TURUN
YLIOPISTO
UNIVERSITY
OF TURKU

PHOTODISSOCIATION OF AROMATIC MOLECULES BY COINCIDENCE SPECTROSCOPY

Lassi Pihlava

TURUN YLIOPISTON JULKAISUJA – ANNALES UNIVERSITATIS TURKUENSIS
SARJA – SER. AI OSA – TOM. 730 | ASTRONOMICA – CHEMICA – PHYSICA – MATHEMATICA | TURKU 2024

TURUN
YLIOPISTO
UNIVERSITY
OF TURKU

PHOTODISSOCIATION OF AROMATIC MOLECULES BY COINCIDENCE SPECTROSCOPY

Lassi Pihlava

TURUN YLIOPISTON JULKAISUJA – ANNALES UNIVERSITATIS TURKUENSIS
SARJA – SER. AI OSA – TOM. 730 | ASTRONOMICA - CHEMICA - PHYSICA – MATHEMATICA | TURKU 2024

University of Turku

Faculty of Science
Department of Physics and Astronomy
Physics
Doctoral Programme in Exact Sciences

Supervised by

Prof. Edwin Kukk
Department of Physics and Astronomy
University of Turku
Turku, Finland

Reviewed by

Prof. Dr. Sadia Bari
Deutsches Elektronen-Synchrotron DESY
Hamburg, Germany
&
Zernike Institute for Advanced Materials
University of Groningen
Groningen, The Netherlands

Dr. Kari Jänkälä, Docent
GrainSense Oy
Oulu, Finland

Opponent

Prof. Emma Sokell
School of Physics
University College Dublin
Dublin, Ireland

ISBN 978-952-02-0007-7 (PRINT)
ISBN 978-952-02-0008-4 (PDF)
ISSN 0082-7002 (PRINT)
ISSN 2343-3175 (ONLINE)
Painosalama, Turku, Finland, 2024

”It’s very hard to imagine
all the crazy things
that things really are like.”
-Richard Feynman

UNIVERSITY OF TURKU
Faculty of Science
Department of Physics and Astronomy
Physics
PIHLAVA, LASSI: Photodissociation of Aromatic Molecules by Coincidence Spectroscopy
Doctoral dissertation, 160 pp.
Doctoral Programme in Exact Sciences
December 2024

ABSTRACT

This thesis presents five studies on the gas-phase photodissociation dynamics of eight aromatic molecules: nimorazole, metronidazole, tetrabromothiophene, diiodothiophene, 2-nitroimidazole, 4-bromo-2-nitroimidazole, 4-bromo-5-nitroimidazole, and 2-bromo-5-iodo-4-nitroimidazole. The work is fundamental research on molecular physics, investigating how the molecules break down following photoionisation.

All the samples were powders at room temperature and atmospheric pressure. The dissociation mechanisms could be studied at the molecular level on isolated molecules by evaporating the samples in a vacuum. Molecules in the gas phase were ionised using UV radiation and X-rays. The ensuing fragmentation processes were then investigated using ion time-of-flight spectroscopy, electron spectroscopy, and coincidence methods.

Two of the articles concern the photodissociation dynamics of thiophenes. Emphasis has been put on analysing certain major fragmentation pathways in detail. The remaining articles focus on nitroimidazoles and aspects of their dissociation dynamics that may explain the radiosensitization properties possessed by some nitroimidazoles. The introductory section of the thesis summarises the publications and covers the theoretical background, experimental details, and research context.

Among the key results are i) an explanation for the difference in radiosensitization efficacy between nimorazole and metronidazole, ii) a dissociation model of dicationic tetrabromothiophene, iii) time-scale information on dissociation of dicationic diiodothiophene, iv) a conclusion that heavy-element-substituted nitroimidazoles seem potential candidates for bifunctional radiosensitizer drugs from a molecular physics point of view.

KEYWORDS: Molecular physics, photodissociation dynamics, ion spectroscopy, electron spectroscopy, coincidence spectroscopy, radiosensitizer

TURUN YLIOPISTO
Matemaattis-luonnontieteellinen tiedekunta
Fysiikan ja tähtitieteen laitos
Fysiikka
PIHLAVA, LASSI: Photodissociation of Aromatic Molecules by Coincidence Spectroscopy
Väitöskirja, 160 s.
Eksaktien tieteiden tohtoriohjelma
Joulukuu 2024

TIIVISTELMÄ

Tämä väitöskirja sisältää viisi tutkimusta kahdeksan aromaattisen molekyylin kaasufaasin fotodissosiaatiodynamiikasta. Näytemolekyylejä olivat nimoratsoli, metronidatsoli, tetrabromitiofeeni, dijoditiofeeni, 2-nitroimidatsoli, 4-bromi-2-nitroimidatsoli, 4-bromi-5-nitroimidatsoli ja 2-bromi-5-jodi-4-nitroimidatsoli. Työ on molekyylifysiikan perustutkimusta ja selvittää miten molekyylit hajoavat fotoionisaation seurauksena.

Näytteet olivat huoneenlämpötilassa ja normaalissa ilmanpaineessa kiinteitä jauheita. Dissosiaatiomekanismeja tutkittiin molekyylitasolla yksittäisissä molekyyleissä höyrystämällä näytteitä tyhjiössä ja ionisoimalla kaasufaasissa olevia molekyylejä röntgen- ja UV-säteilyllä. Ionisaation käynnistämiä fragmentaatioprosesseja tutkittiin käyttäen ioni- ja elektronispektroskopioita sekä koinssidenssimenetelmiä.

Artikkeleista kaksi käsittelee tiofeenien fotodissosiaatiota. Analyysissä on keskitytty erityisesti tärkeiden hajoamiskanavien ymmärtämiseen. Muissa artikkeleissa tutkitaan puolestaan nitroimidatsoleja. Näiden tutkimusten keskiössä ovat erityisesti ne fragmentaatiodynamiikan piirteet, jotka voivat liittyä nitroimidatsolien kykyyn toimia sädeherkistäjinä. Väitöskirjan johdanto tiivistää artikkelit ja esittelee taustateoriaa, mittausmenetelmiä ja tutkimuskontekstia.

Väitöskirjan keskeisiä tuloksia ovat i) selitys erolle nimoratsolin ja metronidatsolin sädeherkistetehokkuuksien välillä, ii) tetrabromitiofeeni-dikationin fotodissosiaatiomalli, iii) tieto dijoditiofeeni-dikationin fragmentaation aikakehityksestä ja iv) molekyylifysiikkaan perustuva johtopäätös raskaalla alkuaineella substituoitujen nitroimidatsolien soveltuvuudesta bifunktionaalisiksi sädeherkistäjiksi.

ASIASANAT: Molekyylifysiikka, fotodissosiaatiodynamiikka, ionispektroskopia, elektronispektroskopia, koinssidenssispektroskopia, sädeherkistäjä

Acknowledgements

The work for this thesis was carried out in the Femto group of the Materials Research Laboratory, Department of Physics and Astronomy, University of Turku. First and foremost, I am deeply grateful to my supervisor, Professor Edwin Kukk. Thank you for taking me under your wing and always finding time to guide me. Your decision to offer me a summer internship in 2018 paved the way for this PhD journey. Next, I thank Docent Johannes Niskanen for the numerous discussions (often over morning coffee) and the "pre-pre-examination" of this thesis. Your help over the years has been invaluable. I also thank Dr. Eero Itälä for teaching me the ropes during the summer internship and while I was writing my Master's thesis. I thank all those mentioned above as well as Dr. Sari Granroth, Dr. Anton Vladyka, and Mr. Eemeli Eronen for providing a positive work environment.

Over the past few years, I have had the pleasure of working with many people. I thank Dr. Marta Berholts for her collaboration, for inviting me to visit the University of Tartu, and for letting me be the first author in **publication V**. I thank Dr. Antti Kivimäki for his helpful feedback on the manuscripts. I acknowledge Antti and the rest of the MAX IV staff for their support during the beamtimes at FinEstBeAMS. I am thankful to all the co-authors of our published works who have not been named individually above. Additionally, I thank all the collaborators from the beamtimes, which have not yet materialised in publications.

I thank the preliminary examiners, Prof. Dr. Sadia Bari and Docent Kari Jänkälä, for their valuable comments. Your feedback helped me improve the quality of this thesis. Furthermore, I want to thank my opponent-to-be, Professor Emma Sokell.

I am grateful for the financial support provided by Vilho, Yrjö and Kalle Väisälä Foundation, the Turku University Foundation, the PCS and the EXACTUS doctoral programmes, the Femto group, and the Department of Physics and Astronomy.

Finally, I would like to acknowledge my friends and family. Mum and Dad, thank you for always being there for me and believing in me. Last but not least, Milja, thank you for your love and support. I am lucky to have you in my life.

Turku, December 2024
Lassi Pihlava

Table of Contents

Abbreviations

2NIM	2-Nitroimidazole
4Br2NIM	4-Bromo-2-Nitroimidazole
4Br5NIM	4-Bromo-5-Nitroimidazole
AEPIPICO	Auger-Meitner Electron-PhotoIon-PhotoIon Coincidence
AM	Auger-Meitner
AO	Atomic Orbital
BO	Born-Oppenheimer
BrINim	2-Bromo-5-Iodo-4-Nitroimidazole
ETMD	Electron Transfer Mediated Decay
FinEstBeAMS	Finnish-Estonian Beamline
GPES	Gas-Phase Endstation
GSD	General Secondary Dissociation
HF SCF	Hartree-Fock Self-Consistent Field
HOMO	Highest Occupied Molecular Orbital
ICD	Intermolecular Coulombic Decay
LCAO	Linear Combination of Atomic Orbitals
LUMO	Lowest Unoccupied Molecular Orbital
M	Intact parent molecule
MCP	Microchannel Plate
MO	Molecular Orbital
PEPICO	PhotoElectron-PhotoIon Coincidence
PEPIPICO	PhotoElectron-PhotoIon-PhotoIon Coincidence
PES	Potential Energy Surface
PIPICO	PhotoIon-PhotoIon Coincidence
R	An intact thiophene ring (C_4S in **pub. II** and C_4H_2S in **III**)
R_f	A thiophene ring fragment
SR	Synchrotron Radiation
TOF	Time-Of-Flight

List of Original Publications

This dissertation is based on the following original publications, which are referred to in the text by their Roman numerals:

I E. Itälä, J. Niskanen, **L. Pihlava**, E. Kukk: *Fragmentation patterns of radiosensitizers metronidazole and nimorazole upon valence ionization.* The Journal of Physical Chemistry A, 2020, **124**: 5555-5562.

II **L. Pihlava**, J. Niskanen, K. Kooser, C. Stråhlman, S. Maclot, A. Kivimäki, E. Kukk: *Photodissociation dynamics of halogenated aromatic molecules: the case of core-ionized tetrabromothiophene.* Physical Chemistry Chemical Physics, 2021, **23**: 21249-21261.

III E. Kukk, **L. Pihlava**, K. Kooser, C. Stråhlman, S. Maclot, A. Kivimäki: *Energy-dependent timescales in the dissociation of diiodothiophene dication.* Physical Chemistry Chemical Physics, 2023, **25**: 5795-5807.

IV **L. Pihlava**, M. Berholts, J. Niskanen, A. Vladyka, K. Kooser, C. Stråhlman, P. Eng-Johnsson, A. Kivimäki, E. Kukk: *Photodissociation of bromine-substituted nitroimidazole radiosensitizers.* Physical Chemistry Chemical Physics, 2023, **25**: 13004-13011.

V **L. Pihlava**, P. H. W. Svensson, E. Kukk, K. Kooser, E. De Santis, A. Tõnisoo, T. Käämbre, T. André, T. Akiyama, L. Hessenthaler, F. Giehr, O. Björneholm, C. Caleman, M. Berholts: *Shell-Dependent Photofragmentation Dynamics of a Heavy-Atom-Containing Bifunctional Nitroimidazole Radiosensitizer.* Physical Chemistry Chemical Physics, 2023, **26**: 8879-8890

The original publications have been reproduced with the permission of the copyright holders.

The publications above result from teamwork. The author conducted the experiments as a part of a group in all works and made further contributions as follows. **I**: initial data analysis and manuscript revisions. **II**: main responsibility of data analysis and manuscript writing. **III**: manuscript revisions. **IV**: main responsibility of data analysis and manuscript writing. **V**: shared co-responsibility of data analysis and manuscript writing with the principal investigator.

1 Introduction

Photoabsorption – the absorption of light – by molecules often leads to complex dynamic responses. Depending on the energy of the incoming light, the effects range from subtle structural changes to the complete atomisation of the target molecule via a Coulomb explosion. Photochemical processes are ubiquitous and photoabsorption drives dynamics in e.g. photosynthesis, photodegradation, and radiotherapy.

The retinal molecule is a great example of a photoswitch: a compound that reversibly isomerises between two ground-state species due to photoabsorption. Retinal molecules are found in the rhodopsin proteins of the rod cells, which are responsible for human night vision [1]. When the 11-*cis*-retinal absorbs a visible light photon, it isomerises to all-*trans*-retinal. The change in molecular geometry triggers a cascade of signal transduction processes that eventually result in vision. The *trans*-retinal is then converted back to 11-*cis*-retinal via a sequence of biochemical processes before it can be reused.

Molecules can be modelled accurately in their lowest energy state near the equilibrium geometry with relative ease. Meanwhile, the description of electronically excited states is far from routine [2]. Theoretically predicting the radiation response of even a small quantum system often poses a formidable challenge. For example, the dynamics of a biomolecular system is too complex for *ab initio* simulations and more empirical models must be used [3]. Tracking the photoinduced molecular dynamics of small molecules in experimental studies allows reconstructing an increasingly complete picture, providing a basis for future model development. Coincidence methods [4], like the ones used in the present work, have been invaluable in this task.

This thesis explores how molecules break into pieces after photoionisation. Such a reaction is called photodissociation [5] and the **original publications I-V** report photodissociation dynamics of eight sample molecules: two thiophenes and six nitroimidazoles. A commonality for the samples is that they all have an aromatic ring in their structure. Chapters 2 and 3 provide the necessary physical and experimental background. Research context surrounding the sample molecules is discussed in chapter 4 while chapter 5 summarises the **original publications**.

2 Theoretical Background

An atom consists of positively charged protons, chargeless neutrons, and negatively charged electrons. Each chemical element has a unique number of protons, equal to the number of electrons. Since protons and electrons have equal but opposite charges of one elementary charge unit (e = 1.602176634 x 10^{-19} C), atoms have a net charge of zero. An ion is a charged system with an unequal number of electrons and protons.

The strong interaction binds the protons and the neutrons together, forming the nucleus. The number of neutrons can vary, leading to isotopes with different masses. Protons and neutrons have roughly the same mass, approximately one atomic mass unit (1u = 1.660539 x 10^{-27} kg). The mass of an electron is only about 1/1800 that of a proton. Most of the mass of an atom is therefore contained in the nucleus.

According to the semi-classical Bohr model, the electrons orbit the nucleus due to electromagnetism – similar to how planets orbit the Sun due to gravity. However, the idea of fixed orbits is inaccurate. Instead, a wave function Ψ_{T} properly describes the entire system. The total wave function can usually be separated into nuclear and electronic parts $\Psi_{\mathrm{T}} = \Psi_{\mathrm{N}}\Psi_{\mathrm{E}}$ according to the Born-Oppenheimer (BO) approximation. The heavy nuclei remain largely unaffected by the motion of electrons. Dynamics of the electronic wave function occur in attosecond timescales [3]. For comparison, the natural timescale for the nuclear motion in molecules is much slower, occurring in the femtosecond time domain [6]. In this thesis, we will primarily consider the electronic wave function.

2.1 Electrons in Atoms and Molecules

2.1.1 Electronic Structure of Atoms

Let us start by considering the lone electron of a hydrogen atom. The wave function $\Psi(\bar{r}, t)$ is governed by the Schrödinger equation [7] (and references therein):

$$\hat{H}\Psi(\bar{r}, t) = \mathrm{i}\hbar\frac{\partial}{\partial t}\Psi(\bar{r}, t), \tag{1}$$

where $\hat{H}$ is the Hamiltonian operator, $\bar{r}$ the position in space, t time, i the imaginary unit, and $\hbar$ the reduced Planck constant [8]. The Hamiltonian has the form:

$$\hat{H} = -\frac{\hbar^2}{2m_{\mathrm{e}}}\nabla^2 + \hat{V}, \tag{2}$$

where m_{e} is the mass of an electron and ∇^2 is the Laplacian

$$\nabla^2 = \frac{\partial^2}{\partial x^2} + \frac{\partial^2}{\partial y^2} + \frac{\partial^2}{\partial z^2}, \tag{3}$$

with x, y, and z being the Cartesian coordinates. The first part of the Hamiltonian is the kinetic energy operator. The second part, $\hat{V}$, is the potential energy operator. As a whole, the Hamiltonian is the total energy operator of the closed system.

When the hydrogen atom is not subjected to a time-dependent outside perturbation, the potential energy is independent of time. Energy eigenstates $\Psi_i(\bar{r})$ can then be obtained from the time-independent Schrödinger equation

$$\hat{H}\Psi_i(\bar{r}) = \varepsilon_i \Psi_i(\bar{r}), \tag{4}$$

where ε_i is the total energy. For these states

$$\Psi_i(\bar{r}, t) = \mathrm{e}^{-\mathrm{i}\varepsilon_i t/\hbar}\Psi_i(\bar{r}). \tag{5}$$

The complex wave function oscillates in time, yet $|\Psi(\bar{r}, t)|^2$ remains constant. Such a state is called a stationary state.

The wave function does not reveal where the electron is precisely located at any given time, the actual location can only be pinpointed by measuring the electron. However, it is possible to calculate probabilities. The Born rule states that the probability density for finding a particle at any given point is proportional to the squared modulus of its wave function [9]. The probability P for finding an electron in a volume τ is:

$$P = \int_{\tau} |\Psi(\bar{r}, t)|^2 \mathrm{d}\tau \tag{6}$$

assuming that the wave function has been normalized. The nucleus is surrounded by a cloud of electron density instead of an electron on a fixed orbit à la Bohr model.

In a hydrogen atom, the one-electron wave functions $\Psi_i(r)$ are well-defined and commonly called atomic orbitals (AO). Each such solution to the Equation (4) is identified by a unique set of three quantum numbers: the principal quantum number n (where n = 1, 2, 3...), the orbital angular momentum quantum number l ($0 \leq l \leq n-1$ with integer intervals), and the magnetic quantum number m_l ($-l \leq m_l \leq l$ with integer intervals). When an electron occupies an AO, its angular momentum vector $\bar{l}$ is quantised, having a magnitude of

$$|\bar{l}| = \sqrt{l(l+1)}\hbar. \tag{7}$$

The magnetic quantum number is the projection of this vector against a quantisation axis. Additionally, an electron exhibits quantised spin angular momentum $\bar{s}$ associated with a spin quantum number s (1/2) and a projection m_s ($\pm$1/2). AOs are sometimes labelled using n, l, m_l, and m_s – these are called spin-orbitals.

AOs are named using spectroscopic notation, which incorporates the principal quantum number n and a letter associated with the orbital quantum number l. It is customary to omit m_l from the name. The first four letters (corresponding to l = 0, 1, 2, 3) are s, p, d, and f. For higher values of l, the letters are assigned alphabetically starting from g and omitting the letter j. For instance, the wave function with n = 1 and l = 0 is called 1s. Under this notation, degenerate AOs (different m_l but the same n and l) are collectively referred to by the same name, e.g. 2p. The naming system is a historical convention related to spectral lines, with the first four letters originally corresponding to the words sharp, principal, diffuse, and fundamental.

Orbital Approximation

The time-independent Schrödinger equation cannot be solved analytically for atoms containing two or more electrons. This is due to electron-electron interactions. The overall many-electron wave function must describe the correlated motion of N interacting particles. Although not entirely accurate, it is still useful to extend the concept of AOs to polyelectronic atoms under the orbital approximation [8]. The total N-electron wave function is simplified to be a product of N single-electron wave functions. The motion of a single electron is then independent of the actual positions of the other electrons – each electron moves in an averaged field generated by the nucleus and the electron cloud [10].

Thus, under the orbital approximation each electron in an atom is thought to occupy an identifiable AO. However, all electrons are indistinguishable from one another and the total wave function must be anti-symmetric under the interchange of electrons. Therefore, for a closed-shell atom, the total wave function is usually written as a Slater determinant [8]:

$$\Psi(\bar{r}_1, \bar{r}_2, \dots \bar{r}_N) = \frac{1}{\sqrt{N!}} \begin{vmatrix} \psi_1(\bar{r}_1) & \psi_2(\bar{r}_1) & \dots & \psi_N(\bar{r}_1) \\ \psi_1(\bar{r}_2) & \psi_2(\bar{r}_2) & \dots & \psi_N(\bar{r}_2) \\ \vdots & \vdots & \ddots & \vdots \\ \psi_1(\bar{r}_N) & \psi_2(\bar{r}_N) & \dots & \psi_N(\bar{r}_N) \end{vmatrix} \tag{8}$$

Here, ψ_i are spin-orbitals, $\bar{r}_j$ is the position of the j:th electron and N is the number of electrons. The system is in a superposition, where each occupied orbital is, in a sense, occupied by every electron in the system. Sometimes, the total wave function may need to be written as a linear combination of Slater determinants.

Energy Levels

The energy eigenstates Ψ_i of the single electron in a hydrogenic atom have approximately eigenenergies

$$\varepsilon_{n,j} = \varepsilon_n \left[1 + \frac{Z^2\alpha^2}{n} \left(\frac{1}{j+1/2} - \frac{3}{4n} \right) \right], \tag{9}$$

where ε_n is the energy obtained from the time-independent Schrödinger equation, Z the number of protons, α the fine structure constant, n the principal quantum number, and j the total angular momentum quantum number [11]. The energy spectrum obtains its gross structure from ε_n, which is given as

$$\varepsilon_n = -\left(\frac{\mu e^4 Z^2}{32\pi^2 \epsilon_0^2 \hbar^2} \right) \frac{1}{n^2} \tag{10}$$

Here, μ is the reduced mass of the nucleus and the electron, e the elementary charge, ϵ the permittivity of free space, and $\hbar$ the reduced Planck constant. The term in square brackets in Equation (9) represents a correction to the gross structure, accounting for relativity and spin-orbit interaction. The latter couples the orbital angular momentum $\bar{l}$ and spin angular momentum $\bar{s}$. As a result, each energy level $\varepsilon_{n,j}$ is $(2j$+1)-fold degenerate.

The total angular momentum is obtained as a sum:

$$\bar{j} = \bar{l} + \bar{s}. \tag{11}$$

The quantum number j characterising the eigenstates has the possible values of $j = |l \pm s|$. A p-electron, for example, gives rise to two energy levels: $\varepsilon_{n,1/2}$ and $\varepsilon_{n,3/2}$. For electrons on s-orbitals ($l = 0$), there is no spin-orbit coupling.

Equation (9) is only applicable to hydrogenic atoms. Calculating energy levels of many-electron systems is a more complicated task due to electron correlation and will not be pursued further here. Nonetheless, the concept of energy levels and fine structure can be carried over. Electronic energy levels are also well-documented for many atoms and molecules (for example refs [12; 13]).

Configurations

The Pauli exclusion principle states that no two electrons can have the same combination of quantum numbers n, l, m_l, and m_s. Therefore, each AO (n, l, and m_l) can host two electrons with opposite spins. Spin-orbitals (n, l, m_l, and m_s) have room for only one electron at a time. The AOs can be populated in various ways and the different combinations of occupied orbitals are called configurations.

The system has the lowest total energy in the ground state configuration. The Aufbau principle and Hund's rules guide the search for this configuration. Following the former, electrons occupy AOs starting from the lowest energy AO in the order of increasing energy. Hund's rules must be used when there are degenerate or near-degenerate AOs that will not be fully occupied. Finding the ground state configuration may require laborious numeric calculations. Occupied orbitals with the highest principal quantum number n constitute the valence shell in the ground state. Decreasing n by one from the valence leads to the inner shell, and all orbitals below this are denoted as core orbitals.

2.1.2 Electronic Structure of Molecules

When two or more atoms come together to form a molecule, the total many-electron wave function of the whole system needs to be considered. Again, the total wave function is written as a linear combination of antisymmetrised products of one-electron wave functions following Equation (8). These one-electron wave functions are molecular orbitals (MOs).

MOs are often approximated as a linear combination of atomic orbitals (LCAO), which may extend over the entire molecule in various ways [8; 10]. MO $\phi_m(\bar{r})$ is then constructed as:

$$\phi_m(\bar{r}) = \sum_{i=1}^{N} c_i \psi_i(\bar{r}). \tag{12}$$

A total of N linearly independent MOs is generated from a basis set of N AOs. Here, c_i is a weight coefficient describing how much each AO $\psi_i(\bar{r})$ contributes to the linear combination. AOs are well suited to e.g. symmetry-related qualitative considerations, but in quantitative studies, appropriately chosen basis functions usually replace AOs (yet AOs remain in the LCAO acronym). The c_i coefficients are optimised variationally. As explained in the textbook "Molecular Quantum Mechanics" by Atkins and Friedman[8], the variational principle states that the energy of the true ground state wave function is lower than or equal to that of any trial wave function.

MOs have a bonding, an anti-bonding, or a non-bonding character [8]. Occupation on bonding orbitals lowers the total energy compared to a situation where the constituent atoms are infinitely far apart. Bonding orbitals thereby stabilise the system. Anti-bonding orbitals increase the total energy when occupied, causing a destabilising effect. Some AOs might mix only a little with others, forming nonbonding MOs. This may be due to a large energy difference to other AOs or incompatible symmetries that prevent mixing. However, a non-bonding MO is not an exact copy of the constituent AO as the wave function does adapt to the changed potential.

Figure 1 illustrates the MOs of a water molecule as an example. Using a minimal basis set consisting only of the occupied AOs, seven MOs (five occupied and two unoccupied) will be constructed. The names of the MOs are based on their symmetry properties. In the energy diagram of the figure, the 1s orbitals of hydrogens A and B have already been combined into two linear combinations before mixing with the

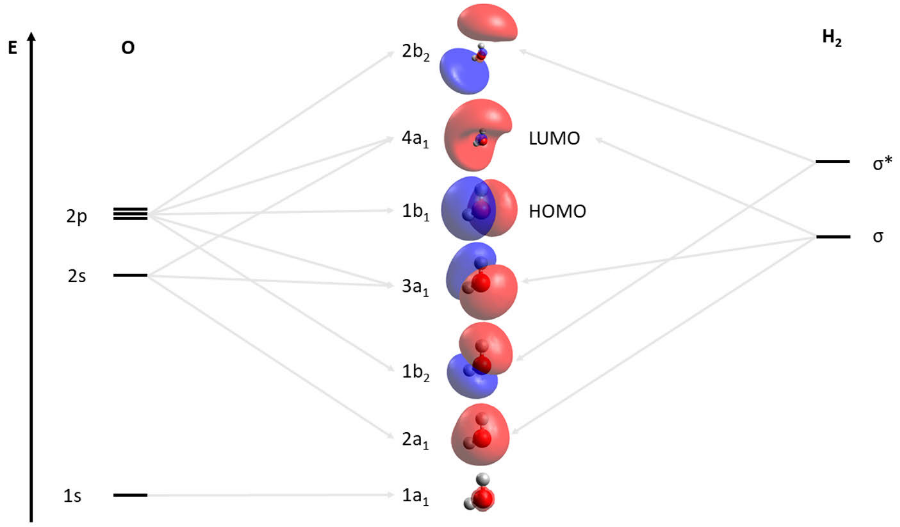

Figure 1. The MOs of a water molecule and the orbitals constituting them according to the LCAO. The energy axis is not to scale. On the left are the AOs of oxygen (1s, 2s, 3 x 2p). The 1s AOs of the two hydrogen atoms (A and B) have already been merged into two linear combinations: σ = 1s$_A$+ 1s$_B$ and σ* = 1s$_A$- 1s$_B$. The MOs were obtained from a Hartree-Fock calculation (aug-cc-pVDZ basis set [14; 15], ORCA 5.0.2 [16–18]) and visualised as isosurfaces around the ball-and-stick models using Avogadro software. An isovalue of 0.02 was used for all MOs except for 1a$_1$, which used 0.005 for illustrative purposes. All orbitals from 1a$_1$ to 1b$_1$ are doubly occupied while 4a$_1$ and 2b$_2$ are unoccupied. The unoccupied MOs are more dispersed than the occupied, so the view was zoomed out. The wave function is positive in the red regions and negative in the blue ones.

AOs of oxygen: bonding σ = 1s$_A$+ 1s$_B$ and antibonding σ* = 1s$_A$- 1s$_B$. The 1a$_1$ and 1b$_1$ are non-bonding MOs and formed by the O 1s and O 2p$_x$ AOs, respectively. The remaining MOs are formed by mixing the O 2s, O 2p$_y$, O 2p$_z$ and the H 1s orbitals. Attention is often given to the shapes of the highest occupied molecular orbital (HOMO) and the lowest unoccupied molecular orbital (LUMO), due to the chemical importance of these two frontier orbitals [19].

Figure 1 shows that electron density accumulates both inside and outside interatomic regions. There are no MOs that strictly correspond to classical covalent bonds, an electron pair shared between two atoms. Therefore, the idea of electrons belonging to individual interatomic bonds is misleading. The traditional mental model of molecules as ball-like atoms connected by rod-like bonds is nonetheless often useful owing to its simplicity and clarity.

Let us now consider inner shell and core MOs in two cases as well as photoionisation from these orbitals. i) The single Br 1s AO in 4-bromo-2-nitroimidazole (from **publication IV**) mixes very weakly with other AOs in the system, forming a nonbonding MO that is essentially localised onto the Br atom. When an electron is ionised from this orbital, a hole (the vacancy left behind by the emitted electron) is also localised on the bromine atom. ii) In a molecule with several core AOs of the same type, the core AOs in principle mix among themselves forming non-localised MOs. The level of mixing in each MO (coefficient c_i in Equation (12)) depends on the energy difference between the constituent AOs – the larger the difference, the less mixing there can be. Therefore, large energy differences result in localised MOs. In N_2 molecule the N 1s AOs have identical energies and form two σ-type MOs. The energy splitting between the MOs is approximately 0.1 eV [20]. This illustrates a more general question about the core and inner shell holes. Should the hole be treated as localised to a specific atom or nonlocalised according to the nature of the initial MO? The answer may vary depending on the particular properties being studied[21]. In the case of photoelectron spectroscopy (discussed in section 3.5), the holes are typically considered localised. Photoionisation recoil studies, for instance, show that the recoil momentum due to an ejected photoelectron is primarily given to a single atom, not to the entire molecule [22]. As the core holes are localised, ionisation of core MOs is often discussed by referring to AOs, i.e. Br 1s or C 1s. We will use this notation throughout this thesis.

Neighbouring atoms affect the energy of core AOs. For instance, the four C 1s AOs in ethyl trifluoroacetate $CF_3{-}CO{-}O{-}CH_2{-}CH_3$ all have inequivalent chemical environments – electrons (and the corresponding core holes) on these four atomic sites experience different electrostatic potentials. When the C 1s photoelectron spectrum is measured, photoelectrons with four different binding energies are seen [23; 24]. The according change in the energies is called a chemical shift. The photoelectrons can be assigned to a specific carbon site with simulations or by considering the electronegativity in the local neighbourhood.

2.1.3 Hartree-Fock Method

Although it is impossible to solve the exact electronic wave function of molecules analytically, an approximate wave function can be acquired numerically using e.g. the Hartree-Fock self-consistent field (HF SCF) method [25]. In the calculations, each electron is subjected to the average field created by all the other electrons and nuclei in the system. The process starts from a reasonable initial trial wave function. The electronic wave function is then optimised iteratively until the expectation value for the total energy of the trial wave function converges within a specified tolerance. By following the variational principle, the approximate wave function can be improved until the energy reaches its minimum.

The total electronic wave function is expressed as a single Slater determinant (or a linear combination thereof). The one-electron wave functions are constructed as linear combinations of basis functions, typically Gaussian-type functions [25]. The number and type of basis functions are defined by the used basis set. Using larger basis sets and including diffuse functions increases the flexibility of the trial wave function. This improves the quality of the calculation, albeit at the cost of increasing computing time.

HF SCF does not address electron correlation properly since it places each orbital in a static average electric potential field generated by all other occupied orbitals in the system. Incorporating the electron-electron interactions more accurately improves the calculations, again at added computational cost. This approach is taken by post-Hartree-Fock methods such as the configuration interaction, the Møller-Plesset perturbation theory, and the coupled cluster methods [25]. An alternative route is to use density functional theory [26].

The Born-Oppenheimer (BO) approximation is essential in HF SCF. The nuclei are treated as stationary and the electronic wave function is solved for the fixed geometry. Molecular geometry optimisation algorithms utilising the HF SCF method consist of sequential single-geometry calculations. At each geometry, the electronic wave function is optimised by HF SCF. The molecular geometry is then moved towards the direction of lower total energy for the subsequent iteration. The procedure is repeated until convergence.

2.2 Potential Energy Surfaces

A potential energy surface (PES) describes the energy of a molecule as a function of its nuclear geometry. Since changes in the geometry are smooth, we can envision a smooth energy "landscape" with rolling hills, mountains, and valleys, where the height of the terrain indicates the energy. Everywhere on the surface, the potential energy includes repulsion between the nuclei and – under the BO approximation – the energy of the adapted electronic structure. Whenever the geometry is inoptimal, the system sits on a hill(side) and tends to travel downhill towards equilibrium, converting potential energy into kinetic energy of the nuclei. Conversely, travelling uphill requires kinetic energy. All electronic states (ground, excited, and ionised) have a unique PES.

Only the relative positions of the atoms affect the potential energy, not the absolute position or orientation of the molecule. A PES of an N-atom molecule ($N \geq 3$) has $3N$-6 dimensions [27]. Diatomic molecules have only one internal coordinate – the distance between the two atoms. This reduces the PES to a one-dimensional potential energy curve.

As long as the system encompasses all reactants and products, chemical reactions can be understood as transitions along one or more PESs. The route taken by the system follows a reaction coordinate and the energy landscape is often depicted as a potential energy curve along this coordinate. If the pathway on a single PES starts from a stable geometry, the system must overcome a potential energy barrier. The route will go through a transition state – a saddle point on the PES (a maximum along the reaction coordinate and a minimum in the direction perpendicular to it) [5].

Let us consider the ground state PES of a water molecule as an example. The three-atom molecule has three internal degrees of freedom: the two OH bond lengths and the HOH angle. Even now, it is challenging to illustrate the PES: the geometric dimensions and energy as the fourth dimension do not lend themselves easily to being a single graph. Therefore, a common tactic is to fix some degrees of freedom, thus showing a lower-dimensional slice of the original PES. Such reduced-dimensionality PES is shown in Figure 2. A water molecule was simulated using the Hartree-Fock method (aug-cc-pVDZ basis set [14; 15], ORCA version 5.0.2 [16–18]). One of the OH bonds was kept at a fixed length of 0.944 Å – obtained from a prior geometry optimization with the same basis set – while the length of the other OH bond and the HOH angle were varied with step sizes of 0.05 Å and 5°. Thus, the figure showcases the energy of the molecule versus the relative position of the unfixed hydrogen atom. In Figure 2a the PES is visualised as a colour map with contour lines as a function of the OH bond length and the angle between the bonds. The minimum of the PES corresponds to approximately 0.947 and 106.1°. The accuracy of the simulation could be improved by using a smaller step size between single-point calculations and a larger basis set – not to forget a more advanced level of theory. In the Figure 2b, the PES is mapped on the XY-plane, where the oxygen is placed in the origo and the fixed hydrogen atom on the x-axis. The PES is more sensitive to stretching than bending, as the slope near the minimum is steeper in the radial direction than in the angular direction.

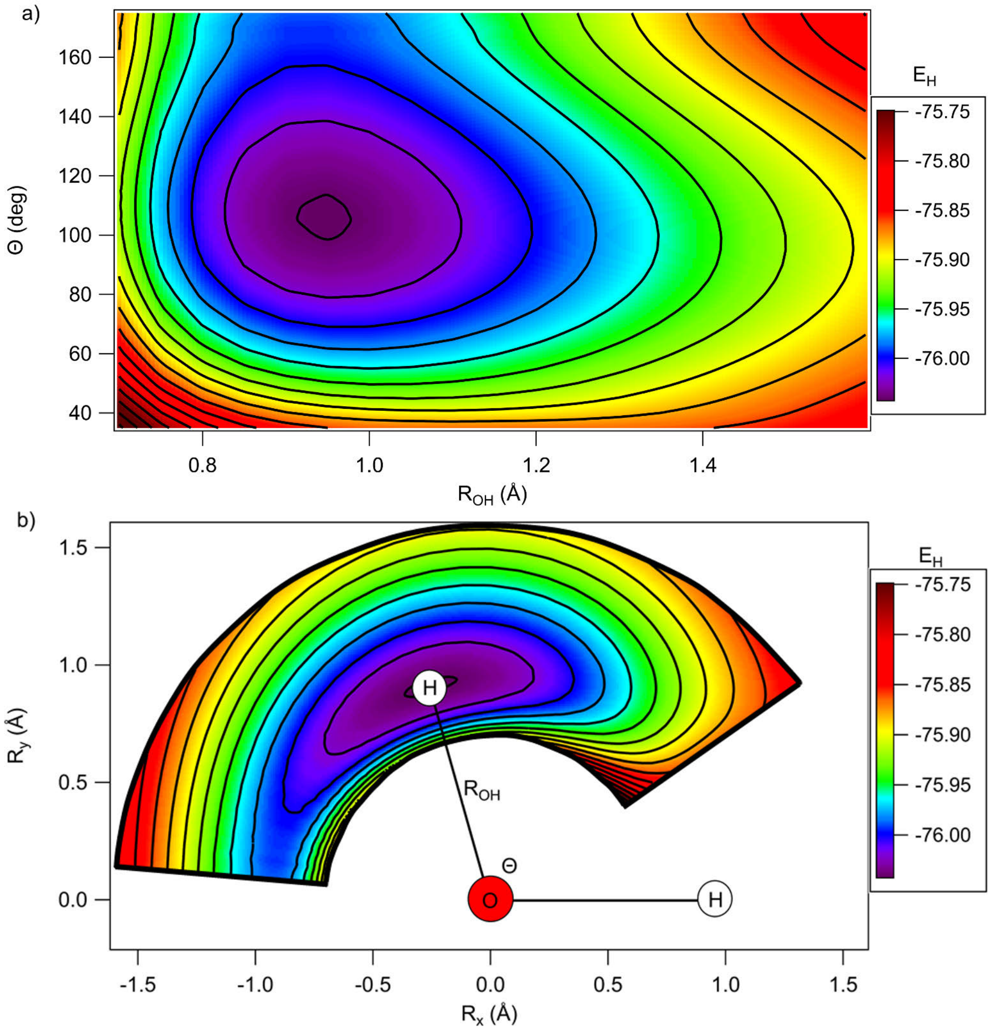

Figure 2. The electronic-ground-state PES of a water molecule as a function of the relative position of the first hydrogen atom using step sizes of 0.05 Å and 5°. The second hydrogen atom was kept at a fixed bond length of 0.944 Å from the oxygen. The energies in the false colour maps are given in hartrees ($E_H \approx 27.21$ eV). a) The PES as a function of the length of the first OH bond R_{OH} and the HOH angle Θ. b) The PES mapped on the XY-plane, with the oxygen atom placed at origo and the fixed hydrogen at (0.957, 0). The system is more sensitive to stretching than bending, as the slope near the minimum is steeper in the radial direction than in the angular.

2.3 Photoionisation and Subsequent Dynamics

2.3.1 Photoionisation

When photoionised, a system absorbs a photon and ejects an electron, leaving the system in a cationic state. Just single-photon absorption is considered here, as light sources discussed in section 3.3 do not generate radiation intense enough for multiphoton processes [28]. It is commonly stated that a specific electron occupying a certain orbital is transferred or removed from the system. However, such a statement is incorrect when considering Slater determinants: each electron in the system is on each occupied orbital so any change in electron configuration involves all the electrons.

The kinetic energy E_k of the photoelectron released from orbital i is

$$E_\mathrm{k} = h\nu - B_i. \tag{13}$$

Here, $h\nu$ is the energy of the incoming photon (h is the Planck constant and ν the frequency of the light) and B_i is binding energy: the energy required to remove an electron from the orbital i. It is the difference in total energy between the initial and final states. Under Koopmans' theorem [29], binding energies can be equated with the one-electron orbital energies from HF-SCF calculation as:

$$B_i \approx -\varepsilon_i. \tag{14}$$

This approximation neglects relaxation of the electronic wave function – orbitals from the system of N interacting electrons are assumed frozen instead of adapting to the new system of N-1 remaining electrons.

Photoionisation from an orbital i becomes possible at the photoionisation threshold – when $h\nu = B_i$. A photon with energy $h\nu < B_i$ can also be absorbed if the energy is exactly right for promoting an electron to an unoccupied orbital. This is known as (resonant) photoexcitation. The likelihood of ionisation – characterised by a photoionisation cross-section – can reach its maximum immediately at the threshold or higher photon energies depending on the type of orbital. At sufficiently high photon energies, the cross-section decreases approaching zero asymptotically. The total cross-section of the system is the sum of cross-sections from all occupied orbitals. In **publication IV**, we approximated the photoionisation cross-sections of the sample molecules using atomic cross-sections found in literature [30].

2.3.2 Photoinduced Dynamics

Photoionisation is generally governed by the Franck-Condon principle, which assumes the ionisation to happen so quickly that the nuclei have no time to move [8]. The system moves from the initial PES to a higher while preserving the nuclear positions and state of motion. This is called a vertical transition.

Classically, the energy required for a vertical transition is the energy difference between the two PESs at geometry R. However, quantum mechanical considerations complicate the classical picture. Molecules are constantly vibrating according to a nuclear vibrational wave function. The vibrations occur on a PES, leading to quantised vibronic (electronic + vibrational) energy levels. When a system transitions from e.g. the ground vibrational state of the neutral electronic ground state PES, it ends up on a higher PES on some vibrational state, which can be other than vibrational ground state. The transition probability to a certain vibrational state is proportional to the squared modulus of the overlap between the initial and final vibrational state wave functions. The energy involved in a vertical transition is the difference between the vibronic energy levels of the initial and the final states.

The equilibrium geometry R_e of the electronic ground state might not be the same as the equilibrium geometry R'_e of the new state. In such a case, the system is not at the minimum of the new PES, allowing various relaxation dynamics to commence. If the photoionisation occurs from the HOMO orbital, the system will only undergo geometry changes along the cationic ground state PES. Otherwise, the system may also relax by transitioning to a lower PES. A vacancy in the electron configuration can be filled by an electron on a higher orbital. The energy difference between the two electronic states is then given away by emitting either a photon (fluorescence, phosphorescence) or an additional electron (Auger-Meitner effect). The former moves the system to a lower PES of the same charge state, while the latter takes the system to a lower PES of a higher charge state. Again, the transitions are considered vertical.

A polyatomic molecule may also pass to a lower PES non-radiatively through a crossing of the two surfaces – a conical intersection [27]. Near these points, the electronic and nuclear wave functions become more strongly coupled and the BO approximation breaks down. Several studies have indicated that conical intersections are an important relaxation pathway for DNA molecules, hindering the formation of radiation-induced damage [31; 32]. Transition through a crossing of states with the same spin multiplicity (total spin is zero for singlet states and one for triplets) is called internal conversion. Intersystem crossing involves a change in the total spin of the electronic system and happens through a singlet-triplet crossing.

The complexity and basic concepts of photoinduced dynamics are exemplified in Figure 3 (originally published in reference [2], reproduced with permission). A polyatomic molecule is first photoexcited from the singlet ground state S_0 to a singlet state S_2. The nuclear geometry relaxes along the PES until passing through a conical intersection to a state S_1. From there, the system can follow either the left or the right path. On the left, the system will later undergo intersystem crossing to a triplet state T_1 and relax to a local energy minimum. If the system becomes trapped in the minimum, it will eventually transition to the singlet ground state via phosphorescence. Alternatively, it may overcome the potential barrier with enough kinetic

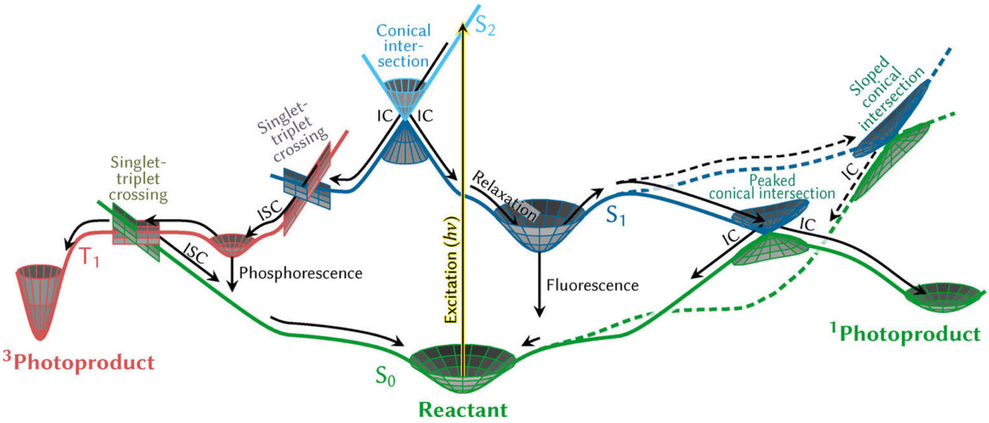

Figure 3. A schematic example of photoinduced dynamics. The system is first photoexcited vertically from the neutral ground state to an excited state, passes to a lower state via a conical intersection, and can then continue relaxing along various pathways. S_0 is a singlet ground state, $S_{1,2}$ are singlet excited states, and T_1 is a triplet state. T_1 is an excited state versus the global minimum on the S_0 PES. However, on the left are molecular geometries where T_1 is the local ground state PES. IC stands for internal conversion and ISC for intersystem crossing. Reproduced with permission from the reference [2].

energy and reach the singlet-triplet crossing, either returning to the singlet ground state or continuing to the global minimum of the triplet state. On the right path, the system may reach the S_0 ground state either via fluorescence or two conical intersections. Once the ground state PES is reached, the system can end up back in the global minimum from where it started or some other local minimum. Substituting photoexcitation with photoionisation introduces a further change into Figure 3: an ionic system cannot return to the neutral ground state. Instead, all relaxation happens on the ionic state PESs.

Auger-Meitner Effect

The Auger-Meitner (AM) effect is a process, where an electronically excited state decays by emitting an electron, increasing the net charge of the system [33–35]. In the commonly used two-step model, the system is ionised and the AM decay occurs soon after. The vacancy is filled by an electron from a higher orbital, and the energy released in the transition is then used to remove another bound electron. Thus, this decay pathway is only possible if the available energy is greater than the binding energy of the AM electron in the ionic state. AM decay can be accessed after core or inner-shell ionisation, whereas valence-ionised states remain singly charged. If energetically possible, the process can repeat in a cascade, leading to more highly charged states.

In the above two-step model, the kinetic energy E_{AM} of an AM electron is not dependent on the photon energy. Instead, it is equal to the energy difference between the final state and the initial excited state:

$$E_{\mathrm{AM}} = E_{\mathrm{f}} - E_{\mathrm{e}}. \tag{15}$$

Here, E_{f} and E_{e} are the total energies of the system and should not be confused with orbital energies. The lifetime of a core-ionised state before the AM decay is in the order of femtoseconds [36], which is enough time for nuclear relaxation to start. However, simulating all the different final and excited states can be time-consuming for efficiently using Equation (15). Rough matching of E_{AM} with AM transitions is often sufficient. Kinetic energy can be approximated in the spirit of Koopmans' theorem as

$$E_{\mathrm{AM}} \approx -(\varepsilon_{\mathrm{c}} - \varepsilon_{\mathrm{f1}} - \varepsilon_{\mathrm{f2}}) \tag{16}$$

when no nuclear or electronic relaxation (other than the transitions) is allowed. Here, ε_{c} is the energy of the core-orbital from which the photoelectron was ejected and $\varepsilon_{\mathrm{f1}}$& $\varepsilon_{\mathrm{f2}}$ are the energies of the orbitals, where the holes will be located after the AM decay.

Kinetic energy E_{AM} of an AM electron can be used as a measure of internal energy E_{int}. Continuing with the above approximation, we may write

$$E_{\mathrm{int}}(\mathrm{M}^{++}) \approx -\varepsilon_{\mathrm{f1}} - \varepsilon_{\mathrm{f2}} - E_{\mathrm{DI}} \tag{17}$$

where $E_{\mathrm{int}}(\mathrm{M}^{++})$ is the internal energy left to the dication after AM decay and E_{DI} is the double ionisation energy (also known as the double ionisation potential). That is the energy difference between the neutral and dicationic ground states. This concept is illustrated in Figure 4. When no further relaxation is allowed, the double ionisation energy is vertical. Adiabatic double ionisation energy is between the neutral and relaxed dicationic ground states. If the photon energy is smaller than double ionisation energy, the system cannot attain a net charge higher than +1. Now, combining Equation (16) with Equation (17), we obtain

$$E_{\mathrm{int}}(\mathrm{M}^{++}) \approx -\varepsilon_{\mathrm{c}} - E_{\mathrm{AM}} - E_{\mathrm{DI}}, \tag{18}$$

as also illustrated by Figure 4.

The AM effect is a local process that involves one molecule. All studies in this work concern gas-phase molecules and only local processes are possible. However, it is worth noting that non-local decay pathways become operable when the molecule is embedded in an environment. The AM decay can then involve multiple neighbouring molecules and is called intermolecular Coulombic decay (ICD) or electron transfer mediated decay (ETMD) depending on the actual mechanism [37].

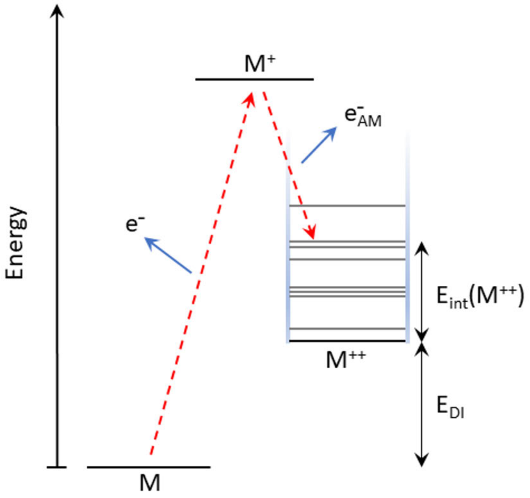

Figure 4. Energy schematics of a molecule M during photoionisation and subsequent AM decay. The core ionised system (M^+) can relax into various dicationic states. If permitted by energy, the system can access even more highly charged states via an AM cascade.

Photodissociation

Photodissociation is a reaction in which a molecule – the parent – breaks apart into fragments due to photoabsorption [5]. Dissociation happens as the molecule relaxes on a PES towards increasing interfragmentary distances as illustrated by Figure 5. The timescale for dissociation is usually in tens or hundreds of femtoseconds [5]. Sometimes, parent molecules may have lifetimes of microsecond or submicrosecond range before dissociation, making them metastable [38]. Dissociation that occurs before a core-hole state has decayed, is called ultrafast.

Molecules can often access various reaction coordinates or fragmentation pathways leading to different outcomes. Chemical bonds are broken, new ones may be formed (migration of hydrogen atoms is not uncommon), and any net charge on the molecule may be distributed differently among the fragments. For example, valence ionisation of diatomic molecule AB can lead to three outcomes:

$$\mathrm{AB} \xrightarrow{h\nu} \mathrm{AB}^+ \longrightarrow \begin{cases} \mathrm{A}^+ + \mathrm{B} & \text{with probability } p_1 \\ \mathrm{B}^+ + \mathrm{A} & \text{with probability } p_2 \\ \mathrm{AB}^+ & \text{with probability } p_3 \end{cases} \tag{19}$$

The system settles on a minimum on the cationic ground state PES in the third pathway, leaving the parent molecule in one piece. Although intact, the parent may have adjusted its nuclear geometry greatly.

The potential energy landscape and the state of the molecule are often unknown. Predicting dissociation dynamics is difficult for all but the smallest systems. Yet, ex-

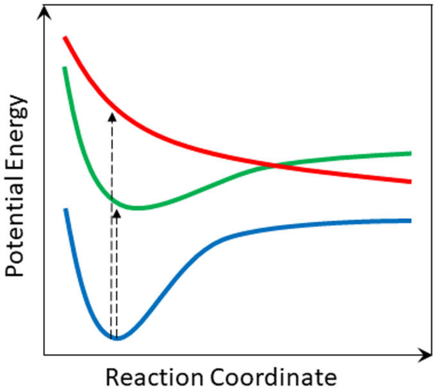

Figure 5. Potential energy curves relevant for photodissociation. Photoionisation can transfer the system from the ground state (blue) to a dissociative excited state (red) or a bound excited state (green). Dissociation occurs when the system relaxes along the red curve towards the dissociation limit – infinite interfragmentary distances. The system can also dissociate from the green curve if it can pass to the red curve with high enough kinetic energy. Alternatively, the system may stay intact by remaining in the green minimum or by passing from the dissociative state to the bound one. Adapted with permission from reference [5]. Copyright 2001 American Chemical Society.

periments allow assigning probabilities for pathways. Some outcomes are observed frequently while others are not at all. These emergent probabilities are dynamic, complicated functions that typically strongly depend on the charge state, internal energy, and even the location of the initial core hole on the molecule in some cases (**publication IV**). Valence and core ionisation lead to completely different fragmentation landscapes. A major difference is that a core-ionised molecule can dissociate via Coulomb explosion as the net positive charges on the molecule repel each other, propelling ionic fragments apart.

3 Experiment

3.1 Gas-Phase Experiments

All the experiments of this thesis were conducted on gas-phase molecules within a vacuum chamber. A specialised vacuum-pumping system creates the vacuum by continuously removing gases from the enclosed volume. Unlike an ideal perfect vacuum, real vacuums are never completely devoid of all matter. Instead, they contain residual gas molecules (the rest gas) – mostly water, nitrogen and oxygen [39]. Some of these molecules have been adsorbed on the chamber walls and are gradually released into the vacuum, while others leak into the chamber from the surrounding atmosphere. With pumping, the vacuum system settles on a dynamic equilibrium pressure.

Dilute gas-phase samples have the significant benefit of enabling the study of individual molecules. Intermolecular interactions can often be disregarded as the average distances between molecules are much greater than the typical length of a chemical bond. The other main advantage is that radiation damage to the sample is not a concern – even in long experiments – since the gas flow constantly introduces fresh sample molecules for study [4].

The partial pressures of the sample and the rest gas constitute the total pressure in the vacuum chamber during an experiment. The amount of residual gases is reduced to a level low enough – here, the chamber pressure is in the order of 10^{-7} or even 10^{-8} mbar before an experiment starts. When sample molecules are introduced to the system, the chamber pressure is typically kept in the order of 10^{-6} or 10^{-7} mbar, which is considered a good high vacuum [39]. Some of this pressure increase can be attributed to the sample molecules but heating (section 3.2) can also increase the release of adsorbed rest gas molecules. The pressure is not uniform across the chamber. Rather, the pressure in the region where sample molecules are injected can easily be higher by an order of magnitude than further away.

The pressure during an experiment is a compromise between two competing factors. i) The sample density must be high enough in the source region to produce a clear signal. This is where the molecules are ionised. ii) Released electrons must have long enough mean free paths – the average distance between successive collisions with other particles – to reach the detectors without any collisions [39]. The mean free path is increased by decreasing the pressure. Therefore, rest gas and dis-

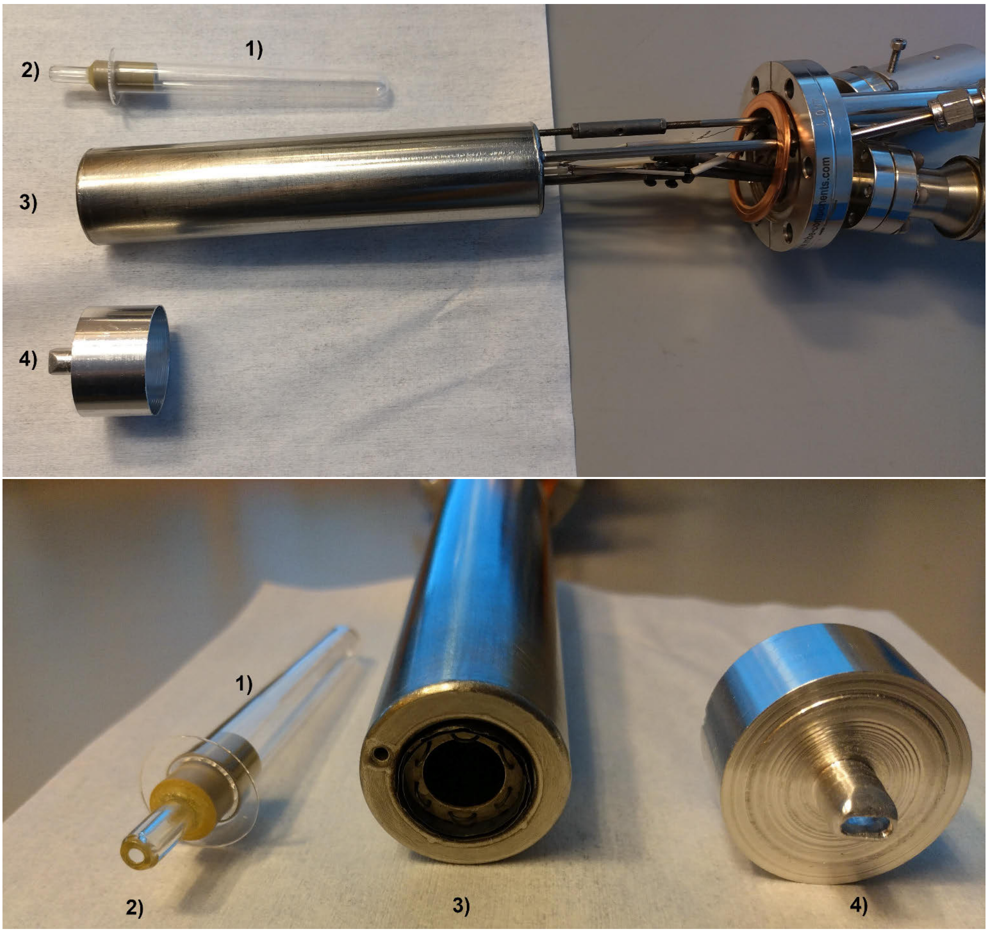

Figure 6. Side and top views of the sample injection setup consisting of 1) a crucible, 2) a capillary cork, 3) an oven, and 4) a cap for the oven.

sipated sample molecules must be removed from the vacuum efficiently.

3.2 Sample Preparation

All samples were solid powders at normal temperature and pressure. They were sublimed into the vacuum for the gas-phase experiments using a setup shown in Figure 6. The powders were at the bottom of a crucible inside an ”oven”. The oven consists of a heat shield and heating filaments surrounding the crucible. The apparatus was installed at the bottom of the vacuum chamber, pointing upwards. The sample sublimation rate usually needs to be boosted by heating. However, in some instances, the studied sample had a high enough vapour pressure at room temperature to produce sufficient gas-phase sample density. A capillary cork was sometimes used to limit the effusion rate of the sample molecules from the crucible. The cork also focused the molecular beam. An oven cap with a large orifice was occasionally used instead of the capillary cork.

The heating needed to be managed carefully for several reasons. i) The effusion rate must be sufficient to not waste limited experimental time at synchrotron facilities by measuring a weak signal that could be strengthened. ii) The effusion rate should not be unnecessarily high. Most evaporated molecules escape the source region without being ionised and are thus wasted. The amount of sample in the crucible is limited, and a high effusion rate comes with the risk of running out of the sample too early. iii) Some samples may undergo thermal degradation when heated. Degradation is a gradual process and not always easily identifiable during an experiment. In the case of thermal damage, the experimental data would then be measured from the sample and the compound(s) formed via degradation. The additional compounds contaminate the data, needing to be identified and excluded from further analysis. Experimental time is also wasted on gathering statistics on contaminants as there are count-rate limitations.

3.3 Light Sources

3.3.1 Gas-Discharge Lamp

A gas-discharge lamp was used as a UV light source in **publication I**. An electric discharge first ionises gas particles. Then, an electric field accelerates the electrons. Once the electrons gain sufficient kinetic energy, they may excite bound electrons in the gas. Finally, a characteristic photon is released when the excitation decays.

Here, the lamp usually uses helium gas. The energy of the main line is 21.22 eV from the He I 1s2p $\rightarrow$ $1s^2$ transition [40]. The radiation also includes other wavelengths from different transitions, but the main line is the most intensive one by far. Different photon energies can be obtained using other gases, e.g. Ar or Kr.

The lamp is mounted to the side of the experimental chamber and connected to it via a capillary. The lamp body houses a cathode, an anode, and a discharge capillary between the two. A constant gas flow was maintained through the lamp from a gas supply towards the anode. Most gas is pumped away while some reaches the main experimental chamber through the same capillary as the UV photons. The gas pressure at the pumping stage is in order of 10^{-1} mbar – much higher than the pressure inside the main chamber. Therefore, differential pumping is employed between the discharge capillary and lamp-chamber capillary. The gas particles are more likely to travel to a pump through a large opening than to the main chamber via the small capillary or back towards the lamp.

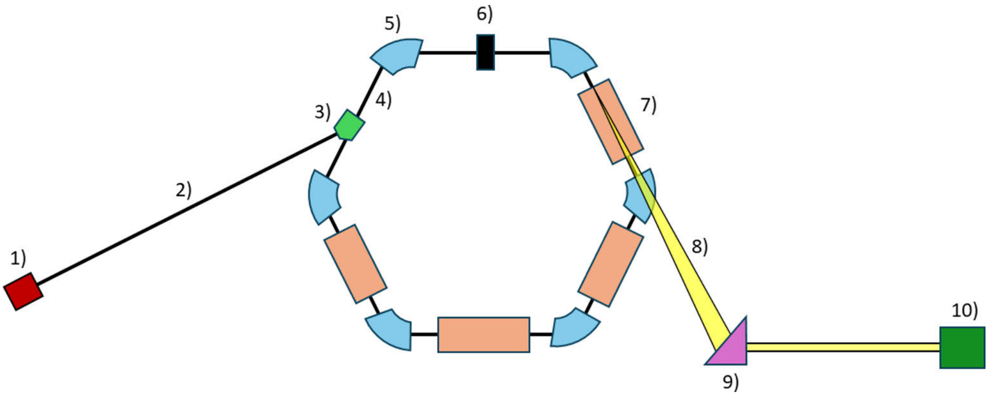

Figure 7. A schematic illustration of a synchrotron. 1) An electron gun, 2) a linear accelerator, 3) an injector, 4) a storage ring, 5) a bending magnet, 6) a radio-frequency cavity, 7) an insertion device (wiggler or undulator), 8) a synchrotron radiation beam inside a beamline, 9) beamline optics, and 10) an end station. The electrons move around the storage ring in a clockwise direction. Although just one X-ray beam has been sketched here, all insertion devices have a beamline and can generate SR simultaneously.

3.3.2 Synchrotron

Publications II-V employed synchrotron radiation (SR) for photoionisation. A synchrotron accelerates electrons close to the speed of light in an ultra-high vacuum system. The relativistic electrons emit SR when "vibrated" by magnets. All the experiments that utilised SR were conducted at the Finnish-Estonian beamline (FinEstBeAMS) [41; 42] of the MAX IV SR facility.

The schematic SR facility in Figure 7 has three main sections: a linear accelerator, a storage ring, and beamlines. An electron gun produces free electrons, which are then accelerated close to the speed of light in a linear accelerator. The acceleration happens using a series of radio-frequency cavities. Each cavity has a strong oscillating electric field. The process is synchronised to make electrons encounter an accelerating electric field at each successive stage instead of being slowed down. The electric field oscillations also pack the electrons into bunches. When the electrons have reached the desired kinetic energy by the end of the linear accelerator, they are directed to the storage ring.

The storage ring is an approximately doughnut-shaped vacuum system, containing a lattice of bending magnets, straight sections connected by the curved lenses, further radio-frequency cavities, and insertion devices [43]. The lattice keeps the electron bunches orbiting the ring with bending and focusing magnets, steering the electrons towards the next bending magnet. Between successive bending magnets are straight sections, which house the insertion devices and the radio-frequency cavities. MAX IV employs undulators as insertion devices. An alternative would be to use wigglers. Both are magnet structures with periodically alternating polarities that

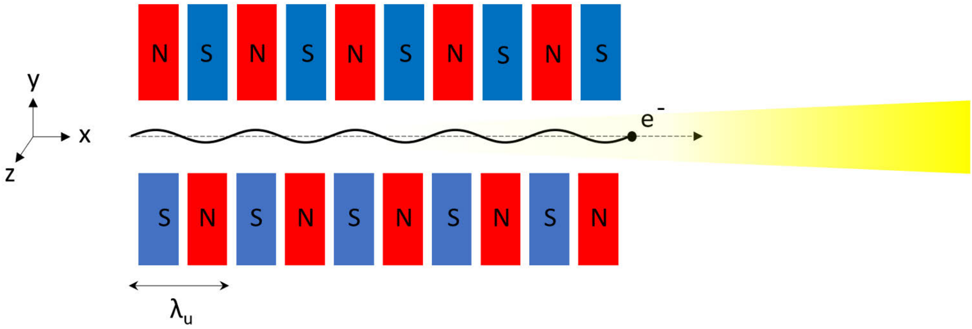

Figure 8. Trajectory of an electron bunch inside an undulator, oscillating in the z-direction due to magnetic fields. SR is emitted in a small cone towards the forward direction in the laboratory frame of reference. Different magnet-array setups are also possible, allowing switching between linearly, elliptically, and circularly polarised radiation.

force the electrons on sinusoidal or helical trajectories. This causes the electrons to produce SR. Electrons emit electromagnetic radiation whenever accelerated, consequently losing energy while travelling around the ring. The radio-frequency cavities replace that lost energy.

A beamline guides the SR beam from the undulator to an end station where experiments are carried out. Each undulator has a designated beamline and can be used independently from one another. End stations around the ring can therefore all have different photon energies. The beam is steered and modified using various beamline optics such as filters, mirrors, monochromators, and slits.

The structure of a simple undulator is illustrated in Figure 8. The undulator consists of magnet arrays that create a periodically alternating magnetic field. A small gap separates the arrays. Once entering the undulator, an electron bunch starts oscillating in the direction perpendicular to the direction of motion and the magnetic field. This results in a sinusoidal trajectory. Electromagnetic radiation is emitted at each turn and radiation pulses from successive periods interfere constructively. The energy spectrum of SR consists of intensive quasi-monochromatic discrete peaks – the fundamental and higher harmonics. Due to the relativistic velocity of the electrons, the radiation is strongly collimated to the forward direction in a laboratory frame of reference, emitted in a narrow cone [44].

The photon energy $h\nu$ of the fundamental is given as [44]

$$h\nu = \frac{2hc\gamma^2}{\lambda_\mathrm{u}}\left(1 + \frac{K^2}{2} + \theta^2\gamma^2\right)^{-1} \tag{20}$$

and the energies of the higher harmonics are integer multiples of the fundamental. Only the odd harmonics and the fundamental are emitted in a cone with an opening angle $1/\gamma$, and the even harmonics are emitted in a ring around the cone, having zero intensity on the axis [43]. Here, h is the Planck constant, c the speed of light in vacuum, λ_u the length of an undulator period, θ is the angle at which the photon was emitted (measured from the forward direction in a laboratory reference frame), γ is the Lorenz factor, and K is an undulator parameter. The Lorenz factor is given as

$$\gamma = \frac{1}{\sqrt{1 - v^2/c^2}}, \tag{21}$$

where v is the speed of the electron. The undulator parameter is

$$K = \frac{eB\lambda_u}{2\pi m_\mathrm{e} c}, \tag{22}$$

where e the elementary charge, B the magnetic field strength, and m_e the electron rest mass [44]. The photon energies can be adjusted with the value of K – the undulator gap can be decreased or increased, making the magnetic field between the arrays stronger or weaker. The undulator parameter $K \approx 1$ for undulators and $K \gg 1$ for wigglers. Bending magnets can also be used to generate SR.

FinEstBeAMS

FinEstBeAMS [41; 42] is located at the 1.5 GeV storage ring of MAX IV. The beamline receives SR from an elliptically polarising undulator of Apple II type [45], which consists of four magnet arrays – two on either side of the gap. The longitudinal position of the individual arrays can be adjusted, allowing the generation of SR with adjustable polarisation. Here, only horizontal polarisation was used. The beamline utilises a plane grating monochromator (600 and 92 lines/mm gratings), covering a wide photon energy range of 4.5-1300 eV.

The beamline has two branches and three end stations. Here, we used the gas-phase end station (GPES) [46]. The SR beam is focused and steered to the select end station with four sets of mirrors. Along the way, the beam size is adjusted with precision baffles and the photon energies can be further adjusted with thin-film filters.

3.4 Ion Mass Spectroscopy

3.4.1 Instrumentation

Mass spectroscopic experiments have three steps: i) ionisation, ii) separation of the created ions based on their mass-to-charge ratio (m/q), and iii) ion detection. Common mass spectrometer designs include quadrupole, linear time-of-flight (TOF), orthogonal acceleration TOF, reflectron TOF, and magnetic sector analysers [47]. This thesis will only cover a linear Wiley-McLaren type ion TOF spectrometer [48] setup used in all experiments here. The spectrometers at the home laboratory and the FinEstBeAMS are custom-made.

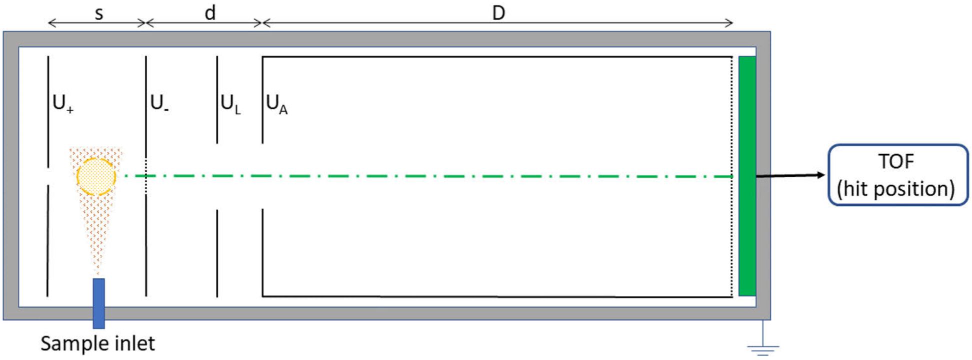

Figure 9. Scheme of the Wiley-McLaren type ion TOF spectrometer. The double-headed arrows indicate the three regions of the system: a source region, an acceleration region, and a field-free drift tube with lengths s, d, and D, respectively. The sample jet encounters the photon beam (yellow circle), and electric fields created by the voltages U_+, U_-, and U_A accelerate cations towards the detector (green rectangle). The setup also includes an electrostatic lens with voltage U_L. The trajectory (green dash-dotted line) passes through three apertures and two grids (black dotted lines).

Figure 9 shows a Wiley-McLaren TOF spectrometer comprising three distinct regions: a source region, an acceleration region, and a field-free drift tube. The spectrometer propels ions through the regions towards a detector. We will define this axial direction as the positive z-direction. The photon beam follows the x-axis, while the molecular beam from the sample inlet travels to the positive y-direction. Directions in the xy-plane away from the central axis will be generally referred to as radial. Ions with different m/q are accelerated to different velocities resulting in different flight times to the detector. The measurements are displayed as a TOF spectrum (abundance vs. flight time), which can be converted to a mass spectrum (abundance vs. m/q).

The gas-phase sample molecules are first introduced to the source region, where they encounter the ionising photon beam. Two parallel plates are on either side of the source region – the pusher and the extractor – at a distance $2s_0 = s$ from each other. Both plates have an aperture in the middle, allowing particles to pass through. Extraction voltage pulses with opposing signs but equal magnitude were applied to the plates with a pulse generator, creating an electric field that accelerates the ions. The pusher was set to a positive potential, U_+, and the extractor to a negative one, U_-. The extraction voltage U_S is then

$$U_\mathrm{S} = U_+ - U_-. \tag{23}$$

The extraction voltage is pulsed to define a starting point for the flight time measurement. The accelerated ions travel through the extractor aperture, entering the acceleration region of length d. The ions are then accelerated to their final kinetic energy with an acceleration voltage U_A. An aperture to the drift tube is located on the opposite side of the region. The drift tube contains no electric fields and the ions keep travelling with the velocity obtained during the two-stage acceleration. At the end of the drift tube, the ions pass through a grid and, finally, reach the detector. In this thesis, the ion detection is done by a microchannel plate (MCP) and a position-sensitive anode.

The MCP contains an array of small channels that run through the plate. When an ion reaches the front end of the MCP and collides with the walls of a channel, it releases secondary electrons that are then accelerated towards the back end of the MCP. Along the way, the electrons keep colliding with the walls and produce a cascade of secondary electrons, resulting in a measurable signal. When only TOF information is needed, as in **publication I**, the signal can be collected directly from the MCP. In **publications II-V**, ion hit positions on the detector were also recorded. This was done using a Hexanode – a hexagonal delay-line anode [49]. The Hexanode is positioned behind the MCP and consists of three coils wrapped around the anode plane at a relative angle of 60° to each other and perpendicular to the MCP. The electron avalanche from the MCP generates a signal in the coils. Measuring the time difference between the signal detection from the opposite ends of each coil allows for calculating the hit position on the anode. Two coils are enough to extract the hit position, and the third coil here serves as a redundancy measure.

The acceleration region contains an electrostatic lens system – an additional aperture plate – set to a potential U_{L}. Ideally, the electric fields would be strictly confined to their designated regions. However, field penetration occurs through apertures, accelerating ions radially. The field penetration can be prevented by overlaying the aperture with a fine mesh, as done with the aperture between the source and acceleration regions. This allows the source region to be field-free between the pulses, which is important for the accuracy of electron spectroscopy during coincidence experiments (section 3.6). Since field penetration occurs in the setup, the lens allows further modification of the ion trajectories. The lens can adjust the size of the hit position distribution. Here, this adjustment is called “zooming”.

Experimental Considerations and Wiley-McLaren Conditions

An ion will be detected after a nominal flight time T_{n} if i) it is located at the centre of the source region at the start of extraction and ii) it has no initial axial velocity. If these conditions are not met, the measured flight time T can deviate from the nominal one. We will define flight time deviation

$$\Delta T = T - T_{\mathrm{n}}. \tag{24}$$

In measured TOF spectra, ions with the same mass-to-charge ratio m/q will have their T distributed around T_{n}.

Optimising the applied voltages (U_S, U_L, U_A) – and other experimental settings such as extraction pulse frequency – is crucial at the beginning of an experiment. The voltages must be set high enough to allow detection of all ions. Ions with high initial radial velocity might hit the spectrometer walls if T is too long. Increasing U_S and U_A decreases the flight times. However, the voltages should not be too high to avoid overlapping neighbouring structures in a spectrum. Additionally, even the heaviest ions should reach the detector before ions from the following extraction arrive.

H^+ ions were not detected here due to the rising high-voltage extraction pulse distorting the signal of the ion detector. The interference overlaps the detection of the fastest ions before falling below the selected trigger level of ion detection for the voltage generated at the anode. Hydrogen could be seen properly if the extraction voltages were lower. However, many fast hydrogen ions would still escape the source region before extraction. Alternatively, a constant extraction field could be used. This, in turn, would necessitate pulsing the light source, which would require us to change the experimental setting even further. Consequently, we have opted to have a minimum time threshold for the flight time measurements, leaving out H^+ and focusing on other ions.

After finding suitable experimental settings, the next step is minimising the width of TOF peaks. This is done by adjusting the ratio between U_S and U_A. The source region is not point-like and ions formed closer to the detector will be accelerated less. Eventually, they will be overtaken by ions formed further away. Space focusing moves this catch-up point to overlap with the detector. The system is set to comply with the equation

$$D = 2s_0\sqrt{k_0^3}\left(1 - \frac{1}{k_0 + \sqrt{k_0}}\frac{d}{s_0}\right), \tag{25}$$

known as the Wiley-McLaren (space focusing) condition [48]. Here

$$k_0 = \frac{s_0E_\mathrm{s} + dE_\mathrm{d}}{s_0E_\mathrm{s}}, \tag{26}$$

s_0 is the distance from the centre of the source region to the extractor, d is the length of the acceleration region, and D is the length of the drift tube. E_s and E_d are the electric field strengths in the source and acceleration regions, respectively.

3.4.2 Data Treatment

Identifying Ions

The nominal flight time T_n in a linear Wiley-McLaren type spectrometer is

$$T_\mathrm{n} = T_0 + C\sqrt{m/q}, \tag{27}$$

where T_0 and C are calibration coefficients and m/q the mass-to-charge ratio of an ion. The calibration coefficients depend on the applied voltages and the spectrometer geometry, making comparison of TOF spectra from different experiments potentially inconvenient. Therefore, TOF spectra are converted to mass spectra using Equation (27) as done in Figure 10. T_0 and C can be obtained by finding two peaks of known ions – such as rest gas or the parent. Two simultaneous equations can then be formed to solve the unknown parameters, allowing the assigning of spectral features to ions. Conventionally, atomic mass units (1 u = 1.660539 x 10^{-27} kg) and multiples of the elementary charge (1 e = 1.602177 x 10^{-19} C) are used here [47].

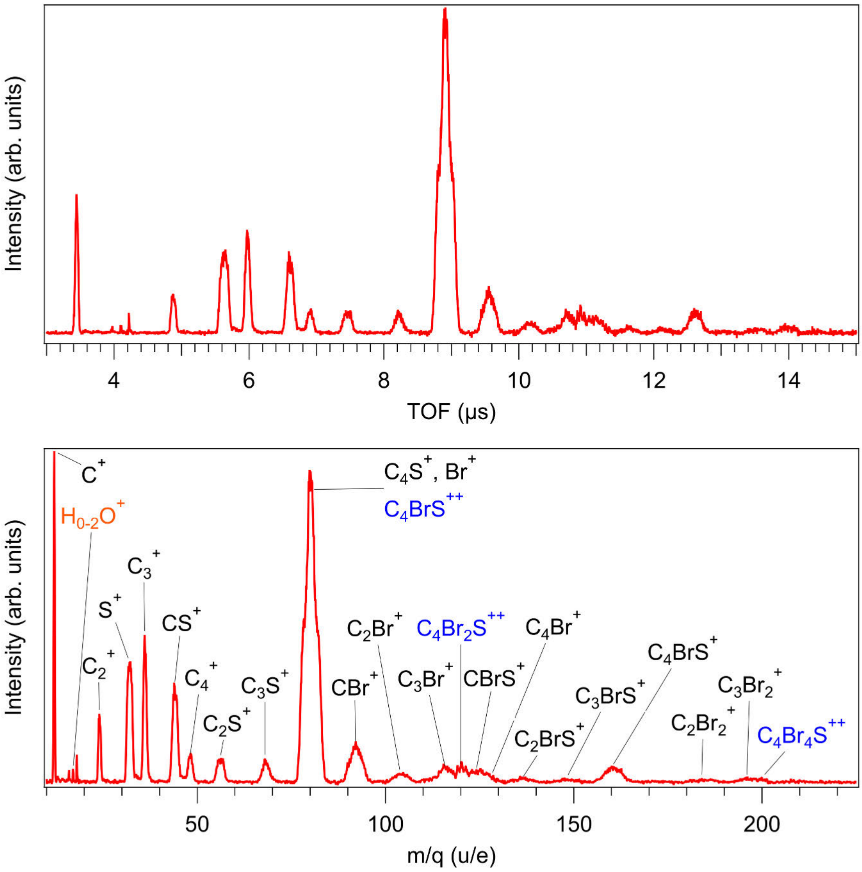

Figure 10. Top: an ion TOF spectrum of tetrabromothiophene, C_4Br_4S from a Br 3d PEPIPICO experiment. Bottom: the spectrum above converted into mass-to-charge scale using Equation (27) and rebinned. All visible fragments have been identified. Dications have been highlighted in blue and residual water in orange.

Potential fragments are devised by systematically breaking the chemical bonds of the parent molecule in different combinations. Some fragments may also require changes in the geometry of the parent molecule, such as hydrogen migration. Here, most fragments are singly charged, even if the parent obtained a higher charge via core ionisation and subsequent AM decay. The positive net charges repel each other and often localise on different fragments, although detection of dications is not uncommon. Ideally, potential fragments from the sample and the rest gas should be enough to explain all observed spectral features. Unfortunately, some experiments include unknown contaminants, which must be distinguished from the sample and excluded from analysis.

Let us assume that fragments A^+ and B^+ have the same m/q and can be released from the photodissociation of molecule M. A peak at that specific m/q could correspond to either one of the ions or a mixture of the two. Here, the resolution is not good enough to resolve, for example, CH_2^+ and N^+ despite the small difference in masses. However, the more likely candidate may sometimes be deduced:

1. As a general rule, A^+ is more likely to be observed than B^+ if it can be obtained more easily from M – i.e. with fewer bond breakages and geometrical restructuring of the parent.

2. Some elements have more than one stable isotope, e.g. bromine with $^{79}\mathrm{Br}$ and $^{81}\mathrm{Br}$ in approximately 1:1 ratio. All isotopes must be present according to their natural abundances: a peak at 79 u/e cannot correspond to Br if there is no peak at 81 u/e. In **publications II, IV,** and **V** the mass peaks from the Br isotopes overlapped, resulting in a wide peak centred around 80 u/e.

3. The spectrum may contain complementary features, such as $(M-A)^+$. Even if both A^+ and B^+ are easily released, $(M-B)^+$ might be a highly unlikely fragment, requiring a great deal of restructuring. This would indicate that at least neutral A is released, making the production of A^+ more likely. $(M-A)^+$ and A^+ could originate from the same fragmentation pathway with the charge localising on either one of the two. However, it is worth noting that the charge can also localise predominantly on just one of the fragments

4. When the charge of the parent is higher than +1e, A^+ and B^+ may be distinguished by studying ion-ion coincidences (see section 3.6). Let us assume that i) either A^+ or B^+ is detected in tandem with a third fragment C^+, ii) A^+ and C^+ can be obtained simultaneously from the same molecule, and iii) B^+ and C^+ cannot be released simultaneously. Therefore, the unknown ion pair must be (A^+, C^+), and A^+ is detected instead of B^+.

5. When the charge of the parent is higher than +1e, it becomes possible to observe dications (or even more highly charged fragments). If fragments A^+ and C^{++} are released via dicationic dissociation and have the same m/q, the assignment can be done based on the peak shape. A^+ experiences Coulombic

> repulsion due to the other charge in the system, accelerating before the extraction. Consequently, the peak profile is broadened. The dication contains both charges in the system and experiences no repulsion. The initial velocity will be low, resulting in a sharp peak.

Position-sensitive ion detectors record when and where the ions hit the detector. Figure 11 illustrates such data measured upon N 1s ionisation of N_2 gas. The gas molecule becomes doubly charged, either dissociating into two N^+ fragments or staying intact as N_2^{++}. Both have $m/q = 14\ \mathrm{u/e}$ and identical nominal flight times. Yet, the ions are easily identifiable in the TOF spectrum because they have different lineshapes as seen in panel 11a). Although there are only two ions, the spectrum shows three peaks. The sharp middle peak is centred at the nominal flight time and belongs to the dication. The two peaks at either side of the sharp central peak belong to N^+. By solely judging the TOF spectrum, these structures might be incorrectly considered distinct and the left (right) peak would be assigned with m/q value smaller (greater) than 14 u/e. The correct interpretation is that the N^+ cations repel each other, obtaining higher initial velocity than the dication. If the initial velocity vector is oriented towards the detector, the actual flight time will be shorter than the nominal flight time. The initial velocity vectors are distributed isotropically, resulting in similar intensities on both sides of the nominal flight time. Dication experiences no such Coulombic repulsion, having less initial velocity and staying close to the central axis.

The detector image in panel 11b) confirms the above explanation: the dications are localised in a small, intensive pattern at the centre while the cations are much more spread out. This is better highlighted in panel 11c)-f), where the false colour scheme has been scaled differently to emphasise weak features. The panels 11d) and e) show the hit position x- and y-coordinates against TOF, respectively. Comparing these panels against the TOF spectrum clarifies why N^+ ions are in two peaks instead of a single broad one. The final panel, 11f), illustrates the radial hit position from the central axis ($R = |\sqrt{X^2 + Y^2}|$) versus TOF. The cations form an identifiable ”arch” centred around the nominal flight time.

Figure 11 has been chosen deliberately for two reasons: i) it exemplifies the usefulness of hit position information in TOF measurements. Discussion on related analysis continues in the next section. ii) The figure also illustrates non-optimal behaviour that, unfortunately, sometimes occurs in experiments. The detector image is slightly elongated in the x-direction. This is partially due to the photon beam, which is also along the x-axis. The detector images are also otherwise distorted, seen clearly in the asymmetric dication pattern and the edges of the cation pattern in the y-direction, panel 11e). These geometric distortions are systematically observed at the experimental station. The figure shows signs of ion loss: the cation “rings” and the arch in panels 11d)-f) are incomplete. Ion loss will be discussed further later.

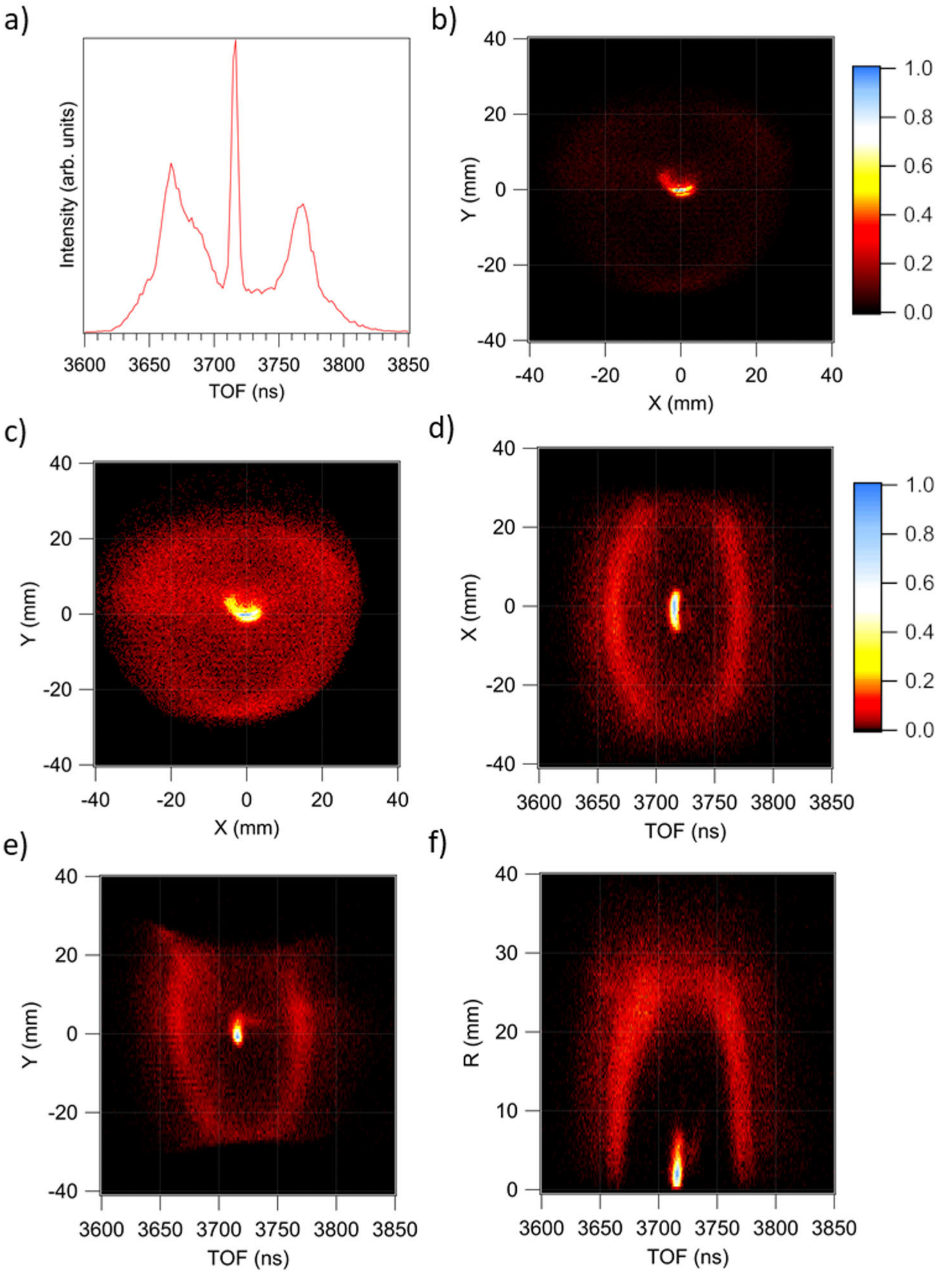

Figure 11. Ion TOF and hit positions measured upon N 1s ionisation of N_2 gas, presented in six panels: a) the TOF spectrum with N_2^{++} in the middle and N^+ on the sides, b) the detector image, c) the detector image with a false-colour scheme that emphasises weak features (also used in the following panels), d) the ion hit position in the x-direction versus TOF, e) the ion hit position in the y-direction versus TOF, and f) radial hit position versus TOF. The colour scales depict relative intensity. The ion hit positions have been corrected to place the bright N_2^{++} spot at the centre. The dication stays close to the centre due to the lack of Coulombic repulsion and can be distinguished easily from the cation. The figures show non-optimal behaviour: distortions systematically observed at the experimental station and ion loss.

Extracting Ion Momentum

Flight times and hit positions allow the reconstruction of initial momentum vectors – the momentum an ion has obtained from the dissociation before the extraction. The total initial momentum vector $\bar{p}$ is calculated as follows:

$$\bar{p} = m\bar{v} = m(\bar{v}_x + \bar{v}_y + \bar{v}_z) \tag{28}$$

where m is the mass of the fragment, and $\bar{v}_{x,y,z}$ are the x-, y-, and z-components the initial velocity, respectively. Since the mass of the fragment is a known constant, the initial velocity needs to be obtained from the data.

The initial radial components of the velocity are calculated using the flight time and the hit position of an ion. Only axial forces affect the ion trajectories when assuming no field penetration or zooming. Therefore, any distance travelled from the central axis is due to the radial initial velocity. These velocity components are calculated as

$$\bar{v}_x = \frac{\bar{X}}{T} \text{ and } \bar{v}_y = \frac{\bar{Y}}{T} \tag{29}$$

where $\bar{X}$ and $\bar{Y}$ are the displacement vectors in the x- and y-directions from the central axis, and T is the actual flight time of the ion (not the nominal flight time). In practice, the detector image is never perfectly aligned at the centre of the detector. Therefore, all hit positions are shifted to centre the detector image at origo during analysis. Here, a constant shift for all ions is suitable, since the centre position misalignment does not show any flight-time dependence.

When an accurate study of the ion momenta is needed, the lens zooming must be accounted for. According to simulations, the above momentum components are multiplied by a zooming coefficient, typically between 0.8 and 1.2, depending on the experimental settings. In the simplest approximation, the coefficient is set to 1.

Determining the initial axial velocity component $\bar{v}_z$ is slightly more complicated than the radial components. It can be estimated using the observed flight time T, the nominal flight time T_n, and known experimental parameters. The flight time of an ion is the sum of the times spent in the source region, acceleration region, and the drift tube. Using basic Newtonian mechanics, T can be approximated [50] as:

$$T = \frac{v_1 - v_z}{a_1} + \frac{v_2 - v_1}{a_2} + \frac{D}{v_2} \tag{30}$$

$$v_1 = \sqrt{v_z^2 + 2a_1 s_0} \tag{31}$$

$$v_2 = \sqrt{v_z^2 + 2a_1 s_0 + 2a_2 d}. \tag{32}$$

All velocities v and accelerations a are axial and the vector signs are dropped accordingly. Here, v_z is the initial velocity, while v_1 and v_2 are the ion velocities at

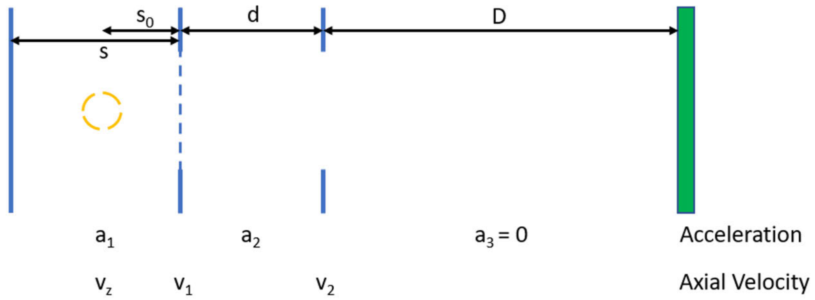

Figure 12. A schematic of a Wiley-McLaren type two-stage TOF configuration with the dimensions and the source region indicated. The constant accelerations in the source, the acceleration, and the field-free (drift tube) regions are a_{1-3}. The initial axial velocity is v_z while v_1 and v_2 are the axial velocities at the end of the source and acceleration regions. The lens system has been omitted from the illustration. Adapted from [50].

the first and second apertures. Accelerations a_1 and a_2 are the accelerations in the source and acceleration regions. The distance from the centre of the source region to the first aperture is marked by s_o. The lengths of the acceleration region and the drift tube are d and D. The variables are also detailed in Figure 12.

Let us consider two ions with the same m/q that are initially travelling with speeds of v_z and $-v_z$ towards and away from the detector. The system is space-focused and otherwise ideal. After leaving the source region, the first ion will travel at speed v_1 ($v_1 >> v_z$). The second ion will travel towards the pusher, slow down, and accelerate towards the detector. When it returns to the centre of the source region after turning around, it will have speed v_z because the electric field is conservative. From this point, it will also accelerate to the same v_1 as the first ion. Thus, although v_z affects the flight times in the acceleration region and the drift tube, the two ions behave identically in these areas, and any flight time difference between them is accumulated in the source region. In a first approximation, the flight time deviation ΔT depends on v_z as:

$$\frac{\partial(\Delta T)}{\partial v_z} \approx -\frac{1}{a_1}. \tag{33}$$

The axial acceleration is written according to Newton's second law:

$$a_1 = \frac{F}{m} = \frac{qE_\mathrm{s}}{m} = \frac{qU_\mathrm{S}}{ms_0} \tag{34}$$

where E_s is the strength of the electric field in the source region and U_S is the extraction voltage. Thus, v_z is

$$v_z \approx -\frac{qU_\mathrm{S}}{ms_0}\Delta T. \tag{35}$$

The initial ion momentum may now be calculated using Equation (28).

Accounting for Ion Loss

Many ions will remain undetected during an experiment. Part of the ion loss is inherent to the instrument:

- Wire meshes stop some ions from passing through apertures – here, about 20% each. Our system includes two meshes, so only about $(80\%)^2 = 64\%$ of all ions can reach the detector.

- Only ions hitting the capillaries of the MCP can be detected. Let us assume that the capillaries are packed tightly next to each other and have round cross-sections of radius r. The smallest possible concentric square outside such a capillary has an area $(2r)^2$. The maximum active versus inactive area ratio is thus $(\pi r^2)/(4r^2) \approx 0.79$. In practice, a ratio of 0.5 can be considered good, as the capillaries are not packed so tightly. Furthermore, efficiency across the detector surface might be non-uniform due to defects and wear. Some ions hitting the active area might therefore remain undetected.

- When two ions arrive at the same MCP capillary nearly simultaneously, the second ion may remain undetected. The arrival of the first ion causes a response, during which the capillary cannot process another ion. Although each channel of an MCP has a dead time of approximately 10^{-2}s, the MCP consists of thousands or tens of thousands of parallel channels, making the effective dead time of the detector multiple orders of magnitude smaller [51].

Some other sources of ion loss can be influenced during the experiment.

- An ion is recorded when a signal pulse from the MCP exceeds some user-defined threshold value set to reduce signal noise from the data. The voltage pulses from an MCP vary in magnitude. Weak pulses might fall under the trigger threshold, leaving the ion detection out of the recorded data.

- As mentioned earlier, hydrogen ions were omitted from the measurements due to interference caused by the high-voltage extraction pulses. The flight-time threshold and the strength of the extraction pulse can be adjusted.

- The photon beam and the sample injection may be misaligned. If the sample molecules are ionised in an incorrect spot, ions might start missing the first aperture.

- Here, extraction voltages were pulsed with a frequency of several kilohertz and the pulse duration was around 10 μs. Ions created right after the extraction pulse is turned off may escape the source region – especially if they have a high initial velocity.

- The extraction and acceleration voltages may be insufficient. If the nominal flight time is too long, ions with radial initial velocity components might start hitting the spectrometer walls instead of reaching the detector.

The final bullet point posed a challenge for the **publication V**. The ion spectrometer voltages were too low, causing a notable loss of fast ions, and the mistake was not noticed in time. As the amount of lost ions had to be estimated to introduce a correction, we will next introduce two analytical methods that can be used – apart from simulating the system.

Signs of ion loss can be already seen in Figure 11. The N^+ cations form a round pattern on the detector image, panels 11b) and c). The pattern fills the entire detector, even extending beyond the edges, albeit judging this solely based on the detector image may be difficult. The panels d) and f) show the ion loss more clearly. The N^+ patterns are incomplete, failing to form closed rings. Although the x-direction pattern is almost complete, it has a lower intensity around $X \approx \pm 30\ \mathrm{mm}$. This corresponds to the edges of the detector. In the y-direction, both extremes are cut off.

The degree of ion loss can first be estimated analytically based on TOF and initial velocity. The detector image cannot be relied upon here if the ring pattern extends beyond the edges of the detector. However, the axial initial velocity does not contribute to ion loss because the detector is in the xy-plane. The complete v_z may therefore be extracted as discussed earlier. The maximum value of v_z corresponds to the magnitude of the initial velocity vector when the initial velocity distribution is assumed isotropic. The molecules are initially randomly orientated but ionisation with linearly polarised light may cause bias in the orientation distribution of the ionised molecules. Therefore, the initial velocity distribution of the fragment ions can be anisotropic. The anisotropy can be rather strong with e.g. a small linear molecule, such as N_2. When a larger molecule dissociates, such as the sample molecules studied in this thesis, the bias in the initial orientation does not affect the initial velocity distribution as strongly. Although it is plausible that some anisotropy remains, isotropicity is a reasonable first approximation for ion-loss correction here.

All ions of the same species do not obtain the same initial momentum upon dissociation. Instead, there is an initial kinetic energy distribution. For simplicity, we shall now use the half width at half maximum (HWHM) of a TOF peak as the value of ΔT, when calculating the initial velocity using Equation (35).

Let us assume that all ions are created at the centre of the source region on the central axis. Then, let α be the angle between the central axis and the leaving trajectory that lands at the edge of the detector. This angle will be approximated as:

$$\alpha \approx \arcsin(\frac{v_\perp}{v}) = \arcsin(\frac{r}{vT_\mathrm{n}}), \tag{36}$$

where $v_\perp$ is the initial radial velocity, v is the total initial velocity, r is the radius of the detector, and T_n is the nominal flight time for a specific m/q. The zooming coefficient is set to 1.

Transmission P is the maximum ratio of ions that can be detected out of all released ions before considering e.g. detector efficiency or ion loss due to meshes. It is calculated as:

$$P = \frac{\Omega}{4\pi} \tag{37}$$

where Ω is the solid angle from which ions with initial velocity $\bar{v}$ can be collected and 4π is the solid angle of a sphere (in steradians).

Due to the cylindrical symmetry of the spectrometer, ions from all sides of the central axis will be treated equally. Effectively, ions will be collected from inside a cone, which has its apex at the centre of the source region. From this, we can calculate a solid angle. We will assume that only a small portion of the total flight time will be spent in the source region. Then the corresponding solid angle for ions originally moving away from the detector will be equal to the other one. Thus

$$P \approx \frac{2 \cdot 2\pi(1 - \cos\alpha)}{4\pi} = 1 - \cos\alpha, \tag{38}$$

where multiplication by 2 accounts for ions moving either towards or away from the detector, $2\pi(1-\cos\alpha)$ is the solid angle described above, and 4π is the solid angle of a full sphere. Although the zooming effect has been ignored and the initial velocity has been extracted from the HWHM of a TOF peak, the analytic estimates given by Equation (38) are congruent with our simulations. Once the transmission has been obtained for each m/q, an estimate for the initial amount of ions (the detected ions + the lost ions) may be calculated by dividing the number of detected ions with the transmission.

Instead of using the above method for analytical estimation, in **Publication V** we decided to apply a momentum-based ion-loss-correction method. We extracted the initial momentum vector $\bar{p}$ for various ions. The zooming coefficient for the non-axial components was simulated. The vectors form a sphere in the momentum space and we projected the sphere onto three orthogonal planes (p_{xy}, p_{xz}, and p_{yz}) for further analysis. The first two projections helped us ensure that the momentum space was accurately centred. The photon beam is aligned in the x direction, making the ions more focused in the y and z directions than in the x. The momentum circle on the p_{yz} plane was further divided into sectors of equal area.

To estimate the ion transmission for an ion species, we assumed that (i) the momentum distribution is isotropic and (ii) all ions in the most populated sector are detected. Any lower intensities in other sectors were considered to be caused by ion loss. We could not be certain that all ions were detected in the x and y directions because their full pattern might extend beyond the edges of the detector image.

However, in the z direction, there were no such concerns. Finally, the transmission was calculated by dividing the total number of detected ions by the highest ion count across the p-projection angle on the p_{yz} plane multiplied by the number of sectors.

3.5 Electron Spectroscopy

3.5.1 Instrumentation

Different electron spectrometer classes include dispersive, retarding field, and time-of-flight analysers [52]. A commonality for all the types is that they differentiate electrons based on kinetic energy. A hemispherical analyser – a dispersive design – is solely used in this thesis. We have used an Omicron 150 mm mean radius hemispherical analyser in our home laboratory while the GPES [46] at FinEstBeAMS is stationed with a Scienta R4000. Both instruments are re-equipped with a 40 mm active area MCP and a resistive anode position-sensitive detector.

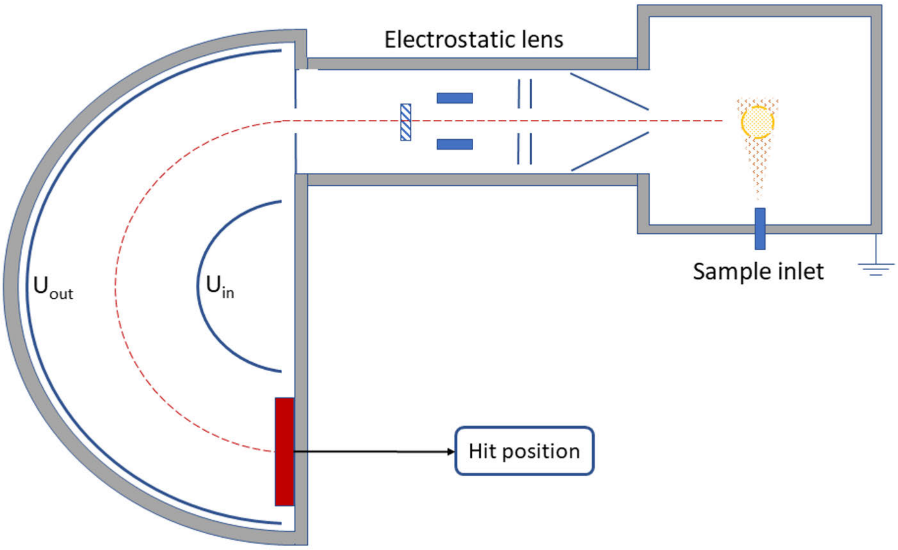

Figure 13. Schematics of a hemispherical analyser used in this thesis. Electrons that are emitted at a narrow solid angle towards the spectrometer first travel through an electrostatic lens system that accelerates/retards electrons. The lens system also often contains electrodes used to adjust the trajectories. After entering the hemispherical analyser via a slit, electrons are steered around the inner hemisphere to a position-sensitive detector.

Figure 13 depicts an electron spectrometer consisting of a hemispherical analyser and an electrostatic lens system. The released electrons are not collected from the source region with electric or magnetic fields. Instead, only electrons emitted at a narrow solid angle can enter the spectrometer. The lens system consists of multiple elements that influence electrons in two ways: i) All electrons are accelerated/decelerated so that electrons with selected kinetic energy E_c will end up with kinetic energy E_p – the pass energy. Energy differences between electrons remain unchanged. ii) The lenses steer and focus electrons towards an entrance slit to the analyser, increasing the acceptance of the spectrometer.

Once inside the analyser, the electrons travel between two concentric hemispheres. The inner hemisphere is set to a higher electric potential than the outer one. This creates a radial electric field between the hemispheres that deflects electron trajectories. In the setups used here, a position-sensitive detector is placed as shown in Figure 13 and the electrons with final kinetic energy E_p hit the centre of the detector. Electrons slower than this drift closer to the inner hemisphere and faster electrons end up closer to the outer hemisphere. The hit positions on the detector therefore correspond with kinetic energies. The total width of the energy window is approximately 10% of E_p.

The resolution of an electron spectrometer refers to the ability to separate electrons with different energies from one another. Here, a good approximation of the energy resolution ΔE – the smallest energy difference that can be discerned – is

$$\Delta E = \frac{sE_\mathrm{p}}{2r} \tag{39}$$

where s is the entrance slit size and r is the mean radius of the hemispheres. When s and E_p are chosen for an experiment (r cannot be adjusted), the resolution is balanced against the size of the energy window and the electron count rate. A large slit allows more electrons to pass through than a narrow one while having a worse resolution. A good resolution is often important when measuring only an electron spectrum. A spectrum with a large energy range can be accumulated by slowly scanning through the range with a narrow energy window. The ionisation rate can also be increased to compensate for low transmission. The rate is kept low in photoelectron-photoion coincidence spectroscopy (section 3.6), and good transmission is often preferred over resolution in such an experiment. Hemispherical analysers have proven versatile in this thesis, allowing the choice between high resolution + low transmission and low resolution + high transmission.

In addition to the above resolution of the spectrometer, other factors also broaden spectral features. i) Core-hole states decay in the order of femtoseconds. Due to the short lifetimes, there is some uncertainty in the energy of the core-hole state. The shorter the lifetime, the more uncertainty, and the broader the spectral line. This is called lifetime broadening. ii) The photons used in an experiment do not all possess the same energy. Instead, the energies are distributed around the nominal $h\nu$ with a linewidth $\Delta h\nu$. Due to the slight variation in photon energy, two electrons ejected from the same orbital may have slightly different kinetic energies. iii) Doppler broadening is caused by electrons being emitted from moving gas-phase molecules. The kinetic energy of an ejected photoelectron is slightly higher if the molecule is initially

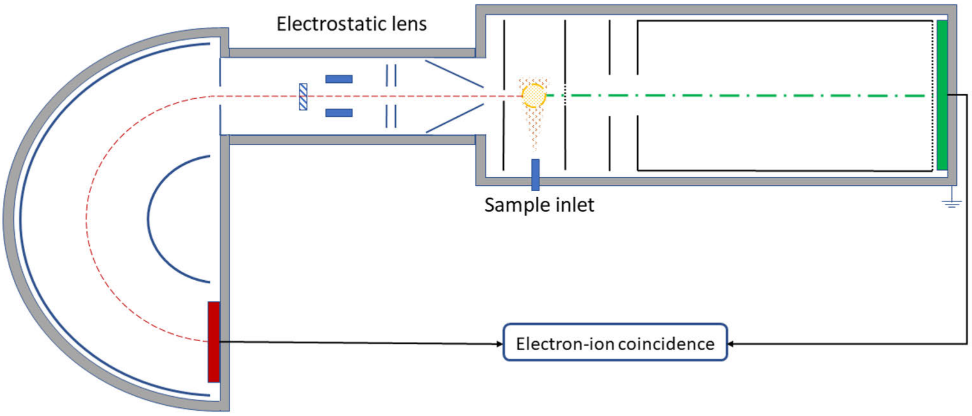

Figure 14. A scheme for a PEPICO experiment. The ion and electron spectrometer setups are the same as in Figure 9 and Figure 13.

moving towards the electron spectrometer than if it is moving away from the electron spectrometer. The total resolution is obtained as a convolution of the instrumental resolution, lifetime broadening, photon linewidth, and Doppler broadening.

3.5.2 Data Treatment

Two calibration measurements are needed for data analysis. i) A dispersion calibration allows the conversion of hit positions into energy scale. A dispersion curve is obtained moving a spectral structure across the detector in multiple steps. This is done by adjusting the photon energy or the selected kinetic energy E_c. The dispersion calibration must be done for each used pass energy. ii) The energy scale may be offset from the proper kinetic energies. A constant correction term is found by measuring a known photoelectron line and comparing it with a literature value (e.g. from [53]). The kinetic energy scale can also be converted into the binding energy scale using Equation (13).

3.6 Coincidence spectroscopy

3.6.1 Instrumentation

Measuring ion and electron spectra in tandem using a coincidence technique [4] reveals correlations between particles – offering further information on dissociation processes than the simple spectra would. The ions and electrons are recorded in a manner, where particles possibly originating from the same individual molecule are grouped under a single coincidence event. All works in this thesis involve coincidence spectroscopy.

El.	Ion A	Ion B	Event
X	X	-	True coincidence
X	-	X	False coincidence
X	X	X	True & false coincidence
X	-	-	No coincidence
-	X	-	Random event
-	–	X	Random event
-	X	X	Random event

Table 1. Different types of PEPICO events when two molecules (A and B) are ionised during the same extraction cycle. The electron (El.) originates from molecule A by definition. Only cases with one or zero detected electrons are considered here – events triggered by an electron and pulse generator, respectively.

A scheme for a photoelectron-photoion coincidence (PEPICO) spectroscopy is shown in Figure 14. Such an experiment can also involve the detection of an electron and two ions (PEPIPICO), even more ions (the acronym is not typically extended from the previous one for convenience), or AM electrons instead of photoelectrons (AEPIPICO). The setups used in this thesis consist of a linear Wiley-McLaren ion TOF spectrometer and a hemispherical analyser.

Running the spectrometers in a coincidence mode necessitates more considerations than simply turning the instruments on simultaneously. The challenge is distinguishing true coincidences (correlated particles from the same parent) from false coincidences (non-correlated particles from different parents). Table 1 illustrates different outcomes when two molecules are ionised during the same extraction cycle. Although some events can easily be ruled as false coincidences – e.g. ion-ion coincidences that cannot originate from the same molecule – these cases are a clear minority. Usually, coincident events seem reasonable and it is impossible to say whether they are true or false.

Released electrons move faster than ions, having submicrosecond flight times to the electron detector. For comparison, a typical flight time in an ion TOF experiment is several microseconds. Electron detection can therefore act as a trigger for ion extraction. The true and false coincidences are declared versus the electron. All detected electrons are considered a part of a true coincidence whereas ions can originate from the same photoionisation event as the electron or not. The electron count rate is set around 10-50 electrons per second to decrease the likelihood of ions from different molecules being present in the source region at the start of extraction. However, data acquisition happens much more slowly than in regular ion TOF or electron spectroscopy experiments – sufficient statistics are acquired in hours instead of minutes.

The acceptance of the electron spectrometer is low. Only about one or two electrons out of a hundred will be emitted in the right direction and can be detected. The ionisation rate is therefore much higher than the electron count rate. The electron-triggered events are a mixture of true and false coincidences. Dark counts can also trigger extraction, causing false coincidences. Furthermore, some electrons are not associated with detected ions due to ion loss.

Here, the false coincidence background is treated by measuring a second dataset, where the ion extraction is triggered by a pulse generator [54]. These triggers arrive at a constant rate but are nonetheless called “random” since they are not correlated with ionisation events. The triggers are treated as false electrons and all ions coinciding with them belong to false coincidences. The two datasets are recorded simultaneously with the random triggers interleaved with electron triggers, ensuring that the experimental conditions are identical for the datasets.

3.6.2 Data Treatment

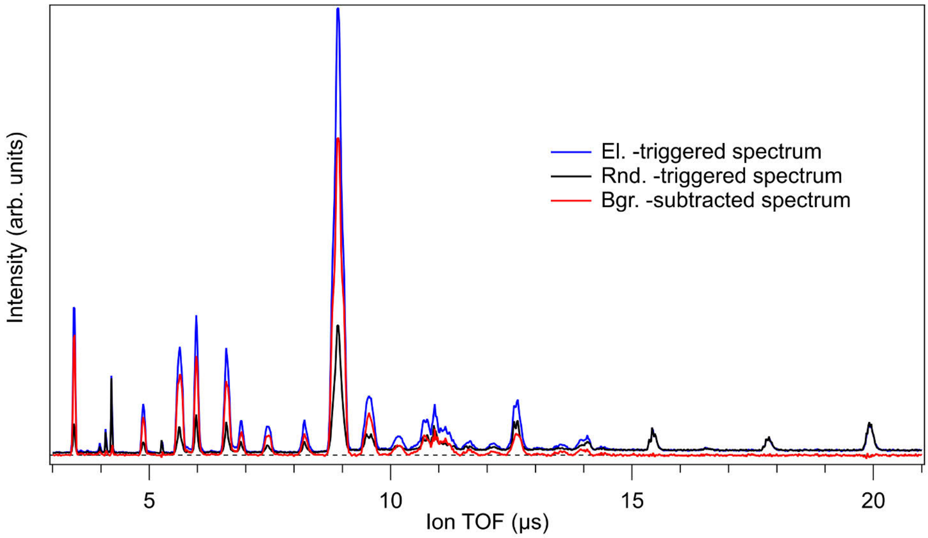

Figure 15. Electron-triggered, random-triggered, and background-subtracted TOF spectra of C_4Br_4S from a Br 3d PEPIPICO experiment, normalised to the same number of triggers. The dotted horizontal line marks zero intensity. The background-subtracted spectrum can occasionally go negative due to unequal noise in the two measured spectra. The background-subtracted TOF spectrum is the same as in Figure 10.

Treatment of ion TOF spectra is straightforward and illustrated in Figure 15. The false coincidence background in the electron-triggered TOF spectrum is assumed to be identical to the random-triggered spectrum. A background-subtracted spectrum

$S_{\text{true,n}}$ thus consists only of real coincidences and is obtained as [54]

$$S_{\text{true,n}} = \frac{S_{\text{e}}}{N_{\text{e}}} - \frac{S_{\text{rnd}}}{N_{\text{rnd}}}, \tag{40}$$

where the subscript $_{\text{n}}$ indicates triggerwise normalisation. S_{e} and S_{rnd} are the measured electron- and random-triggered TOF spectra, which are normalised by the number of electron triggers N_{e} and random triggers N_{rnd}.

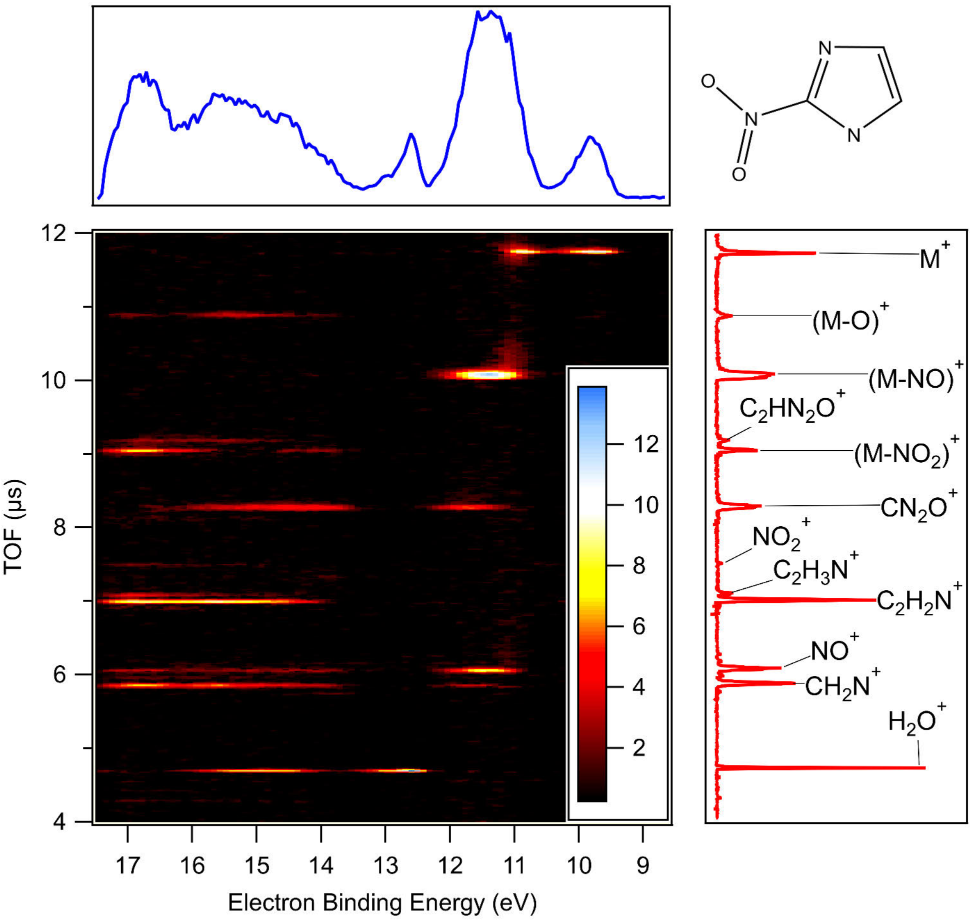

Figure 16. A PEPICO map of valence-ionised 2-nitroimidazole ($C_3H_3N_3O_2$). Coincident ion TOF and electron spectra are included for illustration. The intact parent ion is marked M^+ in the labels. All detected H_2O^+ ions are residual water based on electron binding energies [53].

Electron-ion coincidences can be illustrated with PEPICO maps, as in Figure 16. Electron binding energy is on the x-axis, ion TOF on the y-axis, and coincident electron-ion pairs form horizontal patterns. Electron and ion spectra are obtained by projecting the map on the axes. The values of the 2D bins are derived from the number of electron-ion pairs and then arbitrarily scaled to produce an easily readable false colour map.

The data for Figure 16 is from a valence PEPICO experiment of 2-nitroimidazole (a sample from **publication IV**). The map showcases the energy dependency of the dissociation: fragmentation pathways open and close as electrons are ionised from different valence MOs. This information cannot be obtained from the individual electron and ion spectra alone. The subtraction of false coincidences becomes slightly more complicated but not overly so. The normalised random-triggered TOF spectrum is subtracted from the map weighted by the electron spectrum. Alternatively, the electron-ion coincidences can be presented using ion yield curves. The curve is an electron spectrum coincident with an ion TOF range, showing the production of an ion as a function of electron binding energy. Analysing ion yield curves or PEPICO maps can reveal e.g. appearance energies of different fragments – the lowest internal energy needed to produce the fragment.

Many of the experiments here involve measuring coincidences between more than two particles. Such PEPIPICO data cannot be presented comprehensively in a single 2D map. Instead, we prepare separate PEPICO and PIPICO maps, presenting a part of the data at a time. In the PEPICO maps, possible ion-ion coincidences are not accounted for. The ion-ion coincidences are presented in PIPICO maps. The detected electron can be used as a filter, selecting only certain processes or ionisation from a certain atomic site to be included.

Figure 17 is a PIPICO map from C 1s PEPIPICO experiment of 2-nitroimidazole. On the x-axis of the map is the flight time of the faster ion, while the slower ion is on the y-axis. Ion pairs coincident with the photoelectron appear as tilted patterns. Background subtraction in PIPICO maps is much more difficult than in PEPICO maps. A precise subtraction procedure is introduced in reference [54] requiring information on e.g. detection efficiency. Lacking these, we applied a more empirical approach, where background PIPICO maps were constructed from (i) the random-triggered data and (ii) by mixing ions from the electron- and random-triggered sets. The background maps were subtracted from the electron-triggered map, fine-tuning various multiplication coefficients to reach a satisfactory result. It should be noted, that the PIPICO maps are simply for visualising the data. For instance, background subtraction for ion-pair analysis is done on list form data akin to Equation (40): random-triggered ion pairs in a pattern are subtracted from the electron-triggered ion pairs in the same pattern following a normalisation by the number of triggers.

In **publications II, IV,** and **V**, PIPICO data were analysed in two ways: i) the number of ion pairs in clearly visible patterns was calculated, normalising the total number to unity. The extracted numbers then reflect the probabilities of the system following different fragmentation pathways. ii) The PIPICO-pattern slopes were studied. The pattern orientation in Figure 17 varies, alluding to differences in fragmentation dynamics. This analysis is discussed in detail next.

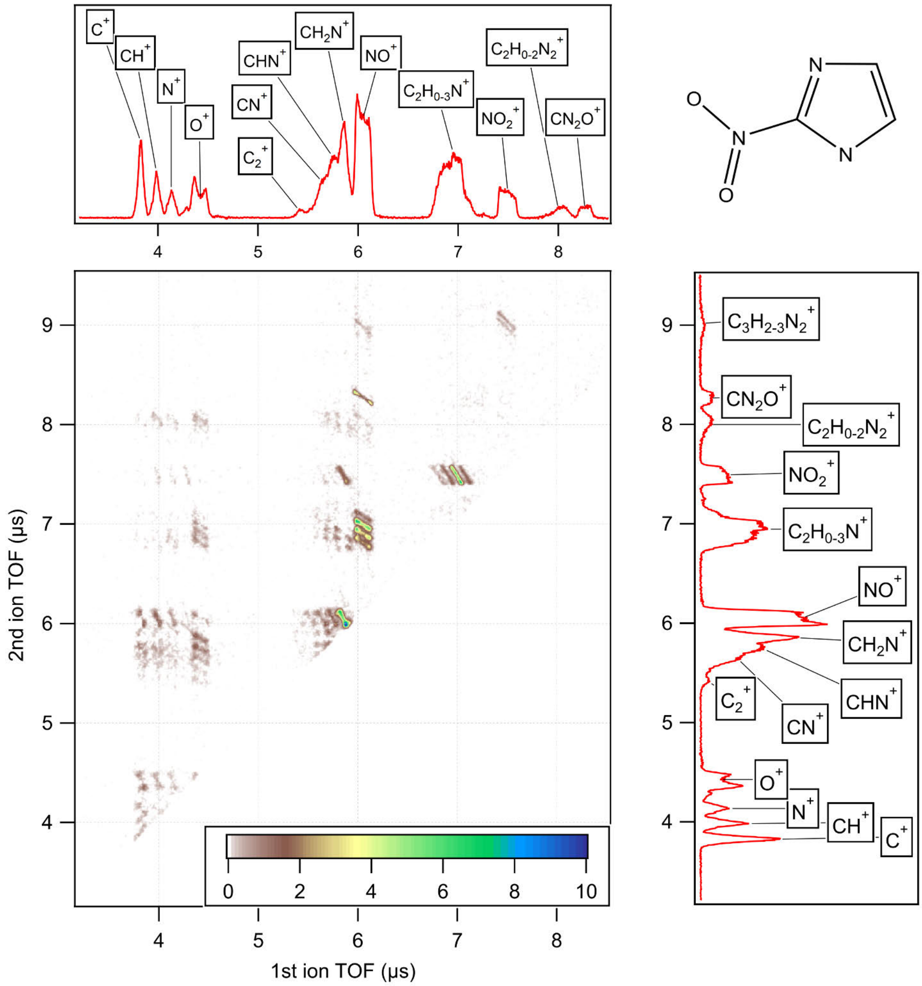

Figure 17. A PIPICO map from C 1s PEPIPICO experiment on 2-nitroimidazole. Ion pairs are coincident with the photoelectron and form tilted patterns. The coincident ion TOF spectra on the sides (the same spectrum twice) aid in interpreting the map.

PIPICO-slope analysis

When a molecule dissociates, the initial motion of sibling fragments is correlated due to the conservation of momentum. The two ionic charges repel each other and move initially in opposite directions. When the slower ion initially moves towards the detector, its flight time becomes shorter than the nominal flight time. The faster ion moves initially away from the detector, resulting in a longer flight time than the nominal one. The coincident ion pair thus appears on the lower, right-hand-side end of a pattern. If the initial velocities are reversed, the coincident event is located in the upper, left-hand-side end of the pattern. Between these cases, the initial motion has components in the radial direction. The slope of a PIPICO pattern is an indicator of the momentum distribution – not only between the two detected coincident ions but also including all other sibling fragments released from the same parent. Assuming that the momentum exchange occurs primarily through Coulomb repulsion between charged fragments, let us derive slope equations for different fragmentation pathways.

The slope k is defined as

$$k = \frac{\mathrm{d}T_2}{\mathrm{d}T_1}, \tag{41}$$

where T_1 and T_2 are the flight times of the faster and the slower fragments. However, this equation is poorly suited for analysing experimental data. A PIPICO pattern is a discontinuous conglomerate of individual events. While the pattern becomes continuous in a 2D histogram, the exact shape will likely contain irregularities. PIPICO patterns are usually oblong, but other shapes are also possible due to e.g. dissociation involving three charged particles (two of which were detected) [55], an overlap of neighbouring patterns or ion loss. Weak patterns may lack a definite structure altogether. If the studied pattern has a clear structure, the slope can be obtained in two ways: i) by rotating the pattern to find the tilt angle giving the narrowest projection. The slope is then calculated using basic trigonometry. ii) By projecting the pattern on the x- and y-axis. Writing the width of a projection as $2\Delta TOF$, the slope can be expressed as

$$k = \frac{2\Delta TOF_2}{2\Delta TOF_1} = \frac{\Delta TOF_2}{\Delta TOF_1}. \tag{42}$$

The maximum flight time deviation, obtained when the initial velocity vector is completely axial, equals ΔTOF.

- **Two-body dissociation**

The first dissociation process to be considered is the two-body dissociation:

$$\mathrm{AB}^{q_\mathrm{A}+q_\mathrm{B}} \longrightarrow \mathrm{A}^{q_\mathrm{A}} + \mathrm{B}^{q_\mathrm{B}}$$

When the two charged particles separate from one another, the conservation of momentum dictates:

$$m_\mathrm{A}\bar{v}_\mathrm{A} = -m_\mathrm{A}\bar{v}_\mathrm{A} \tag{43}$$

versus the centre of mass. Assuming the dissociation events to occur isotropically, we shall limit our considerations to the cases where the fragments separate in the axial direction. Henceforth, vector signs and the $_z$ subscripts will be dropped, as only axial velocities are used. We may write

$$\Delta TOF_{\mathrm{A}} = -\frac{m_{\mathrm{A}}v_{\mathrm{A}}}{Eq_{\mathrm{A}}} \tag{44}$$

$$\Delta TOF_{\mathrm{B}} = -\frac{m_{\mathrm{B}}v_{\mathrm{B}}}{Eq_{\mathrm{B}}} = \frac{m_{\mathrm{A}}v_{\mathrm{A}}}{Eq_{\mathrm{B}}} \tag{45}$$

by using Equation (35) and substituting U_{S}/s_0 (extraction voltage/distance from the centre of the source region to the first aperture) with E_{s} (electric field strength in the source region). Assuming that the fragment B is slower than A, the pattern slope will be

$$k = \frac{\Delta TOF_{\mathrm{B}}}{\Delta TOF_{\mathrm{A}}} = \frac{m_{\mathrm{A}}v_{\mathrm{A}}/E_{\mathrm{s}}q_{\mathrm{B}}}{-m_{\mathrm{A}}v_{\mathrm{A}}/E_{\mathrm{s}}q_{\mathrm{A}}} = -\frac{q_{\mathrm{A}}}{q_{\mathrm{B}}} \tag{46}$$

If the fragments have the same charge, the PIPICO pattern will have a slope of -1.

- **Three-body dissociation**

Three-body-dissociation processes leading to the release of two ions and a neutral fragment are slightly more complicated to handle than two-body processes since there are three main fragmentation pathways [55] to choose from:

1. Concerted (contested) dissociation:

$$\mathrm{ABC}^{q_{\mathrm{A}}+q_{\mathrm{B}}} \longrightarrow \mathrm{A}^{q_{\mathrm{A}}} + \mathrm{B}^{q_{\mathrm{B}}} + \mathrm{C}$$

All fragments are released simultaneously. The neutral fragment experiences no Coulombic repulsion, obtaining no momentum from the dissociation. Consequently, the two ions behave as if they originated from a two-body dissociation.

2. Deferred charge separation:

$$\mathrm{ABC}^{q_{\mathrm{A}}+q_{\mathrm{B}}} \longrightarrow \mathrm{AB}^{q_{\mathrm{A}}+q_{\mathrm{B}}} + \mathrm{C} \longrightarrow \mathrm{A}^{q_{\mathrm{A}}} + \mathrm{B}^{q_{\mathrm{B}}} + \mathrm{C}$$

Deferred charge separation is a two-step process, where the neutral fragment is released in the first step, followed by the separation of the two ions in the second phase. Again, the neutral fragment is released before the Coulombic repulsion, resulting in no additional momentum for either the neutral or the multiply-charged fragments. The slope for the PIPICO pattern is still given by Equation (46).

3. Secondary dissociation

$$\mathrm{ABC}^{q_\mathrm{A}+q_\mathrm{B}} \longrightarrow \mathrm{A}^{q_\mathrm{A}} + \mathrm{BC}^{q_\mathrm{B}} \longrightarrow \mathrm{A}^{q_\mathrm{A}} + \mathrm{B}^{q_\mathrm{B}} + \mathrm{C}$$

In secondary dissociation, the charge separation occurs first and the neutral fragment is released in the second phase. Invoking the conservation of momentum:

$$m_\mathrm{A} v_\mathrm{A} = -m_\mathrm{BC} v_\mathrm{BC} \tag{47}$$

$$m_\mathrm{B} v_\mathrm{B} + m_\mathrm{C} v_\mathrm{C} = m_\mathrm{BC} v_\mathrm{BC} \tag{48}$$

The first stage occurs in the axial direction. The second step of the dissociation happens after the ionic fragments A and BC have obtained all the momentum they can from their mutual repulsion. The second step could occur in the radial directions, but there is no Coulombic repulsion between the charged and the neutral fragments. Therefore $\bar{v}_\mathrm{B} \approx \bar{v}_\mathrm{C} \approx \bar{v}_\mathrm{BC}$, and can all be considered axial. The flight time spread for the cation A is given by Equation (44), while for B we can write

$$\Delta TOF_\mathrm{B} = -\frac{m_\mathrm{B} v_\mathrm{B}}{E_\mathrm{s} q_\mathrm{B}} \approx -\frac{m_\mathrm{B} v_\mathrm{BC}}{E_\mathrm{s} q_\mathrm{B}} = \frac{m_\mathrm{B}}{E_\mathrm{s} q_\mathrm{B}} \frac{m_\mathrm{A} v_\mathrm{A}}{m_\mathrm{BC}}. \tag{49}$$

At this point, there are two options. If fragment A is the faster ion,

$$k = \frac{\Delta TOF_\mathrm{B}}{\Delta TOF_\mathrm{A}} \approx -\frac{m_\mathrm{B} m_\mathrm{A} v_\mathrm{A} / E_\mathrm{s} q_\mathrm{B} m_\mathrm{BC}}{m_\mathrm{A} v_\mathrm{A} / E_\mathrm{s} q_\mathrm{A}} = -\frac{m_\mathrm{B}}{m_\mathrm{BC}} \frac{q_\mathrm{A}}{q_\mathrm{B}}. \tag{50}$$

Because $m_\mathrm{B} < m_\mathrm{BC}$, the pattern slope becomes less steep than what it would be otherwise. If fragment A is the slower ion, ΔTOF_A and ΔTOF_B merely switch places resulting in

$$k = \frac{\Delta TOF_\mathrm{A}}{\Delta TOF_\mathrm{B}} \approx \frac{m_\mathrm{BC}}{m_\mathrm{B}} \frac{q_\mathrm{B}}{q_\mathrm{A}} \tag{51}$$

and the slope becomes steeper than earlier.

- **Four-body dissociation**

Four-body dissociation ups the complexity, but the slope equations can still be derived by following the earlier approach. However, the derivation becomes more tedious with each added step. Yet, neutral fragments released before the Coulombic repulsion do not affect the slope, and the problem may be reduced to the three- or two-body dissociation cases. Now, as an example, we shall derive a slope equation for the following dissociation process:

$$\mathrm{ABCD}^{q_\mathrm{A}+q_\mathrm{D}} \longrightarrow \mathrm{AB}^{q_\mathrm{A}} + \mathrm{CD}^{q_\mathrm{D}} \longrightarrow \mathrm{A}^{q_\mathrm{A}} + \mathrm{B} + \mathrm{C} + \mathrm{D}^{q_\mathrm{D}}$$

Approximating $\bar{v}_\mathrm{A} \approx \bar{v}_\mathrm{AB}$ and $\bar{v}_\mathrm{D} \approx \bar{v}_\mathrm{CD}$, we may write

$$m_\mathrm{AB} v_\mathrm{AB} = -m_\mathrm{CD} v_\mathrm{CD} \tag{52}$$

$$m_\mathrm{AB} v_\mathrm{AB} = m_\mathrm{A} v_\mathrm{A} + m_\mathrm{B} v_\mathrm{B} \tag{53}$$

$$m_\mathrm{CD} v_\mathrm{CD} = m_\mathrm{C} v_\mathrm{C} + m_\mathrm{D} v_\mathrm{D}. \tag{54}$$

and subsequently

$$\Delta TOF_{\mathrm{A}} = -\frac{m_{\mathrm{A}} v_{\mathrm{A}}}{E_{\mathrm{s}} q_{\mathrm{A}}} \approx -\frac{m_{\mathrm{A}} v_{\mathrm{AB}}}{E_{\mathrm{s}} q_{\mathrm{A}}} \tag{55}$$

$$\Delta TOF_{d} = -\frac{m_{\mathrm{D}} v_{\mathrm{D}}}{E_{\mathrm{s}} q_{\mathrm{D}}} \approx -\frac{m_{\mathrm{D}} v_{\mathrm{CD}}}{E_{\mathrm{s}} q_{\mathrm{D}}} = \frac{m_{\mathrm{D}}}{E_{\mathrm{s}} q_{\mathrm{D}}} \frac{m_{\mathrm{AB}} v_{\mathrm{AB}}}{m_{\mathrm{CD}}} \tag{56}$$

If we assume that the ion D is slower than ion A, the slope equation becomes

$$k = \frac{\Delta T_d}{\Delta T_a} \approx -\frac{m_{\mathrm{D}} m_{\mathrm{AB}} v_{\mathrm{AB}} / E_{\mathrm{s}} m_{\mathrm{CD}} q_{\mathrm{D}}}{m_{\mathrm{A}} v_{\mathrm{AB}} / E_{\mathrm{s}} q_{\mathrm{A}}} = -\frac{m_{\mathrm{D}}}{m_{\mathrm{A}}} \frac{m_{\mathrm{AB}}}{m_{\mathrm{CD}}} \frac{q_{\mathrm{A}}}{q_{\mathrm{D}}} \tag{57}$$

and in the opposite case, we obtain the reciprocal of the earlier slope value.

- **Generalised secondary dissociation model**

The above simple model cannot sometimes connect an ion pair to a fragmentation pathway. The generalised secondary dissociation (GSD) model of **publication III** replaces the infinite secondary dissociation distance with a finite one. This is the distance between the charged fragments before the ejection of a neutral species. By varying the distance, GSD allows a smooth transition from concerted dissociation to secondary dissociation.

4 Research Context

4.1 Studies on Nitroimidazoles

Radiotherapy uses X-rays or energetic particles to damage cancerous cells. While targeted at tumour cells, some damage is also inflicted on neighbouring healthy cells. Minimisation of this collateral damage is essential. The total radiation dose can be administered in small increments and the tumour can be radiated from different angles. Selectivity of radiotherapy towards malignant cells can also be improved using various radiosensitizers, such as certain nitroimidazoles [56; 57]. **Publications I, IV,** and **V** explore photodissociation dynamics of six nitroimidazole molecules, shown in Figure 18. The underlying molecular-level sensitizing mechanisms are still not fully understood and it is not straightforward to say what makes a molecule a radiosensitizer. For example, 5-iodo-4-thio-2'-deoxyuridine is an efficient radiosensitizing agent while 5-bromo-4-thio-2'-deoxyuridine is not [58]. Clinical trials are expensive and time-consuming – molecules upon molecules cannot be blindly tested to find the most effective radiosensitizer drug. A deeper understanding of relevant dynamics may aid in finding promising drug candidates.

X-rays can damage cells directly by ionising important biomolecules such as DNA. However, most damage is done indirectly by ionising water molecules [56; 59]. The released energetic electrons can interact with further water molecules, starting a cascade of radiolysis that produces reactive hydroxyl radicals $OH^\bullet$. These radicals are then responsible for DNA damage. The free electrons themselves can also induce DNA damage, even at kinetic energies below ionisation thresholds [60]. Solid cancerous tumours are characteristically hypoxic – having a partial pressure of oxygen below a tissue-specific physiological level – due to insufficient oxygen supply and deregulated demand [61–63]. Unfortunately, hypoxia increases resistance against radiotherapy. According to the oxygen fixation hypothesis, the presence of oxygen makes DNA damage irreparable (permanent or "fixed") [59]. Reactive hydroxyl radicals $OH^\bullet$ cause damage creating $DNA^\bullet$ radicals, which the cell can revert to the original state. Oxygen can interact with these radicals, forming peroxy radicals $(DNA)O_2^\bullet$ that are much harder to repair. Hypoxic tumours need higher radiation doses to achieve the desired therapeutic effect, increasing the risk of unwanted side effects.

Under the oxygen fixation hypothesis, nitroimidazole radiosensitizers are oxygen

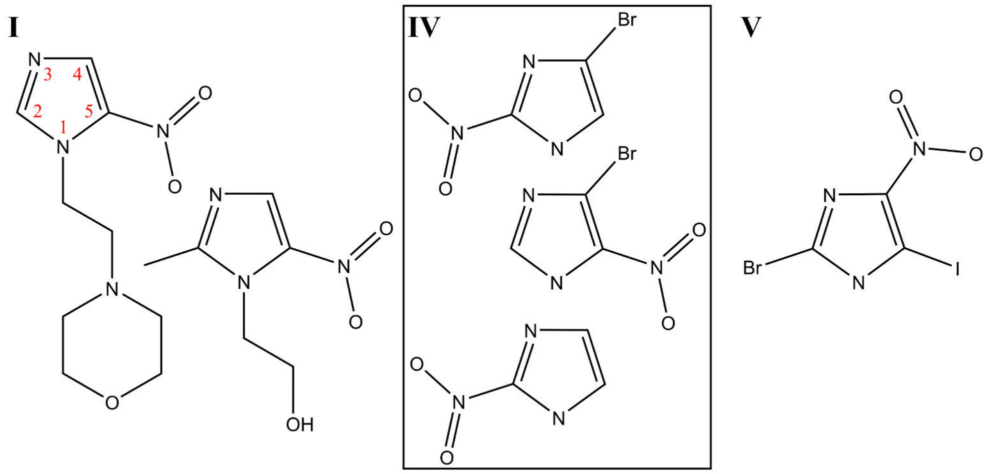

Figure 18. The structural formulae of the six nitroimidazoles studied in original **publications I, IV,** and **V**. The molecules in **I** are nimorazole ($C_9H_{14}N_4O_3$, on the left) and metronidazole ($C_6H_9N_3O_3$). The structural formula of nimorazole also includes the atom numbering for the imidazole ring. The three samples in **IV** are 4-bromo-2-nitroimidazole ($C_3H_2BrN_3O_2$), 4-bromo-5-nitroimidazole ($C_3H_2BrN_3O_2$), and 2-nitroimidazole ($C_3H_3N_3O_2$) in descending order. Finally, 2-bromo-5-iodo-4-nitroimidazole ($C_3HBrIN_3O_2$) was studied in **publication V**.

mimetics – agents mimicking oxygen in making DNA damage unrepairable [57; 64]. These compounds have high electron affinities and can permeate hypoxic tissue better than oxygen, which is constantly used in cellular respiration. Therefore, oxygen mimetics are well-suited for the treatment of hypoxic tumours. Nitroimidazole radiosensitizers undergo enzymatic and radiation-induced redox reactions [64]. When “activated” under irradiation, they release agents that promote unrepairable DNA damage. Among other reactive radical species, interest has been placed especially on NO, a potent radiosensitizer acting through multiple pathways [64; 65].

Heavy elements also act as radiosensitizers [57; 66; 67]. Having larger photoabsorption cross sections than light elements, heavy elements create an X-ray absorption “hot spot” among the soft tissue. The absorbed energy is then deposited into the surroundings via photoelectrons, AM electrons, secondary photons, and energetic ionic fragments from a Coulomb explosion.

The photoelectric effect is a viable interaction method for only low-energy medical X-rays in the keV range. Above 33.2 keV photon energy, iododeoxyuridine reaches the maximum dose enhancement ratio at around 50 keV due to the high photoabsorption cross section of iodine [68]. X-rays like these are used e.g. to treat skin cancer, as the maximum dose is obtained at a depth of a few mm from the surface [69]. For MeV range medical X-rays, the interaction with matter occurs via the Compton effect.

A study by Krause et al. indicated iodinated nitroimidazoles having a greater *in vitro* radiosensitization effect on human colonic adenocarcinoma cells than non-halogenated ones [70]. Yet, the mechanisms behind the increased efficacy remain uncertain. Do nitroimidazoles retain their potential radiosensitization effect, while being enhanced by the heavy element, creating a bi-functional radiosensitizer? Or should the effect be attributed solely to the heavy element or the cytotoxicity of the molecule?

In addition to the works presented here, there have been multiple studies probing the excited-state dynamics of nitroimidazoles in recent years [71–88]. However, a well-known open question remains: to what degree do the dynamics in small gas-phase molecules represent the processes occurring in a cellular environment [3]? Experiments on isolated molecules greatly simplify the interpretations regarding sensitization mechanisms that can be made relying on fundamental physics. In clinical trials or *in vitro* studies, the molecular-level processes cannot be tracked to the same degree as in gas-phase studies. Yet, only clinical trials may answer questions regarding e.g. radiosensitization effectiveness, biostability and tolerability. For instance, misonidazole – a potent nitroimidazole radiosensitizer – was found to cause neuropathy and the radiosensitization effects were lost at clinically tolerable drug doses [64].

The environment may greatly affect dissociation dynamics versus *in vacuo* dynamics. Microhydration of isolated uracil and thymine nucleobases prevents dissociative electron attachment due to very low-energy ($\leq$ 3eV) electrons, instead resulting in stable anionic parent. Neighbouring molecules also make intermolecular relaxation pathways (ICD and ETMD) operable. Environmental effects on the dissociation of nitroimidazoles could potentially be studied using coincidence methods by employing water-radiosensitizer clusters [89; 90].

Although the choice of molecules is strongly motivated by cancer treatment, it is worth emphasising that the work here is fundamental research on photoinduced dynamics. How do the sample molecules dissociate? How does the dissociation differ between effective and ineffective radiosensitizers? Where do the differences stem from? Can dissociation dynamics explain radiosensitization capabilities? What makes an effective radiosensitizer? In this thesis, these questions are considered from a physicist's point of view. No claims are made regarding the applicability or effectiveness of the sample molecules as radiosensitizers.

4.2 Studies on Thiophenes

Various thiophene compounds make an excellent target for the fundamental research of photoinduced dynamics. Firstly, thiophene (C_4H_4S) exhibits rich dynamics and the small size enables conducting very detailed studies. Investigations have revealed, for instance, ultrafast ring-opening dynamics via a conical intersection [91–101]. Being relatively small molecules, accurate *ab initio* calculations can also be car-

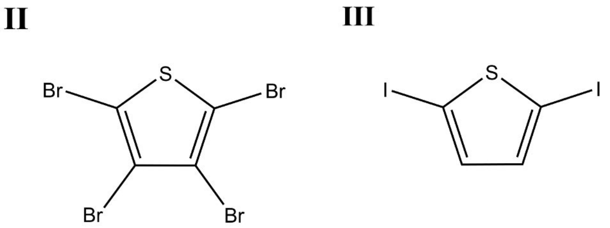

Figure 19. Molecular structures of the two thiophene samples. Tetrabromothiophene (C_4Br_4S) was investigated in **publication II** and diiodothiophene ($C_4H_2I_2S$) in **III**.

ried out to interpret the complex dynamics. Secondly, thiophene lends itself well to various systematic studies. For example, oligothiophenes formed by linking/fusing thiophene monomers, allow studying how the dynamics change as the size of the molecule increases.

Two halogenated thiophenes investigated in **publications II** and **III** – tetrabromothiophene and diiodothiophene – are shown in Figure 19. The bromine and iodine atoms offer additional X-ray absorption sites on the molecule compared to thiophene. By targeting different core orbitals, photodissociation dynamics can be started with the positive charge initially localised on different parts of the sample molecules. The structures also offer an interesting setup for ensuing dynamics: the rigid thiophene ring is trapped between heavy halogen atoms. Especially in the case of tetrabromothiophene, the ring can be thought to reside in an "inertial cage". It has been shown that under multiphoton ionisation, the carbon atoms experience a Coulomb "implosion", trapped in place by the bromine atoms [98]. Here, we set out to investigate what is the role of the inertial cage on dissociation dynamics upon a single core-ionisation event.

As a secondary motivation, thiophenes are versatile compounds. Thiophene, its derivatives, oligothiophenes, polythiophenes, and other thiophene-containing materials display a wide array of present and potential applications in different fields: biodiagnostics, medicine, organic electronics, and photovoltaics to name a few [102–110]. To properly harness these prospects, the properties of thiophenes must be well understood. The applicability of polythiophenes as organic semiconductors, for instance, makes charge migration dynamics across small thiophene units an interesting research topic.

5 Summary of the Publications

5.1 Publication I

Fragmentation Patterns of Radiosensitizers Metronidazole and Nimorazole upon Valence Ionization

We studied the valence-ionisation-induced dissociation of nimorazole and metronidazole. The experimental findings were complemented with simulations, concentrating on the major fragmentation pathways. Both molecules are radiosensitizers, but nimorazole is a more effective one [64]. We focussed our analysis on aspects potentially explaining the disparity between the radiosensitization capabilities – mainly the release of NO and NO_2. The former is a radiosensitizing agent while the latter is a strong oxidizer.

Nimorazole dissociates primarily by cleaving a C-C bond in the intramolecular carbon bridge between the two ring structures:

$$\mathrm{C_9H_{14}N_4O_3}^+ \longrightarrow \mathrm{C_5H_{10}NO^+} + \mathrm{C_4H_4N_3O_2}.$$

According to our simulations, this simple pathway has a transition state of only 0.46 eV above the vertical ionisation potential. Furthermore, we have observed dissociation products corresponding to minor pathways. Fragments with m/q = 113 u/e are due to the separation of the rings, albeit with cleavage of a C-N bond instead of the C-C bond. Light ions (40, 42, 55, and 56 u/e) are also discovered. The left half of Figure 20 illustrates our interpretation of the dissociation dynamics.

Unlike nimorazole, metronidazole exhibits a rich fragmentation landscape. The right half of Figure 20 presents our suggestions for the major dissociation pathways. The one coincident with the lowest binding energy photoelectrons (appearing at around 9.8 eV binding energy) involves a hydrogen migration and the subsequent release of nitrous acid NOOH. Pathways leading to the release of NO_2 emerge above approximately 12.2 eV binding energies. Simulating the molecule, we discovered minimum-energy pathways that agree reasonably with the experimental appearance energies.

NOOH is a less reactive species than radical NO_2. As the NOOH pathway has lower appearance energy than the NO_2 one, we can potentially explain the poor radiosensitization capabilities of metronidazole. Low-energy electrons are more nu-

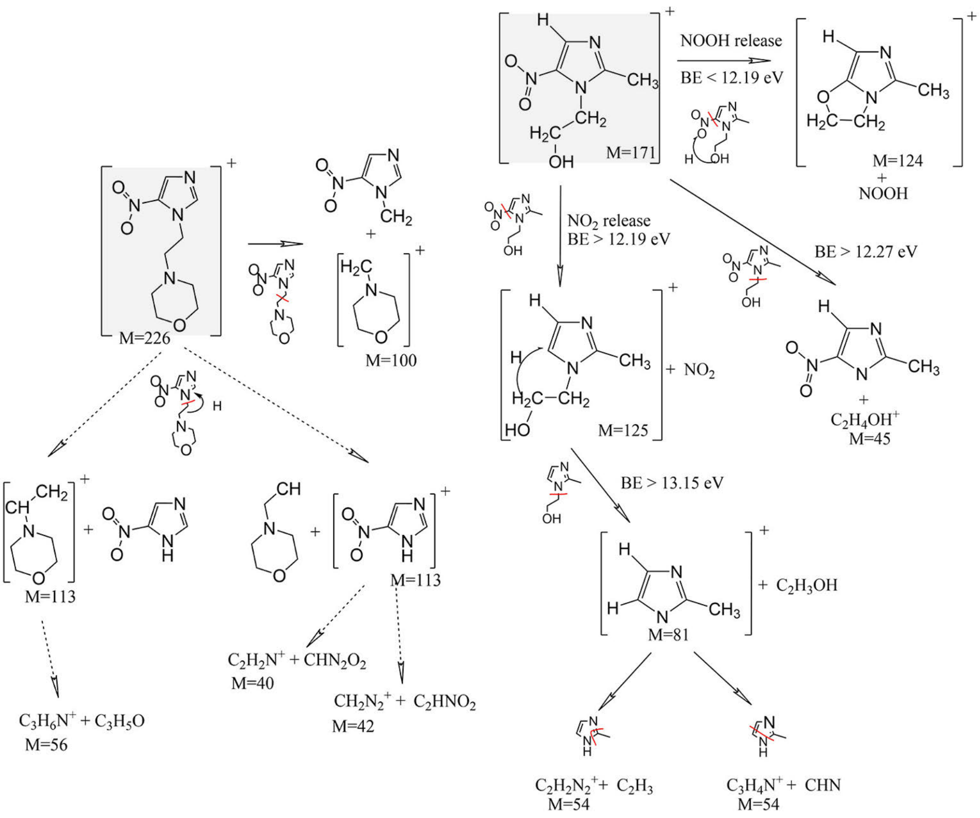

Figure 20. Left: All fragmentation pathways of nimorazole upon valence ionisation, dashed arrows representing minor pathways. Right: Major fragmentation pathways of metronidazole upon valence ionisation. The intact parent cations are highlighted in grey. Adapted with permission from **publication I**. Copyright 2020 American Chemical Society.

merous than high-energy electrons in an irradiated cellular environment, making the release of NOOH more probable than NO_2 release.

Nimorazole showcased no NO, NO_2, or even NOOH release. However, the molecule is a precursor of dehydrogenated 1-methyl-5-nitroimidazole via the primary pathway. 5-nitroimidazole is known to release NO_2 and NO^+ upon secondary dissociation [83]. However, methylation or protonation may affect the dissociation dynamics greatly, and the dehydrogenated methylnitroimidazole should be investigated separately for its radiosensitization potential.

This study revealed that our two samples followed notably different fragmentation schemes. The release of $C_5H_{10}NO^+$ dominates the fragmentation landscape of nimorazole whereas metronidazole exhibits a variety of major pathways. The differences may explain why nimorazole is superior to metronidazole as a radiosensitizer.

5.2 Publication II

Photodissociation Dynamics of Halogenated Aromatic Molecules: the Case of Core-Ionized Tetrabromothiophene

We investigated the photodissociation dynamics of tetrabromothiophene C_4Br_4S (the C_4S ring is referred to as R and any of its fragments as R_f in this work), conducting various experiments: i) PEPIPICO upon Br 3d, C 1s, and S 2p ionisation. All three led primarily to the creation of dicationic states. Analysis was focused on the Br 3d dataset, while the other two were used to study ionisation-site-dependent effects on dissociation. ii) PEPIPICO upon Br 3p ionisation. iii) Non-coincident ion TOF upon valence ionisation. iv) AEPIPICO upon Br 3d ionisation.

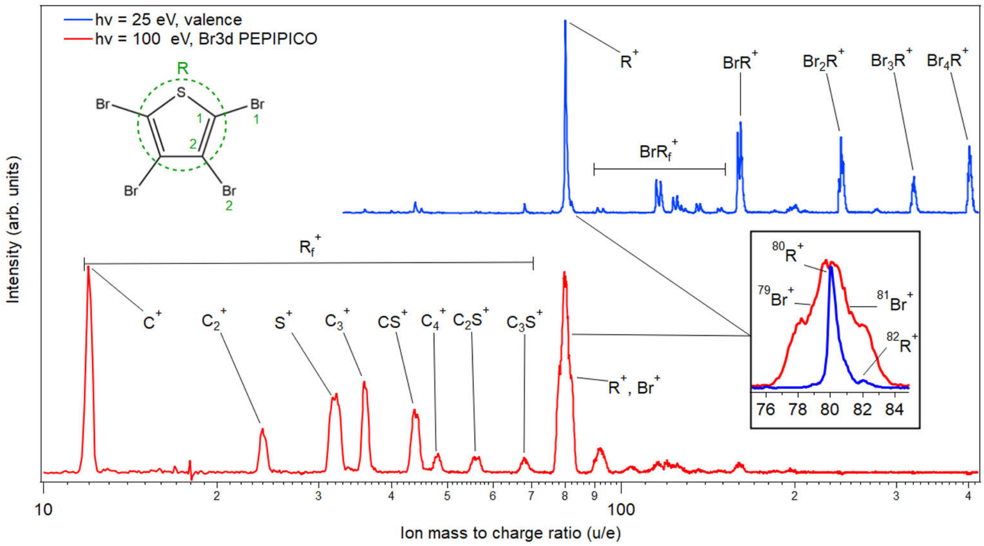

Figure 21. Ion mass spectra of tetrabromothiophene upon valence (top) and Br 3d ionisation (bottom). The lower spectrum is from a PEPIPICO experiment and the contribution of false coincidences has been removed. The peak at 80 u/e corresponds to purely R^+ in the top spectrum. In the bottom spectrum, the structure consists of Br^+ and potentially R^+. The skeletal structure labels symmetrically unique Br and C atoms. Reproduced from **publication II** with permission from the PCCP Owner Societies.

Figure 21 shows the ion mass spectra measured following valence and Br 3d ionisation. The valence-ionised states tend to dissociate by ejecting neutral Br atoms while the thiophene ring R usually remains intact. Moving to core ionisation, the number of small fragments increases notably and Br^+ ions are also produced. A closer analysis of the Br 3d PEPIPICO data showed that approximately 82% of the true-coincidence ion pairs contain at least one Br^+ ion. Eight (R_f^+, Br^+) pairs constituted 43% of the total and we proposed fragmentation pathways for each one using PIPICO-slope analysis. Six out of eight pairs (with R_f^+ being C^+, C_2^+, C_3^+, C_4^+,

C_2S^+, or C_3S^+) corresponded reasonably well with the pathway:

$$\begin{aligned}\mathrm{Br_4R^{++}} &\rightarrow \mathrm{3\,Br + BrR^{++}} \rightarrow \mathrm{3\,Br + Br^+ + R^+} \\ &\rightarrow \mathrm{3\,Br + Br^+ + (R_f{}^+ + R_f)}.\end{aligned}$$

Meanwhile, (S^+, Br^+) aligned with the pathway:

$$\begin{aligned}\mathrm{Br_4R^{++}} &\rightarrow \mathrm{Br_3C_3 + BrCS^{++}} \rightarrow \mathrm{Br_3C_3 + Br^+ + CS^+} \\ &\rightarrow \mathrm{Br_3C_3 + Br^+ + (C + S^+)}.\end{aligned}$$

Finally for (CS^+, Br^+), we proposed the pathway:

$$\begin{aligned}\mathrm{Br_4R^{++}} &\rightarrow \mathrm{3\,Br + BrR^{++}} \rightarrow \mathrm{3\,Br + BrC^+ + C_3S^+} \\ &\rightarrow \mathrm{3\,Br + (C + Br^+) + (C_2 + CS^+)}.\end{aligned}$$

The model above suggests that neutral bromine atoms or bromine-containing fragments are first separated from a dication. The first step is then followed by charge separation and secondary dissociation.

Although not marked in the mass spectrum, we detected some $Br_{1\text{-}4}R^{++}$ dications – a direct evidence of the neutral-Br-loss dynamics. We extracted appearance energies for these dications and various cation groups from the Br 3d AEPIPICO data. Then, we combined all the analysis thus far into the “dissociation tree” model of Figure 22. The release of neutral Br atoms, which characterised dissociation upon valence ionisation, is also important in dicationic dissociation. The “inertial cage” of Br atoms seems to impede ring fragmentation, making the neutral-bromine loss the preferred first step. We compared ion production between the Br 3d, C 1s and S 2p PEPIPICO datasets and concluded that the dissociation tree model developed for Br 3d agrees reasonably well with the other two cases.

Despite the general similarities in ion production between Br 3d, C 1s and S 2p ionisation, some differences exist. Interestingly, the production of stable parent dication is approximately ten times higher after C 1s ionisation and 5 times higher after S 2p than after Br 3d. To explain the discrepancy, we simulated molecular dynamics in the core-hole states. The core ionisation induces changes in bond lengths, with the largest effects observed with Br 3d. The ionisation of either of two chemically inequivalent Br atoms induces significant C-Br bond stretching. C 1s ionisation results in the smallest impact with the vibrational excitations being notably weaker and more uniformly spread out over different bonds. The S 2p ionisation causes the extension of C-S bonds and contraction of the nearest C-Br bonds. The system moves along a core-hole-state PES starting from the equilibrium geometry of the electronic ground state hopping to a dicationic-state PES via AM decay. Since we are interested in the parent dication, we only consider the scenario where the AM decay transfers the system to the dicationic ground state. Figure 23 shows the change in the energy

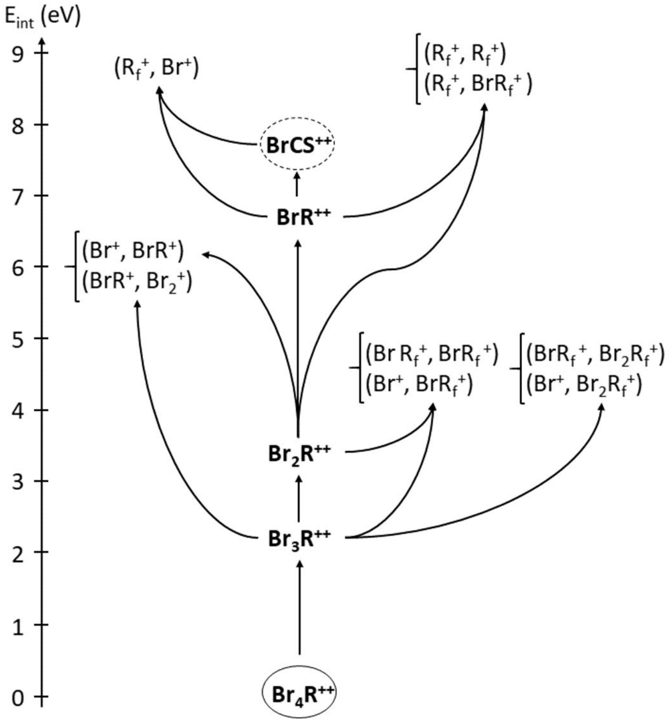

Figure 22. The proposed dissociation tree model for the main fragmentation pathways of dicationic tetrabromothiophene with neutral fragments omitted. The vertical positions of ion pairs and dications reflect their appearance energies versus the double ionisation potential. Intermediary produce $CBrS^{++}$ was not detected but its presence was hinted by PIPICO-slope analysis. Reproduced from **publication II** with permission from the PCCP Owner Societies.

of the dicationic system as a function of time from the core-ionisation. Regardless of how long the system stays in the C 1s-core-hole state, the dynamics leave the energy largely unaffected. Much larger changes in energy occur in the Br 3d and S 2p core-hole states. The core-hole lifetimes are unknown in tetrabromothiophene, yet we have included estimations based on other small molecules. By the time these points have passed, the differences developed in energy between the core-hole states are rather small. However, 1/e ($\approx$ 37%) of the population remains after one core-hole lifetime. Larger energy differences are obtained when remaining longer in the core-hole states.

As a summary, we proposed a dissociation tree model for the dicationic tetrabromothiophene. Furthermore, we investigated differences in the survival of the parent dication between Br 3d, C 1s, and S 2p ionisation. Based on simulations, the system may populate less stable regions of the dicationic-ground-state PES after dynamics in a core-hole state. This is reflected in the likelihood of parent dication being detected.

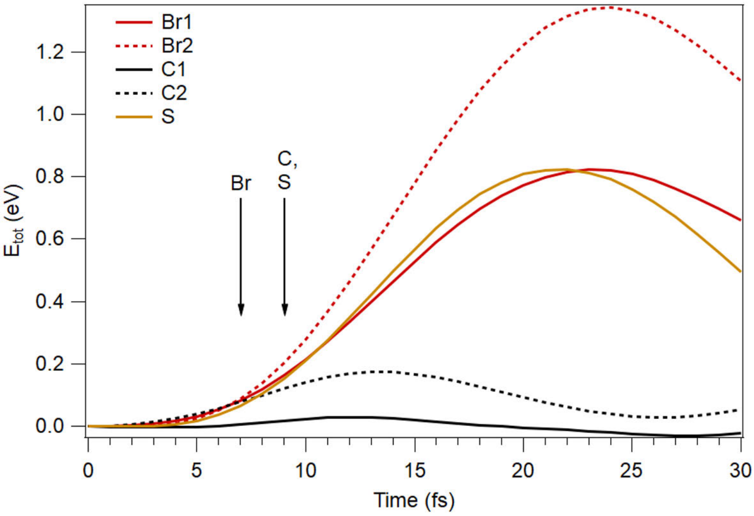

Figure 23. Dicationic-ground-state energy after molecular dynamics in a core-hole state and AM decay. Zero corresponds to the energy in the neutral ground state geometry and the arrows mark estimated core-hole lifetimes. The atomic sites are illustrated in Figure 21. Reproduced from **publication II** with permission from the PCCP Owner Societies.

5.3 Publication III

Energy-Dependent Timescales in the Dissociation of Diiodothiophene Dication

In the third work, we investigated 2,5-diiodothiophene $C_4H_2I_2S$ (we refer to the C_4H_2S structure as R in this work) by measuring I 4d PEPIPICO, I 4d AEPIPICO, and a non-coincident TOF spectrum upon valence ionisation.

The valence-ionised sample dissociates primarily into R^+ – the intact $C_4H_2S^+$. The other important fragments are $C_3H_2^+$, $(R{-}H)^+$ and RI^+. There is also a notable probability of the parent cation staying intact.

Ring fragmentation becomes more prevalent upon I 4d ionisation and many coincidences are made with an I^+ fragment. The intact parent dications are only produced by the lowest-internal-energy-dicationic states. Dissociation begins as the internal energy increases – (R^+, I^+) pathway appears first and the M^{++} signal disappears. Pathways involving ring fragmentation become operable as the internal energy increases further.

We analysed in more detail the following major fragmentation pathway:

$$\mathrm{RI_2}^{++} \longrightarrow \mathrm{R}^+ + \mathrm{I}^+ + \mathrm{I}.$$

Based on slope analysis, deferred charge separation and concerted dissociation result in a slope of -1, while secondary dissociation leads to -2.55. These slopes correspond

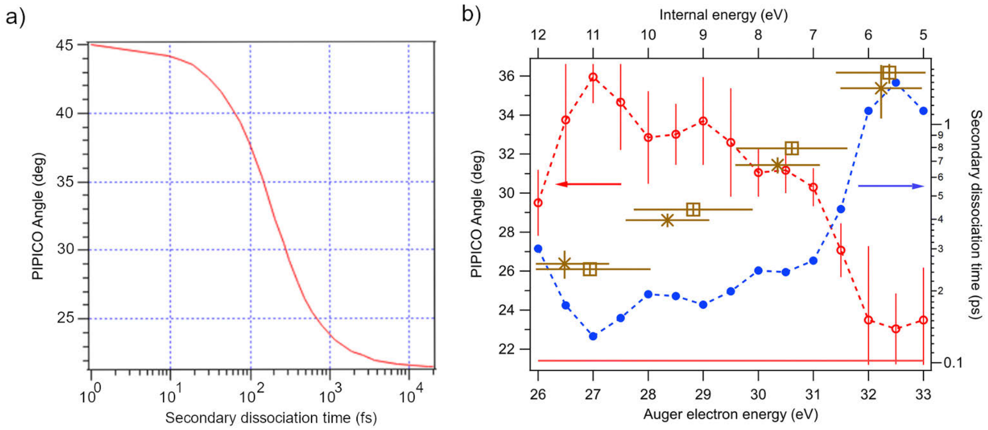

Figure 24. a) The tilt angle of (R^+, I^+) as a function of secondary-dissociation time predicted by the GSD model. b) The red circles show the experimental tilt angle of (R^+, I^+) pattern as a function of internal energy while the blue dots show the corresponding secondary dissociation times. The red horizontal line highlights the limit of pure secondary dissociation. The brown markers with error bars show the secondary dissociation times from simulations: × without and □ with forces returning atoms to the molecular plane. Adapted from **publication III** with permission from the PCCP Owner Societies.

to tilt angles of $45°$ and $21.4°$, respectively, from the vertical. The pattern of the studied pathway does not align with either of the cases. Instead, it lies somewhere in between the two. Further analysis showed the pattern rotating as a function of internal energy.

Since the two-step-dissociation model could not explain the experimental findings, we introduced the general secondary dissociation (GSD) model. There, a finite secondary dissociation time was adopted instead of an infinite one. Figure 24a) shows the PIPICO-pattern tilt angle changing smoothly from concerted dissociation to pure secondary dissociation as the secondary dissociation time increases. Figure 24b) illustrates the experimental tilt angle of the pattern (red curve) as a function of internal energy. The blue curve shows the corresponding secondary dissociation times. At the highest-recorded internal energies, the tilt angle decreases. In this region, new competing fragmentation pathways are opening, and the (R_2^+, I^+) pattern has become diffuse.

The dissociation dynamics were also simulated, reaching a fair quantitative agreement with the experiment. Figure 24b) shows the simulated secondary dissociation times with brown markers in two distinct cases: the simulation was run both with and without forces that returned atoms to the molecular plane. In both cases, the simulations replicate the trend shown by the blue curve.

We extracted information regarding the temporal evolution of the dissociation dynamics without conducting a time-resolved experiment. Although the dissociation timescales are sensitive to the initial conditions, our results indicate that precise knowledge of the electronic structure may not be essential for accurate modelling. Instead, a satisfactory representation of the bond-breaking timescales can be achieved by adjusting the internal energy in the simulation.

5.4 Publication IV

Photodissociation of Bromine-Substituted Nitroimidazole Radiosensitizers

We conducted a comparative study between 4-bromo-2-nitroimidazole (4Br2Nim), 4-bromo-5-nitroimidazole (4Br5Nim), and 2-nitroimidazole (2Nim). The setup allowed us to simultaneously study the effects of bromination (4Br2Nim vs. 2Nim) and the location of the nitro group (4Br2Nim vs. 4Br5Nim) on the photodissociation dynamics. We used Br 3d, C 1s, and N 1s ionisation to create dicationic states.

We extracted the number of ion pairs in each PIPICO pattern, calculating branching fractions for ion pairs and individual ions. These are the probabilities for an ion or a pair to be released. Further analysis focused on Br^+ and ionic fragments related to the nitro group: N^+, O^+, NO^+, and $NO_2{}^+$. Generally, the branching fractions from ionising different core orbitals on the same molecule are similar – within a few percentage points from one another. Therefore, a mean branching fraction over all three ionisation sites is a reasonable way of comparing the samples. The mean branching fractions are presented in Figure 25. In addition to the single ion branching fractions, we have calculated two additional parameters. SUM1 is the combined branching fraction of ion pairs that contain at least one N^+, NO^+, $NO_2{}^+$, or O^+ ion. It is an indicator of charge localisation in the nitro group. SUM2 extends this sum to include Br^+. It reflects the likelihood of dicationic dissociation resulting in the release of ionic fragments that could cause a radiosensitization effect. Differences between 4Br2Nim and 4Br5Nim are minor, with 4Br2Nim exhibiting slightly more charge localisation on the nitro group (SUM1). 4Br5Nim shows more Br^+ release. Comparison with 2Nim shows that bromination slightly inhibits the production of nitro-related ionic fragments yet the effect is not drastic.

Furthermore, we continued our analysis towards the direction of fundamental quantum chemistry. N 1s photoelectron binding energies from different nitrogen atoms were chemically shifted. The photoelectron peaks did not overlap, allowing us to filter the data based on which N 1s site was ionised. Interestingly, differences in the single ion branching fractions were larger between ionisation of different N 1s sites than different photoionisation edges altogether.

Due to increased photoionisation cross-sections, possibility of AM cascades, and the high yield of potentially harmful ionic fragments (SUM2), we concluded that halogenated nitroimidazoles show potential as radiosensitizers from a photodissociation point of view.

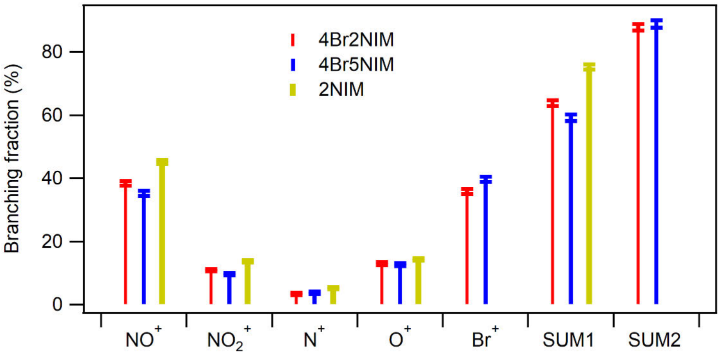

Figure 25. Comparison of mean branching fractions of five ions over the Br 3d, C 1s, and N 1s ionisation cases. Parameter SUM1 reflects the likelihood that an ion pair contains at least one of four leftmost ions. Parameter SUM2 is calculated similarly and includes all five ions. Differences between the brominated samples are minor. Reproduced from **publication IV** with permission from the PCCP Owner Societies.

5.5 Publication V

Shell-Dependent Photofragmentation Dynamics of a Heavy-Atom-Containing Bifunctional Nitroimidazole Radiosensitizer

In the final work of this thesis, we investigated the photodissociation dynamics of 2-bromo-5-iodo-4-nitroimidazole (BrINim) upon I 4d, Br 3d, and I 3d ionisation. The first two ionisations primarily result in dicationic states and we refer to these cases as “shallow core” ionisation. We approximated the population distribution of dicationic and tricationic states to be 81% vs. 19% after I 4d ionisation and 70% vs. 30% after Br 3d. The “deep core” – I 3d – ionisation creates more highly charged states. Ion mass spectra from the PEPIPICO experiments are shown in Figure 26a). As expected, the deep core ionisation showcases more rigorous dissociation as the number of atomic fragments increases drastically from the shallow core ionisations. Differences between I 4d and Br 3d experiments are less pronounced but present: the four most abundant ions are NO$^+$, C_2N^+, Br$^+$, and I$^+$ although in different orders. The most significant factor causing the differences is likely the charge state, although ionisation-site-dependent effects cannot be ruled out completely.

The mass spectrum from the deep core ionisation shows clear signs of ion loss, most notably with N$^+$ and O$^+$. In Figure 26b) we show the peak areas from the uncorrected spectra in solid bars. The dotted bars show the estimated amount of lost bromine-free ions, obtained by applying ion-loss-correction methods detailed section 3.4.2.

We simulated the dissociation dynamics for the charge states $q = +2$ e and

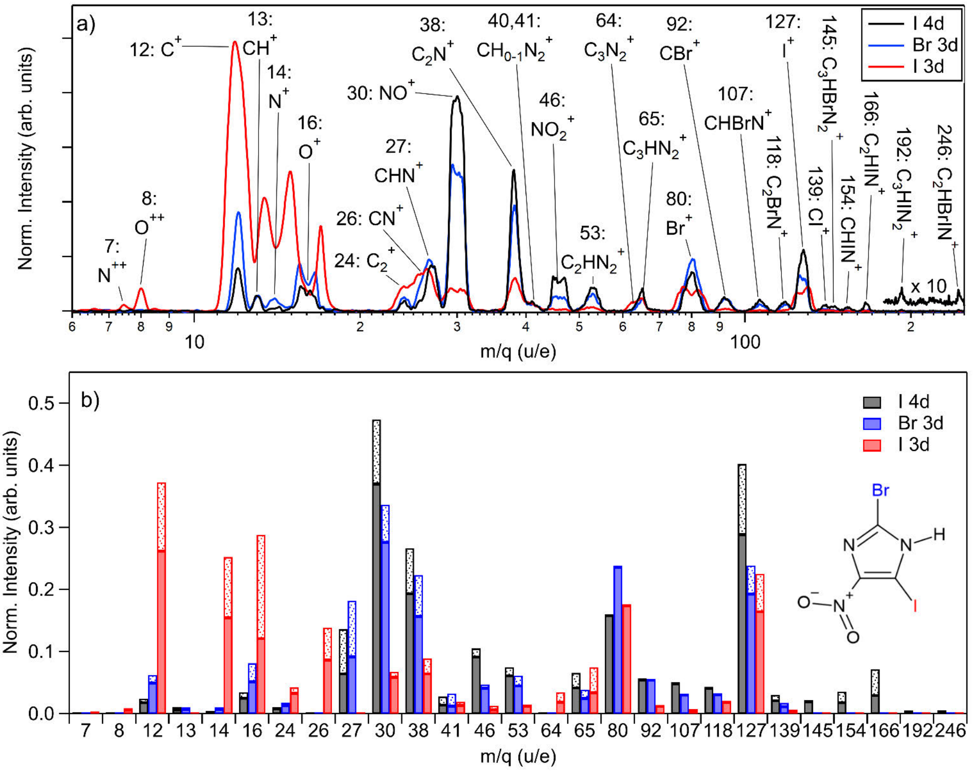

Figure 26. a) Ion mass spectra of BrINim from I 4d, Br 3d, and I 3d PEPIPICO datasets. False coincidence backgrounds have been subtracted and the spectra are normalised trigger-wise. Due to ion loss, the lineshapes of N^+ and O^+ are distorted in the I 3d experiment. b) The solid bars show peak areas extracted from the spectra above. The patterned bars are an estimate of lost ions. The m/q value of Br was assigned to 80, representing the average mass of the two isotopes. Reproduced from **publication V** with permission from the PCCP Owner Societies.

$q = +4$ e, replicating the observed trends such as the increasing amount of atomic fragments when going from shallow core to deep core ionisation. Yet, discrepancies also exist. Some can be explained by the fact that all secondary dissociation pathways might not be captured before the simulated trajectories are terminated.

Thus far, we have only considered individual molecules in the gas phase. We turned to simulations to estimate the potential radiosensitization effect in a cellular environment, carrying out molecular dynamics simulations of an oxygen ion in water. Oxygen was selected as i) it had the highest average kinetic energy upon I 3d ionisation and ii) it was produced in large quantities. The kinetic energy of the oxygen ion increased as deeper electrons were ionised. However, the increase in kinetic energy does extend the distance travelled from the source – “the radius of damage” – by the same factor. Instead, the fragment-water collisions become more energetic and the first few water molecules obtain more energy.

Halogenated nitroimidazole radiosensitizers can act as radiation-absorption hotspots. When radiation is targeted at deep core orbitals such as I 1s, AM electrons and energetic ionic fragments are released. Charged atomic fragments are chemically very reactive and can inflict cellular damage. The simulations suggest that neighbouring water molecules quickly slowed down the cationic fragments. These interactions can ionise water molecules, creating a build-up of water radicals in addition to the ones created by electrons. As more energy is released per unit volume, the radiation hot spot becomes hotter.

6 Conclusion

In this thesis, the photodissociation of eight molecules (nimorazole, metronidazole, tetrabromothiophene, diiodothiophene, 2-nitroimidazole, 4-bromo-5-nitroimidazole, 4-bromo-2-nitroimidazole, and 2-bromo-5-iodo-4-nitroimidazole) is studied using coincidence spectroscopy. The results show rich dissociation dynamics.

A better understanding of how nitroimidazoles and halogenated nitroimidazoles dissociate may help the search for new radiosensitizer drugs. We have investigated the dynamics in the gas phase, yet radiosensitizer drugs are used *in vivo* – not *in vacuo*. The effects of the cellular environment on dissociation remain an open question. However, tracking the dynamics *in vivo* or even *in vitro* is a hopelessly challenging undertaking. In the final article of this thesis, we took our first step along the research avenue, where the potential radiosensitizing mechanisms of nitroimidazoles in an environment are investigated. The considerations were made based on simulations but future experiments are possible. The environmental effects can be included in the dynamics at least partially by utilising e.g. water-radiosensitizer clusters or aerosols. However, experimental setups are more complicated than here and data analysis becomes more challenging as the size of the sample increases. Distinguishing the role of the environment can be aided by detailed models of dynamics on isolated molecules.

The two studies on small halogenated thiophenes provide a stepping stone towards researching the photodissociation dynamics of halogenated oligothiophenes such as bithiophenes and terthiophenes. Charge-transfer dynamics can be studied in incrementally larger oligomers, providing a basis for model testing. A lone halogen atom in the structure acts as a way to localise the initial charge on a certain part of the molecule. This allows for further control over the study of dynamics. For example, oligothiophenes contain multiple carbon atoms so the initial charge may be in various locations following a C 1s ionisation.

All the experiments here are time-independent. Nonetheless, some information on the time evolution of the dynamics was concluded through analysis. Continuing the studies of this thesis with time-resolved pump-probe experiments (e.g. [100]) could provide an interesting research avenue, as the early dynamics after photoionisation are often defining for the ensuing dissociation.

List of References

[1] G. Wald. Molecular Basis of Visual Excitation. *Science*, 162(3850):230–239, 1968.

[2] S. Mai and L. González. Molecular Photochemistry: Recent Developments in Theory. *Angewandte Chemie International Edition*, 59(39):16832–16846, 2020.

[3] K. Ueda, E. Sokell, S. Schippers, F. Aumayr, H. Sadeghpour, J. Burgdörfer, C. Lemell, X.-M. Tong, T. Pfeifer, F. Calegari, A. Palacios, F. Martin, P. Corkum, G. Sansone, E. Gryzlova, A. Grum-Grzhimailo, M. N. Piancastelli, P. Weber, T. Steinle, K. Amini, J. Biegert, N. Berrah, E. Kukk, R. Santra, A. Müller, D. Dowek, R. R. Lucchese, McCudry C. W., P. Bolognesi, L. Avaldi, T. Jahnke, M. S. Schöffler, R. Dörner, Y. Mairesse, L. Nahon, O. Smirnova, T. Schlathölter, E. E. B. Campbell, J.-M. Rost, M. Meyer, and K. A. Tanaka. Roadmap on photonic, electronic and atomic collision physics I. Light-matter interaction. *Journal of Physics B Atomic Molecular and Optical Physics*, 52:171001, 2019.

[4] T. Arion and U. Hergenhahn. Coincidence spectroscopy: Past, present and perspectives. *Journal of Electron Spectroscopy and Related Phenomena*, 200:222–231, 2015.

[5] H. Sato. Photodissociation of Simple Molecules in the Gas Phase. *Chemical Reviews*, 101(9): 2687–2726, 2001.

[6] A. Zewail. Femtochemistry: Atomic-Scale Dynamics of the Chemical Bond. *The Journal of Physical Chemistry A*, 104(24):5660–5694, 2000.

[7] E. Schrödinger. An Undulatory Theory of the Mechanics of Atoms and Molecules. *Physical Review*, 28(6):1049–1070, 1926.

[8] P. W. Atkins and R. S. Friedman. *Molecular Quantum Mechanics*. Oxford University Press, fifth edition, 2011.

[9] M. Born. Zur Quantenmechanik der Stoßvorgänge. *Zeitschrift für Physik*, 37(12):863–867, 1926.

[10] R. Mulliken. Spectroscopy, Molecular Orbitals, and Chemical Bonding. *Science*, 157(3784): 13–24, 1967.

[11] W. Demtröder. *Atoms, Molecules and Photons*. Springer, third edition, 2018.

[12] J. A. Bearden and A. F. Burr. Reevaluation of X-Ray Atomic Energy Levels. *Reviews of Modern Physics*, 39(1):125–142, 1967.

[13] J. C. Fuggle and N. Mårtensson. Core-level binding energies in metals. *Journal of Electron Spectroscopy and Related Phenomena*, 21(3):275–281, 1980.

[14] T. H. Dunning Jr. Gaussian basis sets for use in correlated molecular calculations. i. the atoms boron through neon and hydrogen. *The Journal of Chemical Physics*, 90(2):1007–1023, 1989.

[15] R. A. Kendall, T. H. Dunning Jr, and R. J. Harrison. Electron affinities of the first-row atoms revisited. systematic basis sets and wave functions. *The Journal of Chemical Physics*, 96(9): 6796–6806, 1992.

[16] F. Neese. The orca program system. *Wiley Interdisciplinary Reviews: Computational Molecular Science*, 2(1):73–78, 2012.

[17] F. Neese, F. Wennmohs, U. Becker, and C. Riplinger. The orca quantum chemistry program package. *The Journal of chemical physics*, 152(22):224108, 2020.

[18] F. Neese. Software update: The orca program system—version 5.0. *Wiley Interdisciplinary Reviews: Computational Molecular Science*, 12(5):e1606, 2022.

[19] K. Fukui. Role of Frontier Orbitals in Chemical Reactions. *Science*, 218(4574):747–754, 1982.

[20] U. Hergenhahn, O. Kugeler, A. Rüdel, E. E. Rennie, and A. M. Bradshaw. Symmetry-Selective Observation of the N 1s Shape Resonance in N2. *The Journal of Physical Chemistry A*, 105(23): 5704–5708, 2001.

[21] M. S. Schöffler, J. Titze, N. Petridis, T. Jahnke, K. Cole, L. Ph. H. Schmidt, A. Czasch, D. Akoury, O. Jagutzki, J. B. Williams, N. A. Cherepkov, S. K. Semenov, C. W. McCurdy, T. N. Rescigno, C. L. Cocke, T. Osipov, S. Lee, M. H. Prior, A. Belkacem, A. L. Landers, H. Schmidt-Böcking, Th. Weber, and R. Dörner. Ultrafast Probing of Core Hole Localization in N2. *Science*, 320(5878):920–923, 2008.

[22] E. Kukk, K. Ueda, U. Hergenhahn, X.-J. Liu, G. Prümper, H. Yoshida, Y. Tamenori, C. Makochekanwa, T. Tanaka, M. Kitajima, and H. Tanaka. Violation of the Franck-Condon Principle due to Recoil Effects in High Energy Molecular Core-Level Photoionization. *Physical Review Letters*, 95(13):133001, 2005.

[23] K. Siegbahn, C. Nordling, A. Fahlman, R. Nordberg, K. Hamrin, J. Hedman, G. Johansson, T. Bergmark, S.-E. Karlsson, I. Lindgren, and B. Lindberg. *ESCA: Atomic, Molecular and Solid State Structure Studies by Means of Electron Spectroscopy*. Nova acta Regiae Societatis Scientiarum Upsaliensis. Almqvist & Wiksell, 1967.

[24] O. Travnikova, K. J. Børve, M. Patanen, J. Söderström, C. Miron, L. J. Sæthre, N. Mårtensson, and S. Svensson. The ESCA molecule—Historical remarks and new results. *Journal of Electron Spectroscopy and Related Phenomena*, 185(8):191–197, 2012.

[25] T. Helgaker, P. Jørgensen, and J. Olsen. *Molecular Electronic-Structure Theory*. John Wiley & Sons, 2000.

[26] M. Orio, D. A. Pantazis, and F. Neese. Density functional theory. *Photosynthesis Research*, 102 (2):443–453, 2009.

[27] D. R. Yarkony. Conical Intersections: The New Conventional Wisdom. *J. Phys. Chem. A*, 105 (26):6277–6293, 2001.

[28] N. Berrah. Molecular dynamics induced by short and intense x-ray pulses from the LCLS. *Physica Scripta*, 2016(T169):014001, 2016.

[29] T Koopmans. Über die Zuordnung von Wellenfunktionen und Eigenwerten zu den Einzelnen Elektronen Eines Atoms. *Physica*, 1(1):104–113, 1934.

[30] B. L. Henke, E. M. Gullikson, and J. C. Davis. X-Ray Interactions: Photoabsorption, Scattering, Transmission, and Reflection at E = 50-30,000 eV, Z = 1-92. *Atomic Data and Nuclear Data Tables*, 54(2):181–342, 1993.

[31] H. Kang, K. T. Lee, B. Jung, Y. J. Ko, and S. K. Kim. Intrinsic lifetimes of the excited state of dna and rna bases. *Journal of the American Chemical Society*, 124(44):12958–12959, 2002.

[32] W. J. Schreier, T. E. Schrader, F. O. Koller, P. Gilch, C. E. Crespo-Hernández, V. N. Swaminathan, T. Carell, W. Zinth, and B. Kohler. Thymine Dimerization in DNA Is an Ultrafast Photoreaction. *Science*, 315(5812), 2007.

[33] L. Meitner. Über die Entstehung der β-Strahl-Spektren radioaktiver Substanzen. *Zeitschrift für Physik*, 9(1):131–144, 1922.

[34] L. Meitner. Das β-Strahlenspektrum von UX1 und seine Deutung. *Zeitschrift für Physik*, 17(1): 54–66, 1923.

[35] P. Auger. Sur les rayons β secondaires produits dans un gaz par des rayons X. *Comptes rendus hebdomadaires des séances de l'Académie des Sciences*, 177:169, 1923.

[36] C. Nicolas and C. Miron. Lifetime broadening of core-excited and -ionized states. *Journal of Electron Spectroscopy and Related Phenomena*, 185(8):267–272, 2012.

[37] T. Jahnke, U. Hergenhahn, B. Winter, R. Dörner, U. Frühling, P. V. Demekhin, K. Gokhberg, L. S. Cederbaum, A. Ehresmann, A. Knie, and A. Dreuw. Interatomic and Intermolecular Coulombic Decay. *Chemical Reviews*, 120(20):11295–11369, 2020.

[38] T. A. Field and J. H. D. Eland. Lifetimes of metastable molecular doubly charged ions. *Chemical Physics Letters*, 211(4):436–442, 1993.

[39] A. Fontell, J. Maula, R. Nieminen, C. Söderlund, K. Valli, A. Vehanen, M. Vulli, and M. Ylilammi. *Tyhjiötekniikka*. Suomen tyhjiöseura ry, 1986.

[40] W. L. Wiese and J. R. Fuhr. Accurate atomic transition probabilities for hydrogen, helium, and lithium. *Journal of physical and chemical reference data*, 38(3):565–720, 2009.

[41] R. Pärna, R. Sankari, E. Kukk, E. Nõmmiste, M. Valden, M. Lastusaari, K. Kooser, K. Kokko, M. Hirsimäki, S. Urpelainen, P. Turunen, A. Kivimäki, V. Pankratov, L. Reisberg, F. Hennies, H. Tarawneh, R. Nyholm, and M. Huttula. FinEstBeaMS – A wide-range Finnish-Estonian Beamline for Materials Science at the 1.5GeV storage ring at the MAX IV Laboratory. *Nuclear Instruments and Methods in Physics Research Section A: Accelerators, Spectrometers, Detectors and Associated Equipment*, 859:83–89, 2017.

[42] K. Chernenko, A. Kivimäki, R. Pärna, W. Wang, R. Sankari, M. Leandersson, H. Tarawneh, V. Pankratov, M. Kook, E. Kukk, L. Reisberg, S. Urpelainen, T. Käämbre, F. Siewert, G. Gwalt, A. Sokolov, S. Lemke, S. Alimov, J. Knedel, O. Kutz, T. Seliger, M. Valden, M. Hirsimäki, M. Kirm, and M. Huttula. Performance and characterization of the FinEstBeAMS beamline at the MAX IV Laboratory. *Journal of Synchrotron Radiation*, 28(5):1620–1630, 2021.

[43] Albert Hofmann. *The Physics of Synchrotron Radiation*. Cambridge University Press, 2004.

[44] G. Margaritondo. A Primer in Synchrotron Radiation: Everything You Wanted to Know about SEX (Synchrotron Emission of X-rays) but Were Afraid to Ask. *Journal of Synchrotron Radiation*, 2(3):148–154, 1995.

[45] S. Sasaki, K. Kakuno, T. Takada, T. Shimada, K. Yanagida, and Y. Miyahara. Design of a new type of planar undulator for generating variably polarized radiation. *Nuclear Instruments and Methods in Physics Research Section A: Accelerators, Spectrometers, Detectors and Associated Equipment*, 331(1):763–767, 1993.

[46] K. Kooser, A. Kivimäki, P. Turunen, R. Pärna, L. Reisberg, M. Kirm, M. Valden, M. Huttula, and E. Kukk. Gas-phase endstation of electron, ion and coincidence spectroscopies for diluted samples at the FinEstBeAMS beamline of the MAX IV 1.5 GeV storage ring. *Journal of Synchrotron Radiation*, 27(4):1080–1091, 2020.

[47] E. De Hoffmann and V. Stroobant. *Mass spectrometry: principles and applications*. John Wiley & Sons, 2007.

[48] W. C. Wiley and I. H. McLaren. Time-of-flight mass spectrometer with improved resolution. *Review of Scientific Instruments*, 26(12):1150–1157, 1955.

[49] O. Jagutzki, A. Cerezo, A. Czasch, R. Dorner, M. Hattas, Min Huang, V. Mergel, U. Spillmann, K. Ullmann-Pfleger, T. Weber, H. Schmidt-Bocking, and G.D.W. Smith. Multiple hit readout of a microchannel plate detector with a three-layer delay-line anode. *IEEE Transactions on Nuclear Science*, 49(5):2477–2483, 2002.

[50] D. P. Seccombe and T. J. Reddish. Theoretical study of space focusing in linear time-of-flight mass spectrometers. *Review of Scientific Instruments*, 72(2):1330–1338, 2001.

[51] J. L. Wiza. Microchannel plate detectors. *Nucl. Instrum. Methods*, 162(1-3):587–601, 1979.

[52] S. Hüfner. *Photoelectron Spectroscopy*. Advanced Texts in Physics. Springer, Berlin, Heidelberg, 2003.

[53] K. Kimura, S. Katsumata, Y. Achiba, T. Yamazaki, and S. Iwata. *Handbook of HeI Photoelectron Spectra of Fundamental Organic Molecules: Ionization Energies, Ab Initio Assignments, and Valence Electronic Structure for 200 Molecules*. Japan Scientific Societies Press, 1981.

[54] G. Prümper and K. Ueda. Electron–ion–ion coincidence experiments for photofragmentation of polyatomic molecules using pulsed electric fields: Treatment of random coincidences. *Nuclear Instruments and Methods in Physics Research Section A: Accelerators, Spectrometers, Detectors and Associated Equipment*, 574(2):350–362, 2007.

[55] J. H. D. Eland. Dynamics of fragmentation reactions from peak shapes in multiparticle coincidence experiments. *Laser Chemistry*, 11(3-4):259–263, 1991.

[56] H. Wang, X. Mu, H. He, and X.-D. Zhang. Cancer Radiosensitizers. *Trends in Pharmacological Sciences*, 39(1):24–48, 2018.

[57] L. Gong, Y. Zhang, C. Liu, M. Zhang, and S. Han. Application of Radiosensitizers in Cancer Radiotherapy. *International Journal of Nanomedicine*, 16:1083–1102, 2021.

[58] P. Spisz, M. Zdrowowicz, S. Makurat, W. Kozak, K. Skotnicki, K. Bobrowski, and J. Rak. Why does the type of halogen atom matter for the radiosensitizing properties of 5-halogen substituted 4-thio-2-deoxyuridines? *Molecules*, 24(15), 2019.

[59] D. R. Grimes and M. Partridge. A mechanistic investigation of the oxygen fixation hypothesis and oxygen enhancement ratio. *Biomedical physics & engineering express*, 1(4):045209, 2015.

[60] B. Boudaïffa, P. Cloutier, D. Hunting, M. A. Huels, and L. Sanche. Resonant Formation of DNA Strand Breaks by Low-Energy (3 to 20 eV) Electrons. *Science*, 287(5458):1658–1660, 2000.

[61] M. Höckel and P. Vaupel. Tumor Hypoxia: Definitions and Current Clinical, Biologic, and Molecular Aspects. *JNCI: Journal of the National Cancer Institute*, 93(4):266–276, 2001.

[62] W. R. Wilson and M. P. Hay. Targeting hypoxia in cancer therapy. *Nature Reviews Cancer*, 11 (6):393–410, 2011.

[63] I. Telarovic, R. H. Wenger, and M. Pruschy. Interfering with Tumor Hypoxia for Radiotherapy Optimization. *Journal of Experimental & Clinical Cancer Research*, 40(1):197, 2021.

[64] B. Oronsky, S. Knox, and J. Scicinski. Six Degrees of Separation: The Oxygen Effect in the Development of Radiosensitizers. *Translational Oncology*, 4(4):189–198, 2011.

[65] J. Scicinski, B. Oronsky, S. Ning, S. Knox, D. Peehl, M. M. Kim, P. Langecker, and G. Fanger. NO to cancer: The complex and multifaceted role of nitric oxide and the epigenetic nitric oxide donor, RRx-001. *Redox Biology*, 6:1–8, 2015.

[66] K. Kobayashi, N. Usami, E. Porcel, S. Lacombe, and C. Le Sech. Enhancement of radiation effect by heavy elements. *Mutation Research/Reviews in Mutation Research*, 704(1):123–131, 2010.

[67] J. Choi, G. Kim, S. B. Cho, and H.-J. Im. Radiosensitizing high-Z metal nanoparticles for enhanced radiotherapy of glioblastoma multiforme. *Journal of Nanobiotechnology*, 18(1):122, 2020.

[68] S. J. Karnas, E. Yu, R. C. McGarry, and J. J. Battista. Optimal photon energies for IUdR K-edge radiosensitization with filtered x-ray and radioisotope sources. *Physics in Medicine and Biology*, 44(10):2537–2549, 1999.

[69] R. Hill, B. Healy, L. Holloway, Z. Kuncic, D. Thwaites, and C. Baldock. Advances in kilovoltage x-ray beam dosimetry. *Physics in Medicine & Biology*, 59(6):R183, 2014.

[70] W. Krause, A. Jordan, R. Scholz, and J.-L. M. Jimenez. Iodinated Nitroimidazoles as Radiosensitizers. *Anticancer Research*, 25(3B):2145–2151, 2005.

[71] K. Tanzer, L. Feketeová, B. Puschnigg, P. Scheier, E. Illenberger, and S. Denifl. Reactions in Nitroimidazole Triggered by Low-Energy (0–2 eV) Electrons: Methylation at N1-H Completely Blocks Reactivity. *Angewandte Chemie International Edition*, 53(45):12240–12243, 2014.

[72] L. Feketeová, A. L. Albright, B. S. Sørensen, M. R. Horsman, J. White, R. A. J. O'Hair, and N. Bassler. Formation of radical anions of radiosensitizers and related model compounds via electrospray ionization. *International Journal of Mass Spectrometry*, 365-366:56–63, 2014.

[73] K. Tanzer, L. Feketeová, B. Puschnigg, P. Scheier, E. Illenberger, and S. Denifl. Reactions in Nitroimidazole and Methylnitroimidazole Triggered by Low-Energy (0–8 eV) Electrons. *The Journal of Physical Chemistry A*, 119(25):6668–6675, 2015.

[74] P. Bolognesi, A. R. Casavola, A. Cartoni, R. Richter, P. Markus, S. Borocci, J. Chiarinelli, S. Tošić, H. Sa'adeh, M. Masič, B.P. Marinković, K.C. Prince, and L. Avaldi. Communication: "Position" does matter: The photofragmentation of the nitroimidazole isomers. *The Journal of Chemical Physics*, 145(19):191102, 2016.

[75] A. Ribar, K. Fink, M. Probst, S. E. Huber, L. Feketeová, and S. Denifl. Isomer Selectivity in Low-Energy Electron Attachment to Nitroimidazoles. *Chemistry – A European Journal*, 23(52): 12892–12899, 2017.

[76] S. Pandeti, L. Feketeová, T. J. Reddy, H. Abdoul-Carime, B. Farizon, M. Farizon, and D. T. Märk. Nitroimidazolic radiosensitizers investigated by electrospray ionization time-of-flight mass spectrometry and density functional theory. *RSC Advances*, 7(71):45211–45221, 2017.

[77] E. Itälä, K. Tanzer, S. Granroth, K. Kooser, S. Denifl, and E. Kukk. Fragmentation patterns of 4(5)-nitroimidazole and 1-methyl-5-nitroimidazole—The effect of the methylation. *Journal of Mass Spectrometry*, 52(11):770–776, 2017.

[78] A. Cartoni, A. R. Casavola, P. Bolognesi, M. C. Castrovilli, D. Catone, J. Chiarinelli, R. Richter, and L. Avaldi. Insights into 2- and 4(5)-Nitroimidazole Decomposition into Relevant Ions and Molecules Induced by VUV Ionization. *The Journal of Physical Chemistry A*, 122(16):4031–4041, 2018.

[79] E. Itälä, S. Granroth, D. T. Ha, K. Kooser, H. Levola, E. Rachlew, K. Tanzer, and E. Kukk. Fragmentation of imidazole, pyrimidine and purine induced by core ionization: Significance of small-scale chemical environment. *Journal of Photochemistry and Photobiology A: Chemistry*, 356:283–289, April 2018.

[80] M. Mendes, G. García, M.-C. Bacchus-Montabonel, and P. Limão-Vieira. Electron Transfer Induced Decomposition in Potassium–Nitroimidazoles Collisions: An Experimental and Theoretical Work. *International Journal of Molecular Sciences*, 20(24):6170, 2019.

[81] P. Bolognesi, V. Carravetta, L. Sementa, G. Barcaro, S. Monti, P. Manjari Mishra, A. Cartoni, M. C. Castrovilli, J. Chiarinelli, S. Tosic, B. P. Marinkovic, R. Richter, and L. Avaldi. Core Shell Investigation of 2-nitroimidazole. *Frontiers in Chemistry*, 7, 2019.

[82] S. Pandeti, J. Ameixa, J. M. Khreis, L. Feketeová, F. Chirot, T. J. Reddy, H. Abdoul-Carime, F. Ferreira da Silva, S. Denifl, R. A. J. O'Hair, B. Farizon, M. Farizon, and T. D. Märk. Decomposition of protonated ronidazole studied by low-energy and high-energy collision-induced dissociation and density functional theory. *The Journal of Chemical Physics*, 151(16):164306, 2019.

[83] E. Itälä, H. Myllynen, J. Niskanen, J. González-Vázquez, Y. Wang, D. T. Ha, S. Denifl, and E. Kukk. Controlling NO Production Upon Valence Ionization of Nitroimidazoles. *The Journal of Physical Chemistry A*, 123(14):3074–3079, 2019.

[84] J. Chiarinelli, A. R. Casavola, M. C. Castrovilli, P. Bolognesi, A. Cartoni, F. Wang, R. Richter, D. Catone, S. Tosic, B. P. Marinkovic, and L. Avaldi. Radiation Damage Mechanisms of Chemotherapeutically Active Nitroimidazole Derived Compounds. *Frontiers in Chemistry*, 7, 2019.

[85] R. Meißner, L. Feketeová, A. Ribar, K. Fink, P. Limão-Vieira, and S. Denifl. Electron Ionization of Imidazole and Its Derivative 2-Nitroimidazole. *Journal of the American Society for Mass Spectrometry*, 30(12):2678–2691, 2019.

[86] M. Satta, A. R. Casavola, A. Cartoni, M. C. Castrovilli, D. Catone, J. Chiarinelli, S. Borocci, L. Avaldi, and P. Bolognesi. Ionization of 2- and 4(5)-Nitroimidazoles Radiosensitizers: A "Kinetic Competition" Between NO2 and NO Losses. *ChemPhysChem*, 22(23):2387–2391, 2021.

[87] A. I. Lozano, L. Álvarez, A. García-Abenza, C. Guerra, F. Kossoski, J. Rosado, F. Blanco, J. C. Oller, M. Hasan, M. Centurion, T. Weber, D. S. Slaughter, D. M. Mootheril, A. Dorn, S. Kumar, P. Limão-Vieira, R. Colmenares, and G. García. Electron Scattering from 1-Methyl-5-Nitroimidazole: Cross-Sections for Modeling Electron Transport through Potential Radiosensitizers. *International Journal of Molecular Sciences*, 24(15):12182, 2023.

[88] P. H. W. Svensson, L. Schwob, O. Grånäs, I. Unger, O. Björneholm, N. Timneanu, R. Lindblad, A.-L. Vieli, V. Zamudio-Bayer, M. Timm, K. Hirsch, C. Caleman, and M. Berholts. Heavy element incorporation in nitroimidazole radiosensitizers: molecular-level insights into fragmentation dynamics. *Physical Chemistry Chemical Physics*, 2023.

[89] A. Hans, P. Schmidt, C. Küstner-Wetekam, F. Trinter, S. Deinert, D. Bloß, J. H. Viehmann, R. Schaf, M. Gerstel, C. M. Saak, J. Buck, S. Klumpp, G. Hartmann, L. S. Cederbaum, N. V. Kryzhevoi, and A. Knie. Suppression of X-ray-Induced Radiation Damage to Biomolecules in Aqueous Environments by Immediate Intermolecular Decay of Inner-Shell Vacancies. *The Journal of Physical Chemistry Letters*, 12(30):7146–7150, 2021.

[90] E. Pelimanni, A. Hans, E. Heikura, M. Huttula, and M. Patanen. Efficient neutralization of

core ionized species in an aqueous environment. *Physical Chemistry Chemical Physics*, 24(19): 11646–11653, 2022.

[91] G Lanzani, G Cerullo, S Stagira, and S De Silvestri. Excited state dynamics of oligothiophenes studied by transient pump-probe spectroscopy. *Journal of Photochemistry and Photobiology A: Chemistry*, 144(1):13–19, 2001.

[92] S. Salzmann, M. Kleinschmidt, J. Tatchen, R. Weinkauf, and C. M. Marian. Excited states of thiophene: ring opening as deactivation mechanism. *Physical Chemistry Chemical Physics*, 10 (3):380–392, 2008. Publisher: Royal Society of Chemistry.

[93] R. Weinkauf, L. Lehr, E. W. Schlag, S. Salzmann, and C. M. Marian. Ultrafast dynamics in thiophene investigated by femtosecond pump probe photoelectron spectroscopy and theory. *Physical Chemistry Chemical Physics*, 10(3):393–404, 2008.

[94] E. Kukk, D. T. Ha, Y. Wang, D. G. Piekarski, S. Diaz-Tendero, K. Kooser, E. Itälä, H. Levola, M. Alcamí, E. Rachlew, and F. Martín. Internal energy dependence in x-ray-induced molecular fragmentation: An experimental and theoretical study of thiophene. *Physical Review A*, 91(4): 043417, 2015.

[95] B. Marchetti, T. N. V. Karsili, O. Kelly, P. Kapetanopoulos, and M. N. R. Ashfold. Near ultraviolet photochemistry of 2-bromo- and 2-iodothiophene: Revealing photoinduced ring opening in the gas phase? *The Journal of Chemical Physics*, 142(22):224303, 2015.

[96] P. Kölle, T. Schnappinger, and R. de Vivie-Riedle. Deactivation pathways of thiophene and oligothiophenes: internal conversion versus intersystem crossing. *Physical Chemistry Chemical Physics*, 18(11):7903–7915, 2016.

[97] T. Schnappinger, P. Kölle, M. Marazzi, A. Monari, L. González, and R. de Vivie-Riedle. Ab initio molecular dynamics of thiophene: the interplay of internal conversion and intersystem crossing. *Physical Chemistry Chemical Physics*, 19(37):25662–25670, 2017.

[98] E. Kukk, H. Myllynen, K. Nagaya, S. Wada, J. D. Bozek, T. Takanashi, D. You, A. Niozu, K. Kooser, T. Gaumnitz, E. Pelimanni, M. Berholts, S. Granroth, N. Yokono, H. Fukuzawa, C. Miron, and K. Ueda. Coulomb implosion of tetrabromothiophene observed under multiphoton ionization by free-electron-laser soft-x-ray pulses. *Physical Review A*, 99(2):023411, 2019.

[99] S. Pathak, L. M. Ibele, R. Boll, C. Callegari, A. Demidovich, B. Erk, R. Feifel, R. Forbes, M. Di Fraia, L. Giannessi, C. S. Hansen, D. M. P. Holland, R. A. Ingle, R. Mason, O. Plekan, K. C. Prince, A. Rouzée, R. J. Squibb, J. Tross, M. N. R. Ashfold, B. F. E. Curchod, and D. Rolles. Tracking the ultraviolet-induced photochemistry of thiophenone during and after ultrafast ring opening. *Nature Chemistry*, 12(9):795–800, 2020.

[100] E. Kukk, H. Fukuzawa, J. Niskanen, K. Nagaya, K. Kooser, D. You, J. Peschel, S. Maclot, A. Niozu, S. Saito, Y. Luo, E. Pelimanni, E. Itälä, J. D. Bozek, T. Takanashi, M. Berholts, P. Johnsson, and K. Ueda. Formative period in the x-ray-induced photodissociation of organic molecules. *Physical Review Research*, 3(1):013221, 2021.

[101] B. W. Toulson, D. Hait, D. Faccialà, D. M. Neumark, S. R. Leone, M. Head-Gordon, and O. Gessner. Probing C–I bond fission in the UV photochemistry of 2-iodothiophene with core-to-valence transient absorption spectroscopy. *The Journal of Chemical Physics*, 159(3):034304, 2023.

[102] G. Barbarella, M. Melucci, and G. Sotgiu. The Versatile Thiophene: An Overview of Recent Research on Thiophene-Based Materials. *Advanced Materials*, 17(13):1581–1593, 2005.

[103] T. P. Kaloni, P. K. Giesbrecht, G. Schreckenbach, and M. S. Freund. Polythiophene: From Fundamental Perspectives to Applications. *Chemistry of Materials*, 29(24):10248–10283, 2017.

[104] K. Doré, S. Dubus, H.-A. Ho, I. Lévesque, M. Brunette, G. Corbeil, M. Boissinot, G. Boivin, M. G. Bergeron, D. Boudreau, and M. Leclerc. Fluorescent Polymeric Transducer for the Rapid, Simple, and Specific Detection of Nucleic Acids at the Zeptomole Level. *Journal of the American Chemical Society*, 126(13):4240–4244, 2004.

[105] C. Wu, E. R. Decker, N. Blok, H. Bui, T. J. You, J. Wang, A. R. Bourgoyne, V. Knowles, K. L. Berens, G. W. Holland, T. A. Brock, and R. A. F. Dixon. Discovery, Modeling,

and Human Pharmacokinetics of N-(2-Acetyl-4,6-dimethylphenyl)-3-(3,4-dimethylisoxazol-5-ylsulfamoyl)thiophene-2-carboxamide (TBC3711), a Second Generation, ETA Selective, and Orally Bioavailable Endothelin Antagonist. *Journal of Medicinal Chemistry*, 47(8):1969–1986, 2004.

[106] T. Yamamoto. Molecular assembly and properties of polythiophenes. *NPG Asia Materials*, 2(2): 54–60, 2010.

[107] B. Capozzi, E. J. Dell, T. C. Berkelbach, D. R. Reichman, L. Venkataraman, and L. M. Campos. Length-Dependent Conductance of Oligothiophenes. *Journal of the American Chemical Society*, 136(29):10486–10492, 2014.

[108] R. Shah and P. K. Verma. Therapeutic importance of synthetic thiophene. *Chemistry Central Journal*, 12(1):137, 2018.

[109] G. Turkoglu, M. E. Cinar, and T. Ozturk. Thiophene-Based Organic Semiconductors. In *Sulfur Chemistry*, pages 79–123. Springer International Publishing, 2019.

[110] L. Vallan, E. Istif, I. J. Gómez, N. Alegret, and D. Mantione. Thiophene-Based Trimers and Their Bioapplications: An Overview. *Polymers*, 13(12):1977, 2021.

TURUN
YLIOPISTO
UNIVERSITY
OF TURKU

Painosalama, Turku, Finland 2024

ISBN 978-952-02-0007-7 (PRINT)
ISBN 978-952-02-0008-4 (PDF)
ISSN 0082-7002 (PRINT)
ISSN 2343-3175 (ONLINE)